

**Copyright**  
**by**  
**Chandan Kumar**  
**2006**

**The Dissertation Committee for Chandan Kumar Certifies that this is the  
approved version of the following dissertation:**

**Parameter Inversion for Seismic Anisotropy**

**Committee:**

---

Robert J. Ferguson, Co-Supervisor

---

Mrinal K. Sen, Co-Supervisor

---

Paul L. Stoffa

---

Robert H. Tatham

---

Sergey B. Fomel

**Parameter Inversion for Seismic Anisotropy**

**by**

**Chandan Kumar B.Sc.; M.Sc.**

**Dissertation**

Presented to the Faculty of the Graduate School of

The University of Texas at Austin

in Partial Fulfillment

of the Requirements

for the Degree of

**DOCTOR OF PHILOSOPHY**

**The University of Texas at Austin**

**December, 2006**

**Dedicated to my parents**

*Sri Nandkishore Prasad Singh & Smt. Shubhadra Devi*

## **Acknowledgements**

First, I would like to sincerely thank my supervisors, Dr. Mrinal K Sen and Dr. Robert J. Ferguson for their guidance, encouragement and discussions throughout my graduate studies. I would also like to acknowledge Dr. Paul L. Stoffa, Dr. Robert H. Tatham, and Dr. Sergey Fomel for serving as my committee members and for their suggestions to improve the dissertation and Dr. Steve P. Grand and Dr. Timothy Rowe for serving as committee members during my PhD proposal.

I would like to thank Dr. Clark Wilson and Dr. Paul Sava for discussions on various issues related to my study. I also thank other scientists at the Institute for Geophysics for their suggestions and help.

I would like to extend my gratitude to my present and former colleagues at the Institute for Geophysics University of Texas at Austin: Dhananjay Kumar, Imtiaz Ahmed, Armando Sena, Rishi Bansal, Samarjit Chakraborty, Sanjay Sood, Chunlei Chu, Russell Young, Tiankong Hong, Carmen Gomez, Chengshu Wang, Jason Gumble, Erick Leuro, Irina Filina, Krishnavikas Gudipati, Sylvia Nordfjord, Alejandro Escalona, Xinxia Wu, Sasha Carter, Paresh Patel, David Soto, Nedra Bonal. My special thanks go to the visiting scientists at the Institute for Geophysics, Dr. Achintya Paul, Dr. Indrajit G. Roy, Dr. Ranjit Shaw, Dr. Lopamudra Roy and Dr. Long Jin for their help and encouragement. I also thank Samrat Goswami, Sanjoy Gupta, Anuj Jain, Pawan Dewangan, Priyank Jaiswal,

Manish Kumar, Jyoti Behura, Ravi Shekhar, Satish Sinha, Robin Ozah, Nandakishore Sukhavasi, Arnab Gupta, Saurabh Sinha, Jyoti Khetan, Pankaj Kalra, Ravi Agarawal and other friends and family for their wonderful support during my stay at Austin.

I would also like to acknowledge various geoscientists at BP America Inc, Houston for the fruitful discussions during the summer of 2005.

I also thank Mark Wiederspahn, Kevin Johnson, John Gerboc and Steffen Saustrop for their technical support; Susan Beaubien, Judy Sansom, Dr. Katherine Ellins, Jan Everett, Lisa Gahagan, Patricia E Ganey-Curry and Nancy Hard for their help (from UTIG). I would like to thank Miriam Pashby and Phillip Guerrero from the Department of Geological Sciences; Mary Koch, Debra Sue Trinquen and Rita Omrani from the Geology Foundation for all their help.

I would also like to acknowledge various sources of financial support during my graduate studies: Teagle Fellowship, BP Fellowship, Shell Fellowship and Chevron Scholarship.

This work could not have been completed without continuous love and support of my parents and family.

# **Parameter Inversion for Seismic Anisotropy**

Publication No. \_\_\_\_\_

Chandan Kumar, Ph.D.

The University of Texas at Austin, 2006

Supervisors: Robert J. Ferguson and Mrinal K. Sen

An important objective of reflection seismology is to transform a seismic dataset into a reflectivity image of the subsurface. Reflectivity imaging involves removal of propagation effects by creating an inverse propagation operator using an estimated macro velocity model. The accuracy of a reflectivity image depends on the accuracy of the velocity model used. Hence, the estimation of a good velocity model is crucial. Flat sedimentary layers, though laterally homogeneous over small-scale, often exhibit a simple kind of anisotropy called vertical transverse isotropy (VTI). Negligence of anisotropy in migration may result in significant deviation of an imaged reflector from its true position. Our ability to estimate anisotropic parameters using limited aperture, limited bandwidth seismic data is restricted. Several recent developments in data acquisition including more intense acquisition (e.g., 3-D), broader bandwidths, and new survey methodologies (e.g., Ocean Bottom Seismics and vertical cables) have improved our ability in dealing with anisotropy. In light of these recent developments the

objective of my research is three-fold - (i) finding better algorithms for anisotropy estimation that makes use of enhanced data acquisition, more powerful computers and graphical interfaces, (ii) understanding and re-evaluating our limitations/capabilities of anisotropy estimation in light of the new algorithms, and (iii) using the results of analysis as an aid to constrain anisotropy estimates.

The *Common Focus Point* (CFP) technology defines a recent method of prestack migration velocity analysis which has several advantages over other popular methods. One remarkable advantage is that the imaging error is given directly in time allowing easier model updates through inversion. The CFP technique has been used in recent past for estimating isotropic heterogeneous velocity model for geologically complex subsurface. For my research, I extend this method to anisotropic parameter inversion by suitably implementing the space-time domain version of CFP method for picking the traveltimes error resulting from the incorrect guess model. I successfully implement this approach to estimate anisotropy of the shale thrust-sheets in the Canadian Foothills model. This model has targets of interest below transversely isotropic shale thrust-sheets and estimating anisotropic parameters is important for proper depth imaging of target zone. The synthetic P-mode data used for the analysis has been generated using a finite difference algorithm.

In order to quantitatively assess the advantages or limitations of CFP domain velocity analysis in estimating the anisotropic parameters, I have performed *sensitivity analysis* under different experimental settings like different observation apertures, layer thicknesses, tilt in symmetry axis, picking error and



the use of mode converted data. The results quantitatively establish the advantage of joint inversion of P-P and P-Sv over the conventional inversion of solely P-P data in constraining the depth and anisotropic parameters. Also the constraint on parameter estimation improves with increase in angle of tilt of symmetry axis with respect to the reflector.

The CFP domain analysis also has advantages in dealing with mode converted P-Sv data as separate focusing at the receiver side and source side allows it to deal with one wave type at a time. In complex media, this helps avoid the cumbersome calculation of common conversion point (CCP) location. The CFP analysis has been applied for estimating anisotropic parameters as well as layer thickness by *joint inversion* of P-P and P-Sv synthetic data for the geology encountered in Blackfoot field.

## Table of Contents

List of Figures .....	xii
List of Tables.....	xviii
Symbols .....	xix
Chapter 1: Introduction .....	1
1.1 Motivation .....	1
1.2 Anisotropy in Seismic Exploration .....	2
1.3 Migration Velocity Analysis .....	5
1.3.1 The CMP Method .....	5
1.3.2 The CRS Method .....	10
1.3.3 The CIG Method .....	12
1.3.4 The CFP Method .....	13
1.3.5 Comparison of CMP, CRS, CIG and CFP Methods .....	15
1.4 Inversion and Sensitivity Analysis .....	17
1.5 Joint Inversion of P-P and P-Sv data.....	21
1.6 Thesis Objective .....	21
Chapter 2: Elastic Parameter Estimation in Common Focus Point domain .....	24
2.1 Introduction .....	24
2.2 Common Focus Point (CFP) Velocity Analysis .....	29
2.2.1 WRW Formulation .....	29
2.2.2 CFP Synthesis in Space-Time Domain .....	36
2.2.3 CFP Synthesis in Plane Wave Domain .....	39
2.3 Traveltime Calculation in TTI Media .....	40
2.4 Model Parametrization and Inversion .....	46
2.5 Parameter Estimation for Foothills Model .....	50
2.6 Results .....	52

2.7 Conclusion .....	57
Chapter 3: Traveltime Sensitivity Analysis .....	58
3.1 Introduction .....	58
3.2 Theory .....	61
3.3 Sensitivity Analysis .....	68
3.3.1 Sensitivity Analysis for VTI media.....	68
3.3.2 Sensitivity Analysis for TTI media .....	68
3.4 Summary .....	71
Chapter 4: Joint Inversion of P-P and P-Sv Data .....	76
4.1 Introduction .....	76
4.2 Theory .....	84
4.2.1 WRW Formulation for Multi-component Data.....	85
4.2.2 Space-Time Domain CFP Analysis of C-wave.....	88
4.2.3 Plane Wave Domain CFP Analysis of C-wave.....	90
4.3 Method .....	94
4.4 Analytic Example.....	99
4.5 Synthetic Data Example .....	102
4.6 Summary .....	109
Chapter 5: Summary and Future work .....	111
5.1 Summary .....	111
5.2 Future work .....	114
References .....	116
Vita.....	127

## List of Figures

Figure 1.1. Sorting from a shot gather to a CDP gather geometry. CMP is the surface common mid point location between shot and receiver. If the subsurface comprises of horizontal reflectors then CMP is the vertical projection of CDP on the surface. ....	7
Figure 1.2. (a) Half space velocity model, left. (b) Incorrect velocity model used for migration, right.....	9
Figure 1.3. (a) CIG migrated using the incorrect velocity of Figure 1.2b, (b) residual depth corrected CIG using the incorrect velocity of 1.4 km/s to do the residual depth correction to the CIG in Figure 1.3a, (c) residual depth corrected CIG using the incorrect velocity 1.6 km./s. to do the residual depth correction to the CIG in Figure 1.3a, and (d) residual depth corrected CIG using the true velocity of 1.5 km./s. to do the residual depth correction to the CIG in Figure 1.3a.....	10
Figure 1.4. Traveltime from a CFP to all receiver positions is used to calculate the operator.....	14
Figure 1.5. Time-reversed focusing operator based on traveltime computation in assumed model.....	15
Figure 1.6. (a) Shotgathers from shot 1 to shot 81, (b) The traces corresponding to each shot gather, obtained after application of focusing operator on corresponding shot gather. The arrow marks the event of specular reflection from the given CFP. ....	17
Figure 1.7. CFP response obtained by placing the traces from Fig. 5 at corresponding shot position. ....	19
Figure 1.8. CFP response is indicative of trvaeltime from the CFP to shot positions as obtained from data.....	20

Figure 1.9. Difference of focusing operator and CFP response (DTS panel) for the correct model.....	20
Figure 2.1. Plot of slowness $p=k_x/\omega$ versus phase angle $\theta$ for dipping TI medium. Each value of $p$ in the range indicated by the arrow corresponds to two phase angles. Values outside of this range are uniquely defined (from Ferguson and Margrave, 2002).....	26
Figure 2.2. The impulse response for phase shift in a homogeneous TI medium with an axis of symmetry of $45^\circ$ . The dashed curve shows the theoretical response. The impulse response does not track the theoretical response beyond $90^\circ$ (left side of figure) (from Ferguson and Margrave, 2002).....	26
Figure 2.3. Anisotropic thrust sheet embedded in a homogeneous, isotropic medium.....	27
Figure 2.4. Zero-offset gather. The pull up in the base reflector (inside the ellipse) is evident and is due to the fact that it lies below highly dipping thrust-sheet..	31
Figure 2.5. Migrated image using isotropic velocity model. The poor image of base reflector (inside the ellipse) below the dipping thrust-sheet is due to isotropic assumption in imaging....	32
Figure 2.6. Ray tracing from focus point 'C' (Figure 2.3) to the source-receiver locations. The ray direction with respect to TI symmetry axis shown by arrow varies from near parallel at X to near horizontal at Y.....	32
Figure 2.7. In the first focusing step, each shot record is transformed to one event of the focus-point response (Fresnel-zone stacking). In the second focusing step, all events in the focus point response are aligned at the one-way image time, followed by weighted superposition (CFP stacking). Note that here one-way image ray connects two points with the same lateral position; note also that the traveltimes along this one-way image ray defines one-way image time (from Berkhout, 1997)....	37
Figure 2.8. (a) CFP operator; (b) CFP gather for point 'C' (Figure 2.3) corresponding to the initial-guess model. Differences in traveltimes to the peak energy in the CFP operator and gather indicate error in the model.....	38
Figure 2.9. (a) Single traveltimes calculation scheme. Traveltimes $t_1$ and $t_2$ are known and $t_0$ is calculated to minimize the total traveltimes $t$ , (b) For a given	

point of interest A, eight traveltimes can be computed based on eight gridpoints surrounding it. The minimum of these provide the first arrival traveltime (from Kumar et al., 2004)...	42
Figure 2.10. (a),(b): Traveltime mapping scheme: traveltimes for grid points on the left side of the source (a) and on the right side of the source (b) are calculated column-by-column until the left and right edge of the grid, correspondingly, are reached. (after Faria and Stoffa, 1994).....	43
Figure 2.10. (c),(d): Traveltime mapping scheme: from left to right and right to left away from the source column, moving from the source level to the bottom of the grid (c) and from the source level to the top of the grid (after Faria and Stoffa, 1994).....	44
Figure 2.11. Parametrization of heterogeneous velocity model using spline interpolation.....	45
Figure 2.12. Parametrization of VTI model: $\epsilon$ and $\delta$ are zero for isotropic layers.....	45
Figure 2.13. DTS panel for point ‘C’ (Figure 1) corresponding to the initial-guess model.....	53
Figure 2.14. (a) CFP operator; (b) CFP response for point ‘C’ (Figure 1), after inversion and model update. Traveltimes to reflectoion peaks are similar, as the model updates are approaching their true values.....	55
Figure 2.15. The DTS panel after inversion and model update. Traveltime picks align with zero lag to indicate an improved model....	56
Figure 2.16. Migrated image using anisotropic velocity model obtained through inversion.....	57
Figure 3.1. Plot of offset to depth ratio versus error in vertical traveltime ( $\Delta\tau$ ) for P-arrival resulting from approximately 10% error in the model parameters [ $\alpha_0, \beta_0, \epsilon, \delta, z$ ]. .....	63
Figure 3.2. Plot of offset to depth ratio versus error in vertical traveltime ( $\Delta\tau$ ) for Sv-arrival resulting from approximately 10% error in the model parameters [ $\alpha_0, \beta_0, \epsilon, \delta, z$ ]... ..	64

Figure 3.3. Plot of $V_p$ versus error for fixed $z$ and variable $z$ . For fixed $z$ , error has a sharp curvature at the minimum compared to that for variable $z$ ..	66
Figure 3.4. Plot of parameter uncertainty versus offset to depth ratio for P-P data, when depth is known. As the offset to depth ratio increases, parameter uncertainty for $\epsilon$ and $\delta$ decreases, while uncertainty for $\alpha_0$ remains low and nearly constant.....	72
Figure 3.5. Plot of parameter uncertainty versus offset to depth ratio for joint inversion of P-P and P-Sv data. As the offset to depth ratio increases, parameter uncertainty decreases.....	73
Figure 3.6. Plot of parameter uncertainty versus offset to depth ratio for joint inversion of P-P and Sv-Sv data. As the offset to depth ratio increases, parameter uncertainty decreases.....	74
Figure 3.7. Slowness curves for Mesaverde clayshale. The dotted blue line is slowness curve when symmetry axis is vertical. The continuous green line is slowness curve when symmetry axis is tilted by $45^\circ$ w.r.t. vertical. The ' $\nabla$ 's are slownesses for downgoing waves and ' $\Delta$ 's for upgoing waves corresponding to a certain range of ray parameters.....	75
Figure 4.1. Plot of offset to depth ratio versus error in traveltime for P-P waves for 20% error in parameters (a) $\alpha_0$ , $\beta_0$ and (b) $\epsilon$ , $\delta$ . The rock parameters of Mesaverde shale (Thomsen, 1986) used.....	78
Figure 4.2. Plot of offset to depth ratio versus error in traveltime for P-Sv waves for 20% error in parameters (a) $\alpha_0$ , $\beta_0$ and (b) $\epsilon$ , $\delta$ . The rock parameters of Mesaverde shale (Thomsen, 1986) used.....	79
Figure 4.3. Plot of offset to depth ratio versus error in traveltime for Sv-Sv waves for 20% error in parameters (a) $\alpha_0$ , $\beta_0$ and (b) $\epsilon$ , $\delta$ . The rock parameters of Mesaverde shale (Thomsen, 1986) used.....	80
Figure 4.4. The glauconite channel system at Blackfoot oil field, Alberta, is a sequence of sand and shale filled valleys incised into Lower Cretaceous and Mississippian carbonates. The Blackfoot interpretation has an upper and lower channel that are prospective and separated by a non-porous lithic channel (from Margrave et al., 2001).....	83

Figure 4.5. In the first focusing step, each shot record is transformed to one event of the focus-point response (Fresnel-zone stacking). In the second focusing step, all events in the focus point response are aligned at the one-way image time, followed by weighted superposition (CFP stacking). Note that here one-way image ray connects two points with the same lateral position; note also that the traveltimes along this one-way image ray defines one-way image time.....	89
Figure 4.6. (a) P-wave focusing operator used for focusing P-P data, (b) Sv-wave focusing operator used for focusing converted wave P-Sv data....	91
Figure 4.7. (a) P-wave focusing operator versus (b) CFP gather for P-P data after focusing at receiver end using P-wave focusing operator in Fig. 4.6 (a).....	92
Figure 4.8. (a) P-wave focusing operator versus (b) CFP gather for P-Sv data after focusing at receiver end using Sv-wave focusing operator in Fig. 4.6 (b)....	93
Figure 4.9. (a) DTS panel obtained by cross-correlating P-wave operator in Fig. 4.7 (a) and CFP gather in Fig. 4.7 (b), (b) DTS panel obtained by cross-correlating P-wave operator in Fig. 4.8 (a) and CFP gather in Fig. 4.8 (b).....	96
Figure 4.10. (a) P-wave focusing operator versus (b) CFP gather for P-P data for 10% error in model parameters....	97
Figure 4.11. (a) P-wave focusing operator versus (b) CFP gather for P-Sv data for 10% error in model parameters.....	98
Figure 4.12. (a) DTS panel obtained by cross-correlating P-wave operator in Fig. 4.10 (a) and CFP gather in Fig. 4.10 (b), (b) DTS panel obtained by cross-correlating P-wave operator in Fig. 4.11 (a) and CFP gather in Fig. 4.11 (b) for 10% erroneous model.....	99
Figure 4.13. The z-component of shot gather generated by finite differencing modeling for an elastic model based on Blackfoot geology after removal of direct arrival....	100
Figure 4.14. The x-component of shot gather generated by finite differencing modeling for an elastic model based on Blackfoot geology after removal of direct arrivals.....	102



Figure 4.15. The z-component of shot gather in Figure 4.13, after performing radon transformation.....	104
Figure 4.16. The x-component of shot gather in Figure 4.14, after performing radon transformation.....	105
Figure 4.17. The picking of differential time shift (DTS) on P-P mode data for the initial guess model.....	106
Figure 4.18. The picking of differential time shift (DTS) on P-Sv mode data for the initial guess model.....	107
Figure 4.19. The picking of differential time shift (DTS) on P-P mode data for the model after inversion. ....	108
Figure 4.20. The picking of differential time shift (DTS) on P-Sv mode data for the model obtained from inversion.....	109

## **List of Tables**

Table 2.1. Result of anisotropic parameter estimation for Foothills model. The true, initial guess and final model parameters obtained after inversion.....	54
Table 3.1. Uncertainty in elastic parameter estimates for different types of data as calculated analytically. Maximum offset to depth ratio is 1.5 and standard deviation is 4 ms.....	69
Table 3.2. Uncertainty in elastic parameter estimates for different tilt angles for a TTI medium using P-wave data only when tilt angle of the TI medium is known.....	70
Table 3.3. Uncertainty in elastic parameter estimates for different tilt angles for Joint Inversion of PP and SvSv data for offset to depth ratio of 1 and standard deviation of 4 ms. The angle of tilt of TI medium is also a model parameter. ....	71
Table 4.1. Result of analytic inversion for the anisotropic layers in the Blackfoot model.....	101
Table 4.2. Results of parameter inversion using CFP method for the anisotropic parameters of Fisch Scale layer in the Blackfoot model.....	104

## Symbols

OBS	Ocean bottom seismometer (records 4-C data)
VSP	Vertical seismic profile (records 3-C data)
VTI	Vertical transverse isotropy
TTI	Tilted transverse isotropy (TI with a tilted axis of symmetry)
HTI	Horizontal transverse isotropy (TI with a horizontal axis of symmetry)
NMO	Normal moveout
$p$	Ray parameter
$\tau$	Intercept time (vertical travelttime)
PP-wave	Incident P-wave reflected as P-wave
PS-wave	Incident P-wave reflected as S-wave (converted S-wave)
$\alpha_0$	Vertical P-wave velocity
$\beta_0$	Vertical S-wave velocity
$\alpha_{90}$	Horizontal P-wave velocity
$\delta, \epsilon, \gamma$	Thomsen's VTI anisotropic parameters (unitless)

## **Chapter 1: Introduction**

### **1.1 MOTIVATION**

An important objective of reflection seismology is to transform a preprocessed seismic dataset into a reflectivity image of the subsurface. The primary reflection data contains (i) the propagation effects of the medium and (ii) the reflections from the different layer boundaries in the medium (Berkhout, 1982, p. 167). The propagation effects represent the integral, or average velocities (macro layering or low wavenumber content of the subsurface) over the distance traveled (Stolt and Benson, 1986, p. 25). Reflections, on the other hand, represent the derivative or changes in physical properties (detail layering or high wavenumber content of the subsurface), one of which is velocity (Stolt and Benson, 1986, p. 25). Reflectivity imaging involves removal of propagation effects by creating an inverse propagation operator using an estimated macro velocity model (Berkhout, 1982, p. 167). The accuracy of a reflectivity image depends on the accuracy of the velocity model used to create inverse propagation operator. Hence, the estimation of a good velocity model is crucial. The method used to accomplish this is called migration velocity analysis (Stolt and Benson, 1986, p. 25). In the presence of anisotropy, velocity analysis also estimates the parameters that control the directional dependence of velocity.

Flat lying sedimentary rocks, though laterally homogeneous over small-scale, often exhibit a simple kind of anisotropy called vertical transverse isotropy (VTI) (Officer, 1958; Krey and Helbig, 1956; Daley and Hron, 1977). Negligence of anisotropy in migration may result in significant deviation of a reflector from its true position (Leslie and Lawton, 1998). Hence, it is necessary to incorporate anisotropy in migration algorithms. However, our ability to estimate anisotropic parameters using limited aperture, limited bandwidth seismic data is restricted and depends on several factors like data acquisition, depth and thickness of target layer etc. (Tsvankin and Thomsen, 1994). The study of effect of rate of change in output parameters with respect to changes in model inputs is called sensitivity analysis. Sensitivity analysis is a useful tool and helps numerically quantify uncertainty associated with different elastic parameters under different data acquisition setups.

## **1.2 ANISOTROPY IN EXPLORATION SEISMOLOGY**

Anisotropy is defined simply as a variation of a physical property with the direction in which it is measured (Winterstein, 1990). In the context of seismic wave propagation, anisotropy is the variation of wave propagation with the direction of propagation and/or the polarization of shear waves (Winterstein, 1989; Tatham and McCormack, 1991). Seismic anisotropy can be of three types – (a) Inherent, (b) Induced, and (c) Long wavelength anisotropy (Tatham and

McCormack, 1991, page 35). Inherent anisotropy may be caused by: (i) the specific crystal structure of minerals forming a rock leading to crystalline anisotropy (Crampin et. al., 1984), (ii) directed stress (Crampin et. al., 1984), (iii) preferred orientation of elongated or flat cracks or grains leading to lithologic anisotropy (Crampin et al., 1984). Induced anisotropy occurs when stress causes preferred orientation of cracks (Anderson et. al., 1974; O'Connell and Budiansky, 1974; Budiansky and O'Connell, 1976; Crampin, 1978; Bamford and Nunn, 1979; Hudson, 1981). Most sedimentary rocks of the upper crust are found experimentally to be anisotropic due to their sedimentary origin and lithification under gravity (Thomsen, 1986). Moreover, if a layered isotropic media is investigated with an elastic wave of wavelength much longer than the typical layer thickness, the wave propagates as though in anisotropic medium (Backus, 1962). This type of anisotropy, called long-wavelength anisotropy can be observed if the geologic medium has laminations, parallel fractures etc. (Crampin, 1978; Schoenberg and Douma, 1988; Helbig, 1998).

Seismic anisotropy is not a new concept in exploration seismology. The physics of seismic anisotropy has been understood well based on the theory of continuum mechanics and linear elastic theory (Love, 1944). The degree of velocity anisotropy in stratified rocks has been measured and reported by White and Sengbush (1953), Cholet and Richard (1954) and Uhrig and van Melle (1955) and others. Crampin et al. (1984) provides a good review of the state-of-the-art

seismic anisotropy, however, the subject of anisotropy assumes an altogether different dimension when looked from an imaging perspective. From an imaging perspective, some aspects of anisotropy may be simplified while others get complicated and probably intractable with current models. Simplification comes from the fact that many cases of anisotropy encountered in exploration seismology is transverse isotropy (Thomsen, 1986). This greatly reduces the number of unknown parameters. The complication arises from the fact that the scalar aspect of reflection data is not very sensitive to anisotropy (Thomsen, 1986). The poor sensitivity to anisotropy is due to factors related to our limitations in data acquisition – limited aperture, limited bandwidth, scalar nature of seismic data and the presence of noise (Tsvankin and Thomsen, 1994). Several recent developments in data acquisition including more intense acquisition (e.g., 3-D, 4-D), broader bandwidths, and new survey methodologies (e.g., Ocean Bottom Seismics and vertical cables) have improved our ability in dealing with anisotropy. In light of these developments, we can improve our ability in dealing with anisotropy by

- (i) finding better algorithms for anisotropy estimation that makes use of enhanced data acquisition, more powerful computers and graphical interfaces,
- (ii) understanding and re-evaluating our limitations/capabilities of anisotropy estimation in light of the new algorithms, and
- (iii) using converted wave data as an aid to constrain anisotropy estimates.

In the following three sections, I provide a brief review of each of these aspects of anisotropy estimation problems.

### **1.3 MIGRATION VELOCITY ANALYSIS**

With time, several migration velocity analysis techniques have come into existence. Each has its merits and limitations depending upon the nature of data (e.g. short offset vs. long offset), resources available (e.g. computational power, data size) and the geological setting (e.g. weakly heterogeneous vs. strongly heterogeneous). In this section I briefly discuss the commonly used domains of velocity analysis and how they compare with the CFP method for anisotropy estimation.

#### **1.3.1 THE CMP METHOD**

The Common Mid Point (CMP) method (see Yilmaz, 1987, page 45), is based on the assumption of flat reflectors so that for a particular shot-receiver pair, the reflection point (common depth point or CDP), is located at a position on the reflector midway between the source and receiver (common mid point or CMP) at some depth (see Figure 1.1). For each CMP, the reflection traveltimes as a function of offset is given by the approximation for reflection moveouts from a Taylor series expansion of the  $t^2(x^2)$  curve near  $x^2 = 0$  (Dix, 1955; Taner and Koehler, 1969; Hake et al., 1984; Tsvankin and Thomsen, 1994). For short-spread data in laterally homogeneous isotropic media, reflection moveouts are approximately hyperbolic and are accurately described using just



the first two terms of an infinite series representation (Taner and Koehler, 1969). However, moveout becomes non-hyperbolic with increasing offset and a vertical variation in velocity (Yilmaz, 1987, page 48). To build a velocity model, an attempt is made to find a velocity (normal moveout velocity NMO) which corrects for this moveout. For short-spread data in a horizontally layered subsurface, the NMO velocity equals approximately the root mean square (rms) velocity (Dix, 1955; Taner and Koehler, 1969; Al-Chalabi, 1973; Hubral and Krey, 1980). Interval velocity (the model) can be obtained from the rms velocity using Dix's formula (Dix, 1955).

$$v_{\text{int}}^2 = \sqrt{\frac{v_n^2 t_n - v_{n-1}^2 t_{n-1}}{t_n - t_{n-1}}} \quad , \quad (1.1)$$

where  $v_n$  and  $v_{n-1}$  are the rms velocities at layer boundaries  $n$  and  $n-1$  respectively, and  $t_n$  and  $t_{n-1}$  are the horizon times measured on seismic data corresponding to layer boundaries  $n$  and  $n-1$ . NMO correction, followed by stacking based on nmo velocity analysis, yields improved signal to noise ratio especially for coherent noise (Yilmaz, 1987). The NMO method, however, fails to take into account lateral heterogeneity and so its accuracy is limited to media that are laterally homogeneous within the surface aperture of the CDP gather.

In the presence of anisotropy (say VTI) and/or vertical heterogeneities, the higher order terms from the series representation describe non-hyperbolic moveout for larger offsets. Tsvankin and Thomsen (1994), and Alkhalifah and

Tsvankin (1995) have expressed these higher order terms using anisotropic parameters for homogeneous (one-layer) VTI media. Alkhalifah (1997), and Grechka and Tsvankin (1998) have obtained the expressions for higher order terms in the case of multiple layers. An attempt is made to obtain values for the higher order terms by finding statistically best fits to traveltime curves, and inverting these fits to estimate anisotropic parameters (or a combination of them). This method, however, cannot overcome inherent non-uniqueness, even by using long spreads, if only P-wave data are included (Tsvankin and Thomsen, 1995).

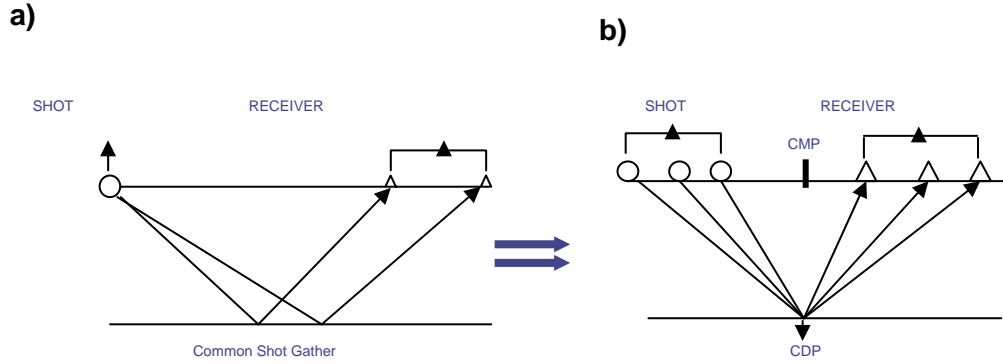


Figure 1.1: Sorting from a shot gather to a CDP gather geometry. CMP is the surface common mid point location between shot and receiver. If the subsurface comprises of horizontal reflectors then CMP is the vertical projection of CDP on the surface.

In the presence of VTI, two combinations of anisotropic parameters namely

NMO velocity ( $v_{nmo} = \alpha_0 \sqrt{1 + 2\delta}$ ) and anellipticity ( $\eta = \frac{\epsilon - \delta}{1 + 2\delta}$ ) can be obtained

from P-wave reflection data from interfaces with different dips (Alkhalifah and Tsvankin, 1995), or from long spread P-wave reflection data from horizontal interface (Alkhalifah, 1996), or from weakly laterally heterogeneous media with horizontal interface (Grechka, 1998), with stability of  $\eta$  estimation decreasing by the same order of magnitude. While  $v_{nmo}$  and  $\eta$  are sufficient to accommodate anisotropy corrections in time migration, they cannot resolve vertical velocity for construction of velocity models needed for depth migration (Stunff et al., 2001). Stunff et al. (2001) demonstrate that all three VTI parameters ( $\alpha_0$ ,  $\varepsilon$  and  $\delta$ ) can be estimated from inversion of arrival times and acquisition geometry if the model contains an intermediate non-horizontal interface. Thus, an anisotropic depth model can be constructed. Information about the vertical velocity and reflector depth was contained in the reflected rays which crossed the dipping intermediate interface (Stunff et al., 2001). Although lateral heterogeneity does create a dependence of P-wave traveltimes on the vertical velocity, there is no guarantee that for a general heterogeneous model all anisotropic parameters can be resolved successfully (Stunff et. al., 2001).

Wave propagation in anisotropic media is manifested in seismic data as anomalies in traveltimes, amplitudes and waveforms. Traveltime data are commonly used in seismic parameter estimation with normal moveout (NMO) based analysis (e.g., Tsvankin, 2001). In NMO analysis, a truncated Taylor series is used to approximate the reflection traveltime equation in a common-mid-point

(CMP) geometry. Authors van der Baan and Kendall (2002), and Sen and Mukherjee (2003) give traveltime expressions for NMO in the  $\tau$ -p (intercept traveltime – ray parameter) domain in a VTI medium. It has been established that from P-wave traveltime analysis alone, three anisotropic parameters ( $\alpha_0$ ,  $\epsilon$  and  $\delta$ ) describing P-wave propagation in a VTI medium (dependence on the fourth parameter  $\beta_0$  is very weak), cannot be determined uniquely from the surface seismic data (Tsvankin and Thomsen, 1994). Anisotropic parameters in a VTI medium can be estimated with the analysis of multicomponent seismic data or a priori information like well-log data or geologic descriptions of the media.

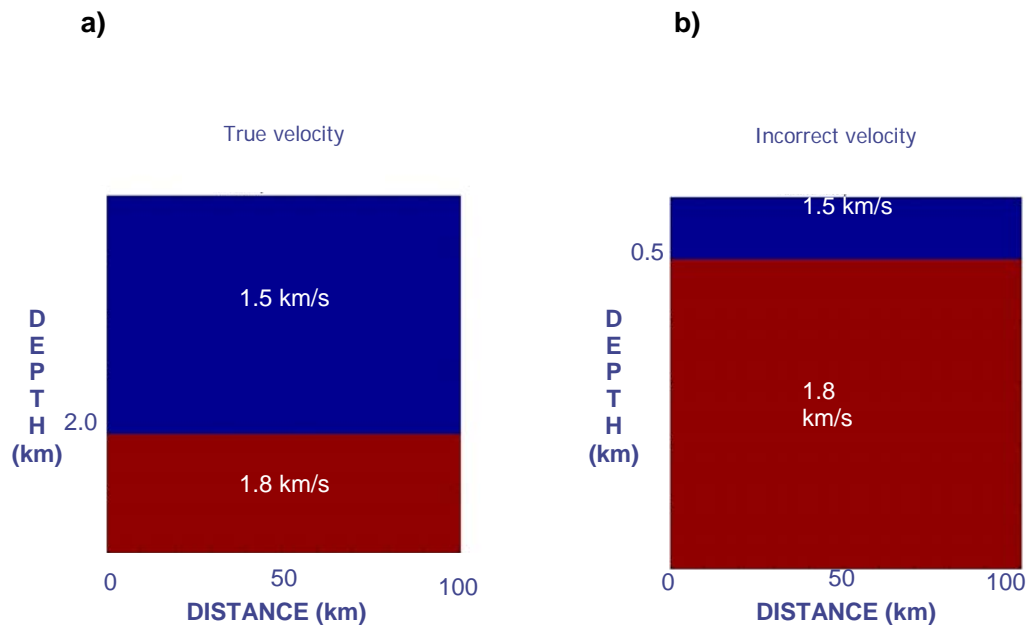


Figure 1.2 (a) Half space velocity model, left. (b) Incorrect velocity model used for migration, right.

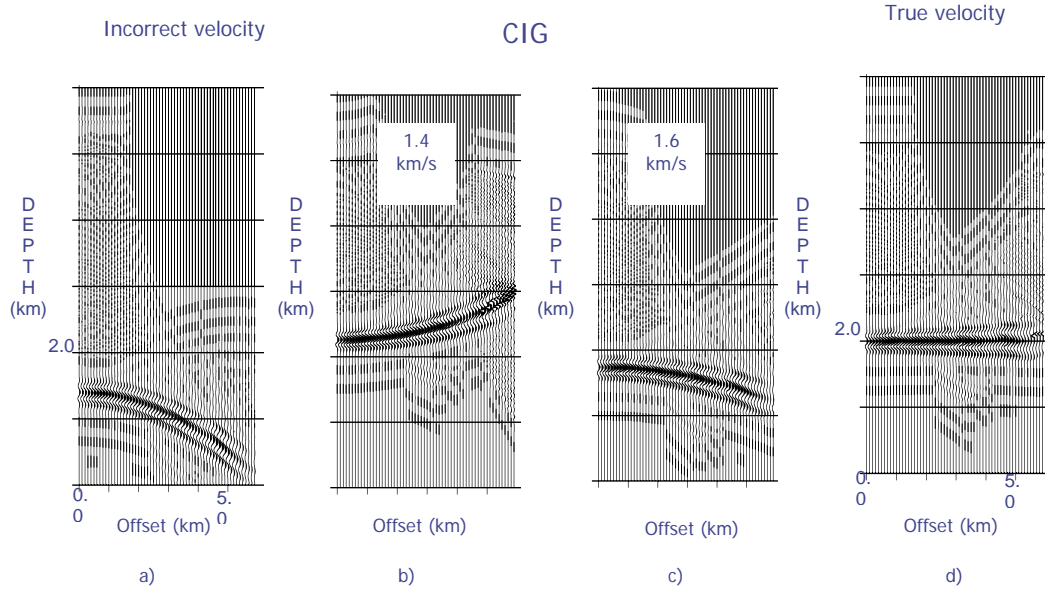


Figure 1.3 (a) CIG migrated using the incorrect velocity model of Figure 1.2b, (b) residual depth corrected CIG using the incorrect velocity of 1.4 km/s to do the residual depth correction to the CIG in Figure 1.3a, (c) residual depth corrected CIG using the incorrect velocity 1.6 km./s. to do the residual depth correction to the CIG in Figure 1.3a, and (d) residual depth corrected CIG using the true velocity of 1.5 km./s. to do the residual depth correction to the CIG in Figure 1.3a.

### 1.3.2 THE CRS METHOD

The Common Reflecting Surface (CRS) is a generalization of the well-known CMP stack and velocity analysis (Bergler et al., 2002). It simulates zero offset sections from 2-D seismic reflection pre-stack data (Muller et al., 1998; Hubral, 1983). In this method stacking of data is not constricted within a single

CMP gather based on one parameter (stacking velocity) analysis (Muller et. al., 1998). Instead, the data are focused to a common reflection surface (CRS) using multiple shots and receivers based on a three parameter analysis. The three parameters are

- (i) the emergence angle of a zero offset ray at the surface ( $\alpha$ ),
- (ii) the curvature of the wavefront at the normal-incidence-point on the reflector associated with the zero-offset ray ( $R_{NIP}$ ), and

- (iii) the curvature of the wavefront that represents the envelope of the wavefronts associated with Huygens' secondary sources along the reflector ( $R_N$ ).

The CRS stacking operator and prestack Kirchhoff type operator (Schneider, 1978) based on diffraction approximate each other if  $R_N=R_{NIP}$ . The Kirchhoff operator is usually determined with the help of a velocity model, while the CRS operator is determined by  $\alpha$ ,  $R_N$ , and  $R_{NIP}$ , and thus provides a model-independent approximation for Kirchhoff operator where  $R_N=R_{NIP}$ . Since the CRS method is model-independent, it can be applied to reflection data from any kind of subsurface. Moreover, the three parameters, (wavefield attributes) can be used in inversion algorithms to finally obtain a velocity model (Biloti et al., 2001). However, I have not seen any attempt to obtain anisotropic parameters from the wavefield attributes using CRS method, in the literature. Incorporating anisotropy in the CRS method should be an interesting area of future research.

### 1.3.3 THE CIG METHOD

In Common Image Gather (CIG) analysis, after prestack migration of common offset data sets, imaged multi-channel data are sorted into common image gathers (CIGs) (Al-Yahya, 1989, Liu and Bleistein, 1995, Varela, 1996). In each CIG, the data have the same imaged horizontal location viewed from different offset/angles. After prestack migration with the correct velocity (see Fig. 1.2a), the imaged depths of individual events at a CIG must be the same regardless of offset (see Fig. 1.3d) so that after stacking, a coherent image of the reflecting point results. After migration with an incorrect velocity (see Fig. 1.2b), the imaged depths at a CIG will differ (see Fig. 1.3a, b, c) (Varela, 1996). The difference of imaged depths (also called residual moveout) provides information with which to correct the velocity based on the quantitative relationship between residual moveout and migration velocity (Varela, 1996). Thus, the residual moveout gives error in depth, and analysis is performed in the space domain. The equation relating traveltimes error to depth error is based on some simplifying assumptions about velocity model e.g., a 1D velocity model assumption (Jiao et al., 2002; Ahmed, 2003) or using simple geometry for 2D/3D velocity model and is thus inaccurate in complex media. This may lead to slow convergence in the presence of strong lateral heterogeneity (Kabir, 1997). The CIG (offset-depth) domain has been used to analyze anisotropic parameter determination for factorized VTI medium using P-wave data (Sarkar and Tsvankin, 2003). (A

medium is said to be factorized if all ratios of the stiffness elements  $c_{ij}$  are constant, which implies that anisotropic coefficients and the ratio of the vertical velocities of P- and S-waves must be constant as well.) Although P-wave traveltimes alone cannot be used to separate anisotropy from lateral heterogeneity, moveout of events in image gathers does constrain the vertical gradient of velocity. Sen and Mukherjee (2003) have performed similar analysis in plane wave ( $\tau$ - $p$ ) domain and unlike ( $x$ , $t$ ) NMO, derived interval anisotropy parameters directly.

#### **1.3.4 THE CFP METHOD**

In the Common Focus Point (CFP) method, the goal is to obtain a velocity model that successfully illuminates each subsurface gridpoint (reflection point or CFP) (Berkhout and Verschuur, 2001). For each point, traveltime is calculated to all receiver locations in the recording aperture (Fig. 1.4) and it is used to generate a focusing operator (Fig. 1.5) (Berkhout and Verschuur, 2001). This operator is applied to all shot gathers, and one trace is extracted from each resulting gather (Berkhout and Verschuur, 2001) (see Fig. 1.6a,b). Each extracted trace has the specular reflection contribution from the particular subsurface gridpoint, and each is placed within a trace-gather corresponding to its shot position (Berkhout and Verschuur, 2001). The resulting gather is called a CFP gather (Fig. 1.7), and it represents the one-way time response (Fig. 1.8) for the subsurface point (Berkhout and Verschuur, 2001).



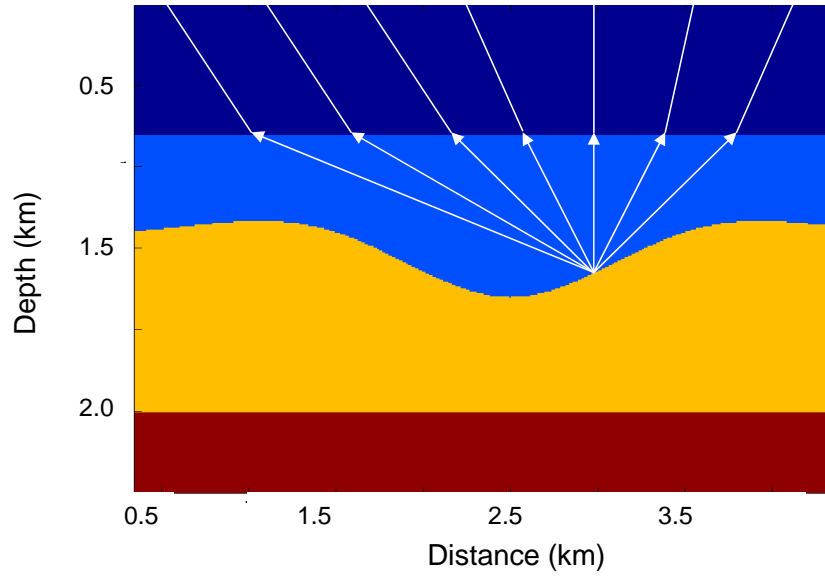


Figure 1.4: Travelttime from a CFP to all receiver positions is used to calculate the operator.

It has been shown by Berkhout and Rietveld (1994), Kabir and Verschuur (1996), and Thorbecke (1997) that for a correct macro model, the time-reversed focusing operator has exactly the same travelttime as the corresponding CFP response for all offsets (principle of equal travelttime) producing zero differential time shift (DTS) between the operator and CFP response (see Fig. 1.9). Any deviation of the DTS from zero-lag indicates a velocity and/or depth error. Since the error is given directly in time for the spatial location of a particular gridpoint, this analysis is done in space and time simultaneously. The CFP domain analysis has been used for anisotropic parameter estimation in VTI media in the offset-time domain (Kumar et al., 2004) as well as in plane wave ( $\tau$ -p) domain

(Ferguson and Sen, 2004) using only P-wave data. Since P-wave data analysis results in velocity-depth ambiguity, Ferguson and Sen (2004) perform joint inversion of P and SV-wave data and successfully obtain depth as well as anisotropic parameters.

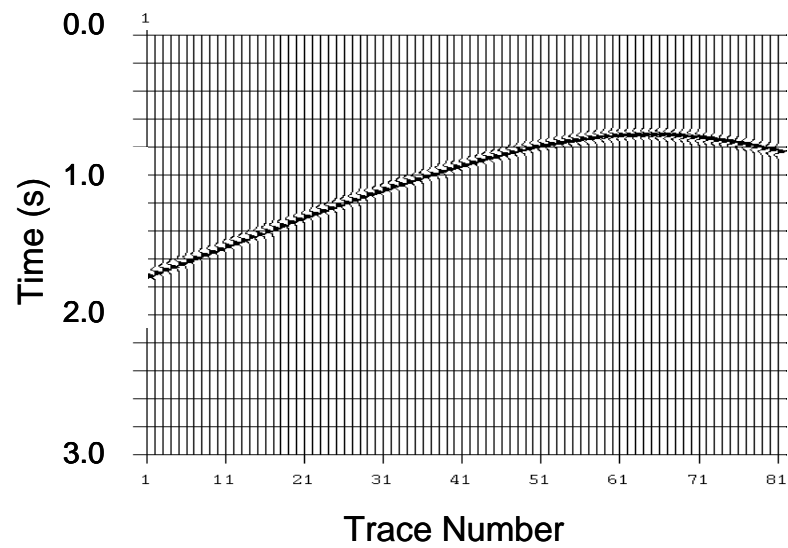


Figure 1.5 Time-reversed focusing operator based on traveltimes computation in assumed model.

### 1.3.5 COMPARISON OF CMP, CIG, CRS AND CFP METHODS

The CFP based differential time shift (DTS) analysis appears to be a natural domain for doing velocity analysis. There exists a direct relationship between traveltimes error and error in depth and phase velocity. The phase velocity in turn depends on anisotropic parameters. The CFP based DTS analysis is performed

before imaging, and then stacking is performed (Kabir, 1997). In CIG based residual curvature analysis (RCA), the analysis is performed after imaging but before stacking (Kabir, 1997). The DTS panel, in contrast to the CIG panel, does not show stretching for far offsets (Kabir, 1997). Error analysis done directly in the time domain allows for more accuracy and relatively easier model updating (Kabir, 1997). In contrast, since in CIG analysis the equation relating traveltimes error to depth error is based on 1D velocity model assumption (Jiao et. al, 2002; Ahmed, 2003), the errors involved are less accurate leading to difficulty in model updating in complex areas. Moreover, since the contribution of anisotropy to traveltimes moveout is small and noticeable only at very far offsets, the choice of CFP based approach appears to be more attractive for anisotropic parameter estimation.

The focusing operator in CFP based analysis is a non-smooth operator and bears all the imprints of complex overburdens above the common reflection point, whereas the CRS operator is a smooth operator and does not bear all imprints of the complex overburden (Bolte, 2003). The data driven CRS operator aimed at migration to zero offset results in smearing of data along boundary, whereas the model driven CFP operator always produces a perfectly focused image (Bolte, 2003). Thus, estimation of anisotropic parameters, which involves error analysis at very far offsets, is well suited in CFP domain. The disadvantage of CFP based

methods over CIG and CRS based methods lies in the high computational cost involved (Kabir, 1997; Bolte, 2003).

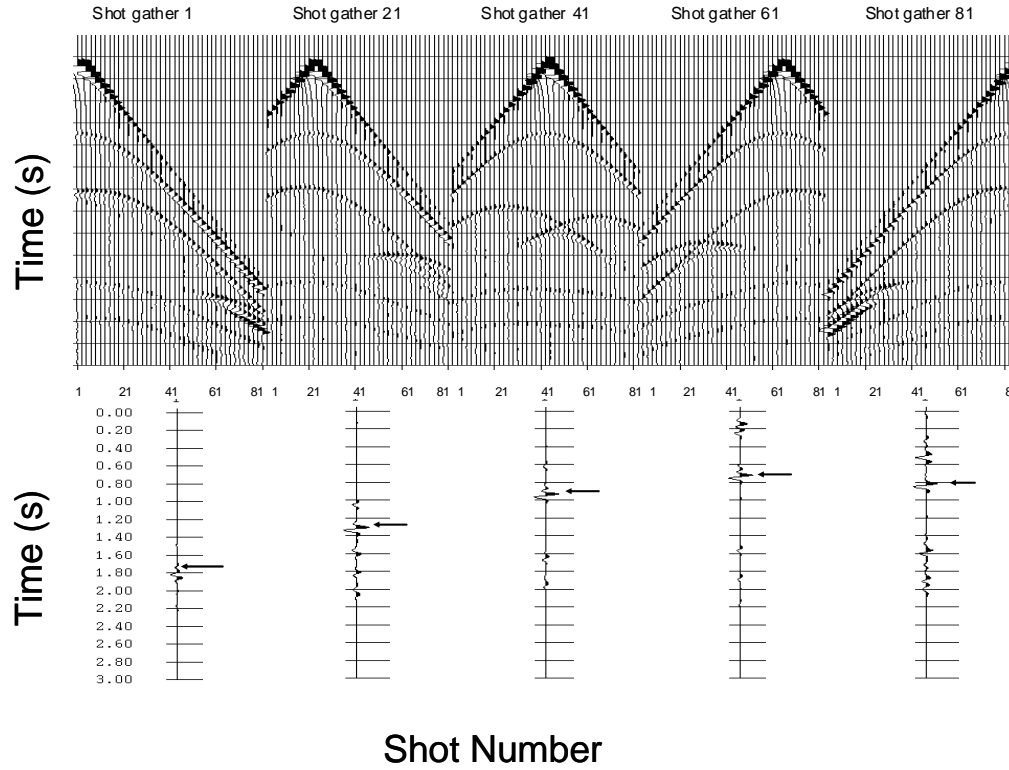


Figure 1.6 (a) Shotgathers from shot 1 to shot 81, (b) The traces corresponding to each shot gather, obtained after application of focusing operator on corresponding shot gather. The arrow marks the event of specular reflection from the given CFP.

#### 1.4 INVERSION AND SENSITIVITY ANALYSIS

If the elastic parameters of the subsurface are known, it is easy to solve the equations governing wave propagation (forward problem) and generate

subsurface images. The process of finding the right elastic parameters from the data (inverse problem) to feed the forward algorithm is not trivial, due mainly to limitations in data acquisition, presence of noise, and non-uniqueness of the method. Depending on the nature of the problem, different inversion algorithms are applied. The inverse problem is broadly categorized as linear or non-linear (Tarantola, 2005). Linear inverse problems can be solved by local optimization methods like steepest descent method or conjugate gradient method (Tarantola, 2005). Non-linear inversion problems are solved by global optimization methods like simulated annealing or genetic algorithm (Sen and Stoffa, 1995). Some non-linear problems can be formulated as linear problems in the vicinity of their solution by making use of first order Taylor series expansion (Menke, 1989; Sen, 2006). Estimation of anisotropic parameters is a non-linear problem. For my research, I formulate the anisotropic parameter estimation problem as a linear problem in the vicinity of a preliminary starting solution and use the steepest descent approach to solve it. The equations are solved in a least squared sense by minimizing an  $L_2$  norm (Menke, 1989).

Seismic data invariably contain noise and/or inadequate information such as limited aperture and limited bandwidth. These factors limit our ability to estimate the anisotropic parameters effectively. It is important to predict our ability or limitations in estimating the parameters under different data acquisition settings and noise conditions. Sensitivity analysis is a useful tool to achieve this. It helps in examining the impact of measurement errors in traveltime data to the estimates of subsurface model parameters. It also includes the theoretical

uncertainty (prediction error) caused by the physics of forward problem. Knowing these, resources of data acquisition can be better applied to give least erroneous estimates.

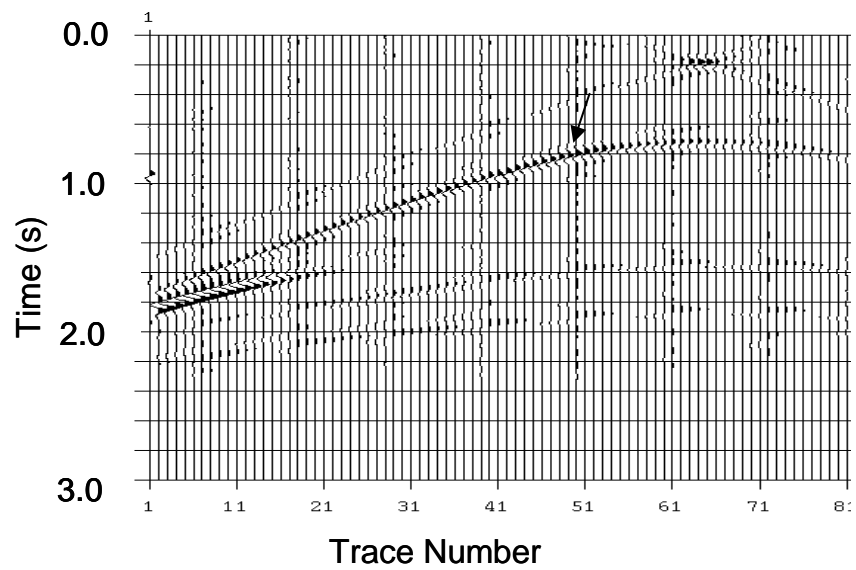


Figure 1.7: CFP response obtained by placing the traces from Fig. 5 at corresponding shot position.

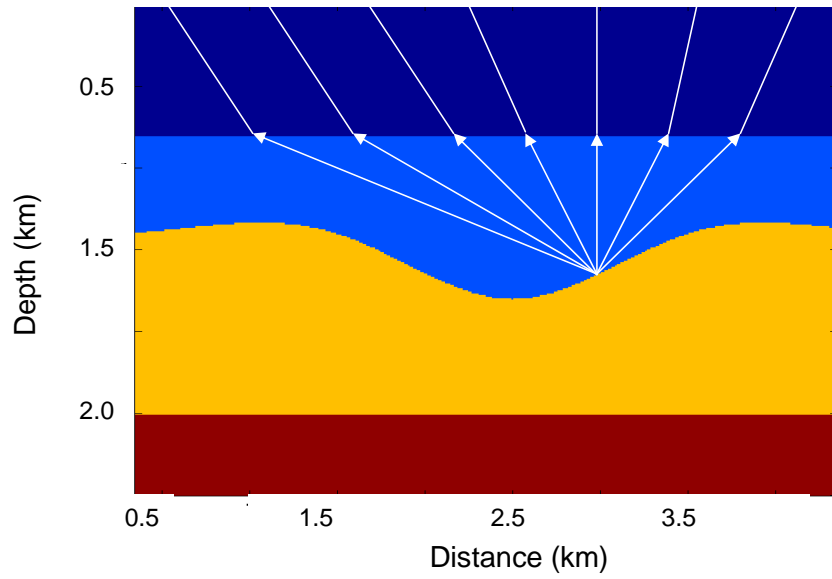


Figure 1.8: CFP response is indicative of trvaeltime from the CFP to shot positions as obtained from data.

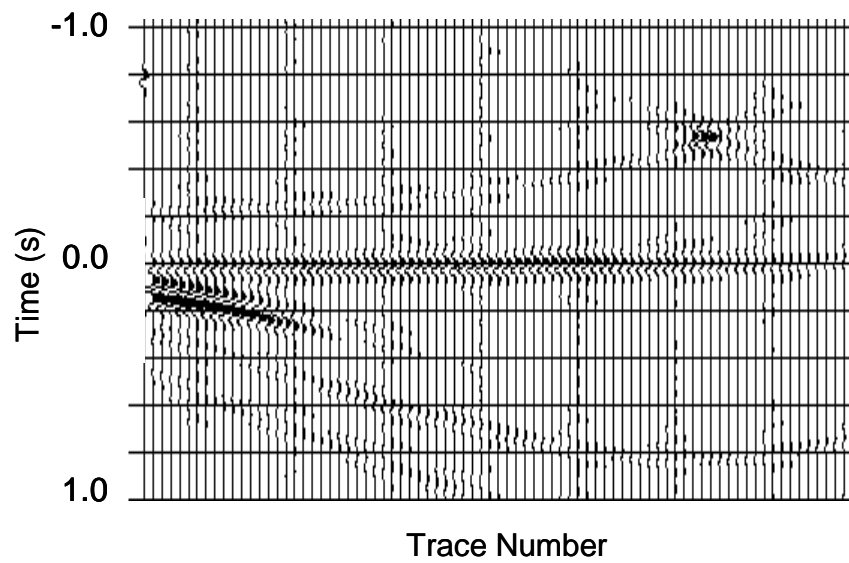


Figure 1.9: Difference of focusing operator and CFP response (DTS panel) for the correct model.

## **1.5 JOINT INVERSION OF P-P AND P-SV DATA**

The use of mode-converted P-Sv data has gained popularity with the advent of Ocean Bottom Cable (OBC) technology and Vertical Seismic Profiling (VSPs) technology (Barr, 1997; Granli et al., 1999; Jin et al., 2000; Yuan, 2001) as pure Sv-Sv mode data are rare and has several acquisition, propagation and processing related problems. Shear waves are more sensitive to anisotropy than P-waves and help in constraining anisotropic parameter estimates needed for imaging. When both P-wave and Sv-wave observations are taken together, we have a situation like having more number of simultaneous equations to solve more unknowns. The conventional CMP based methods cannot deal with P-Sv data due to asymmetrical ray path. The common conversion point (CCP) binning (Harrison, 1992) and P-S DMO are only partial solutions to asymmetry problem and face difficulty with large dimension structural data (Harrison, 1992). The CFP based analysis avoids all such problems. Since CFP method is based on separate focusing of seismic data at the source and receiver side, the operator for focusing in detection may address another wave type than the operator for focusing in emission (Berkhout, 1997).

## **1.6 THESIS OBJECTIVE**

The objective of this thesis is to quantitatively assess the advantages or limitations of Common Focus Point (CFP) domain prestack velocity analysis in estimating the anisotropic parameters for a transversely isotropic (TI) media. This



assessment is done under different experimental settings including the use of mode converted data.

In the current chapter, I have defined and introduced the key concepts like anisotropy, migration velocity analysis, inversion, sensitivity analysis etc. that are integral to my work. I have also provided in this chapter the objective and organization of my dissertation.

In Chapter 2, I present the theory, implementation and advantages or disadvantages of Common Focus Point (CFP) analysis as compared to other popular methods are presented. I extend the space-time domain implementation of CFP analysis for estimation of anisotropy in complex geological areas like Canadian Foothills. I also present an example of anisotropic parameter estimation for Canadian Foothills synthetic P-mode data.

In Chapter 3, I present the theory and results of sensitivity analysis for TI medium under different experimental settings. The results quantitatively establish the advantage of joint inversion of P-P and P-Sv over the conventional inversion of P-P only data in constraining the depth and anisotropic parameters. I also explore other experimental settings including tilted TI media that improve constraint on estimated anisotropic parameters.

In Chapter 4, I present the theory and advantages of CFP domain analysis for mode converted P-Sv data. I also present the results of joint inversion for a synthetic P-P and P-Sv data in CFP domain for a model based on the geology of Blackfoot field, but with the layers and TI symmetry axis dipping.

In Chapter 5, I present a brief summary of the research. I also suggest some direction for future research on this subject.

## Chapter 2: Elastic Parameter Estimation in Common Focus Point Domain

### 2.1 INTRODUCTION

In areas of complex geology such as the Canadian Foothills, estimation of subsurface elastic parameters to be used in seismic imaging is not trivial. The Common Focus Point (CFP) method provides a new domain of prestack velocity analysis where the error in the velocity model corresponding to each reflection point can be directly obtained in two-way reflection time. This allows easier and more precise model updates (Berkhout, 1997; Kabir, 1997). The CFP (Berkhout, 1997; Thorbecke, 1997; Kabir, 1997; Berkhout and Verschuur, 2001) method of imaging based velocity analysis is based on seismic-data focusing at a number of analysis points in the subsurface. These points are selected from CMP stacked images such that they correspond to visible reflections. For each point along the profile, in a layer-stripping fashion, beginning with the shallowest point, data recorded at each receiver location are reverse propagated from the recording surface to the analysis point, and models of each source are forward propagated from their corresponding source-locations to the same point. There they are cross-correlated in time. A gather of source data at an analysis point is termed the *focus operator* for that point, and the corresponding gather of receiver data is termed a *common focus point gather*. Where the background model used for propagation of sources and receivers is correct, cross correlation yields reflection energy lined up at zero-time. Error in the model results in non-alignment or *differential time-shift*

(DTS) (Berkhout, 1992; 1997; Rietveld, 1995; Thorbecke, 1997; Kabir, 1997). DTS itself is a measure of error in depth and error in seismic velocity, and as such, they may be inverted to update the velocity model.

To estimate velocity heterogeneity in isotropic media, Kabir (1997) implements the CFP method in the space-time domain. For homogeneous anisotropic media, Ferguson and Sen (2004) propose plane-wave domain implementation of this technique for anisotropic parameter estimation when both P and Sv-wave data are independently available. Velocity analysis in the plane wave domain is advantageous as it avoids the problem of multipathing and triplication common in the shot domain, and the measured DTSs directly relate ray parameter to error in both vertical slowness and layer thickness (Ferguson and Sen, 2004).

Conventional plane wave domain implementation of depth migration, however, may fail to image steep structures such as the base of tilted TI layers (Ferguson and Margrave, 2002), while ray based methods that rely on computation of group velocity can succeed (Kumar et al., 2004). This imaging problem is an outcome of the fact that for tilted TI symmetry axis, some horizontal slowness values correspond to two phase angles as shown in Figure 2.1. As a result, the impulse response created by phase shifting as shown in Figure 2.2, does not track the theoretical response shown by dashed line beyond  $90^0$  as it lies in the evanescent region beyond the critical angle (Ferguson and Margrave, 2002). Although such problems can be avoided by proper modification of the plane wave migration methods (e.g. Hale, Hill and Stefani, 1992), I feel that it is

worthwhile to extend the CFP method of anisotropic parameter estimation in the space-time domain.

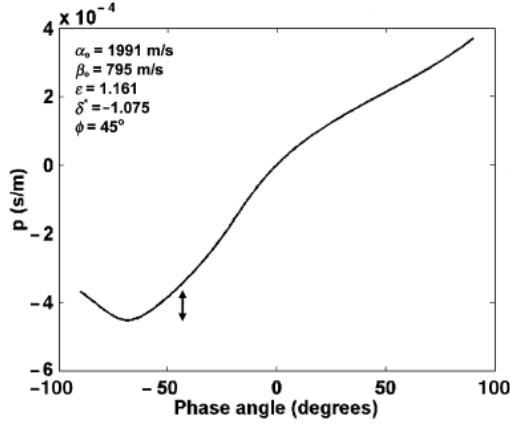


Figure 2.1: Plot of slowness  $p=k_x/\omega$  versus phase angle  $\theta$  for dipping TI medium. Each value of  $p$  in the range indicated by the arrow corresponds to two phase angles. Values outside of this range are uniquely defined (from Ferguson and Margrave, 2002).

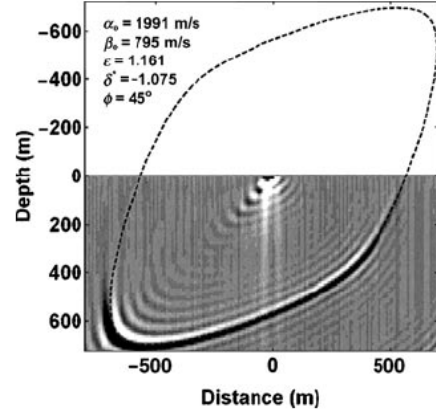


Figure 2.2: The impulse response for phase shift in a homogeneous TI medium with an axis of symmetry of  $45^\circ$ . The dashed curve shows the theoretical response. The impulse response does not track the theoretical response beyond  $90^\circ$  (left side of figure) (from Ferguson and Margrave, 2002).

For a TI medium, seismic velocity is defined by five independent elements of the elasticity tensor (Crampin, 1984). Thomsen (1986) rearranges the five parameters so that two of the five parameters are in units of velocity rather than elasticity. Thomsen's (1986) parameters are  $\alpha_0$  (vertical P-wave velocity),  $\beta_0$  (vertical S-wave velocity),  $\varepsilon$  (a measure of P-wave anisotropy),  $\delta$  (parameter controlling near vertical propagation) and  $\gamma$  (a measure of S-wave anisotropy). By vertical incidence we measure incidence parallel to the axis of symmetry for VTI

medium. P-wave and SV-wave propagation in the plane containing the symmetry axis does not depend on parameter  $\gamma$ , and depends, therefore, on parameters  $\alpha_0$ ,  $\beta_0$ ,  $\epsilon$  and  $\delta$  alone (Thomsen, 1986). Further simplification for P-wave propagation follows from the assumption of ‘weak’ anisotropy where dependence on  $\beta_0$  is negligible (Thomsen, 1986). Hence, the anisotropy of the thrust sheet can be characterized fully by three elastic parameters  $\alpha_0$ ,  $\epsilon$ ,  $\delta$  and thickness.

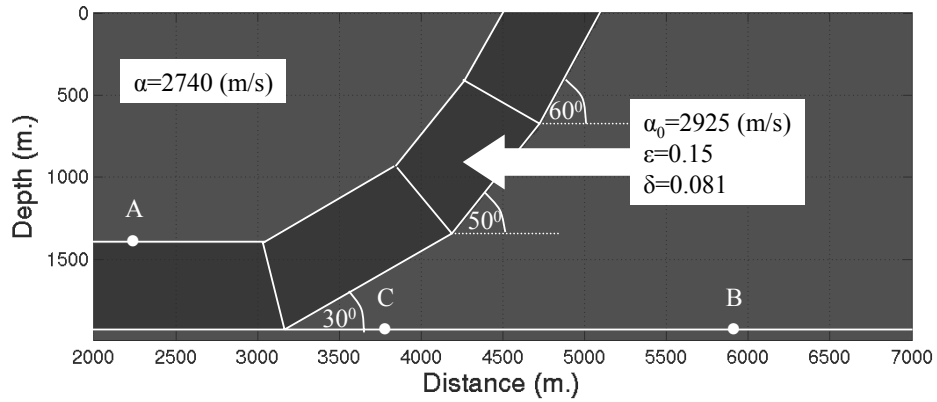


Figure 2.3: Anisotropic thrust sheet embedded in a homogeneous, isotropic medium.

I use the space-time domain implementation of CFP analysis (Kabir, 1997) to estimate anisotropic parameters for weak TI media in the Canadian Foothills model. This model draws inspiration from the geology encountered in Canadian foothills where exploration targets often lie below a thrust shale layer (Leslie and Lawton, 1998, Fei et al., 1998). As shown in Figure 2.3, the model consists of a weak TI thrust sheet with an axis of symmetry vertical to thrust sheet that is made up of four blocks with dips 0, 30, 50 and 60 degrees from vertical

respectively, and these are embedded in a background medium that is isotropic. All four blocks are homogeneous, and the TI symmetry axis for each block is orthogonal to the bedding within. The reflector below the thrust sheet represents a horizontal target-layer.

Based on this model, seismic data used in this paper were generated by finite difference modeling techniques (Fei et al., 1998). Data consist of 86 shot gathers spaced 60m apart. Each shot has 201 receivers spaced 20m apart with a mean offset of zero and total spread of 4000m. The recording geometry is split spread, and the central receiver is coincident with shot location. Figure 2.4 shows the zero-offset gather for this data set. On this gather, the top of the thrust-sheet, the near flat base reflector and the pull-ups on base reflector are easily noticed at 1.4 s and ~ 4000 m. We use these analysis points later to estimate the velocity model to be used for migration

Velocity analysis and migration based on assumed isotropy produces false pull-ups in reflection time below overthrust sediments (Leslie and Lawton, 1998), and this can be seen below the highly dipping portions of thrust sheet in Figure 2.5. The apparent anticline is due to the neglect of anisotropy in thrust sheet above rather than true geology. Figure 2.6 shows the ray tracing for an impulse response from focus point C. It can be seen that the direction of ray at location X in the thrust-sheet is nearly parallel to the TI symmetry axis (slow direction) whereas at location Y the ray direction is nearly perpendicular to TI symmetry axis (fast direction). Within the thrust-sheet if we go from X to Y, we see an increase in angle of propagation with respect to TI symmetry axis and hence an increase in

the group velocity resulting in smaller traveltimes with respect to isotropic medium. Hence isotropic migration using near vertical (slow direction) P-wave velocity, results in false anticline structure for the flat bed below the thrust-sheet. To account for anisotropy in migration, I must determine anisotropic parameters for the thrust sheet. Anisotropic velocity analysis is difficult for TI layer due to the irresolvable velocity-depth ambiguity for P-wave data (Tsvankin and Thomsen, 1994; Tsvankin and Thomsen, 1995; Sen and Mukherjee, 2003). To avoid this problem, I make some a priori assumptions about the model – (i) the background medium is isotropic, (ii) the TTI blocks are homogeneous with the symmetry axis orthogonal to bedding, and (iii) the reflector below the thrust-sheet is horizontal and coincident with the base of horizontal block of thrust sheet. In real situations, I hope to obtain the a priori information from geology or well-logs.

## **2.2 COMMON FOCUS POINT (CFP) VELOCITY ANALYSIS**

It is easier to understand the CFP technique starting with the WRW framework (Berkhout, 1982). In this framework the discrete version of the model for primary wavefields is formulated in the source array coordinates, receiver array coordinates and frequency. The space-time domain implementation of CFP technique (Berkhout, 1997) can be derived from WRW framework.

### **2.2.1 WRW FORMULATION**

After removal of the direct wave, influence of the free surface and internal multiples, the seismic reflection data  $\mathbf{P}_0(z_r, z_s)$  can be expressed in terms of



discrete propagation and reflection operators (Berkhout, 1980) for each temporal Fourier (or Laplace) component

$$\mathbf{P}_0(z_r, z_s) = \mathbf{D}^-(z_r) \mathbf{X}_0(z_r, z_s) \mathbf{S}^+(z_s), \quad (2.1)$$

where each column of source matrix  $\mathbf{S}^+(z_s)$  defines the downgoing source wavefield at the depth level  $z_s$  for one source array, and the corresponding columns of  $\mathbf{P}_0(z_r, z_s)$  define the resulting upgoing wavefields that are measured at the receiver array at depth level  $z_r$ .  $\mathbf{D}^-(z_r)$  is the detector array.  $\mathbf{X}_0(z_r, z_s)$  is the transfer function one element of which defines the upgoing wavefield at one individual receiver element due to a unit source at one individual source point.

This function is defined as

$$\mathbf{X}_0(z_r, z_s) = \sum_{m=1}^M [\mathbf{W}^-(z_r, z_m) \mathbf{R}^+(z_m) \mathbf{W}^+(z_m, z_s)] \quad (2.2)$$

where columns of  $\mathbf{W}^+(z_m, z_s)$  and rows of  $\mathbf{W}^-(z_r, z_m)$  define the propagation respectively between  $z_s$  and  $z_m$  and between  $z_m$  and  $z_r$ .  $\mathbf{R}^+(z_m)$  defines the reflection operator for the downgoing wavefields at depth level  $z_m$ .

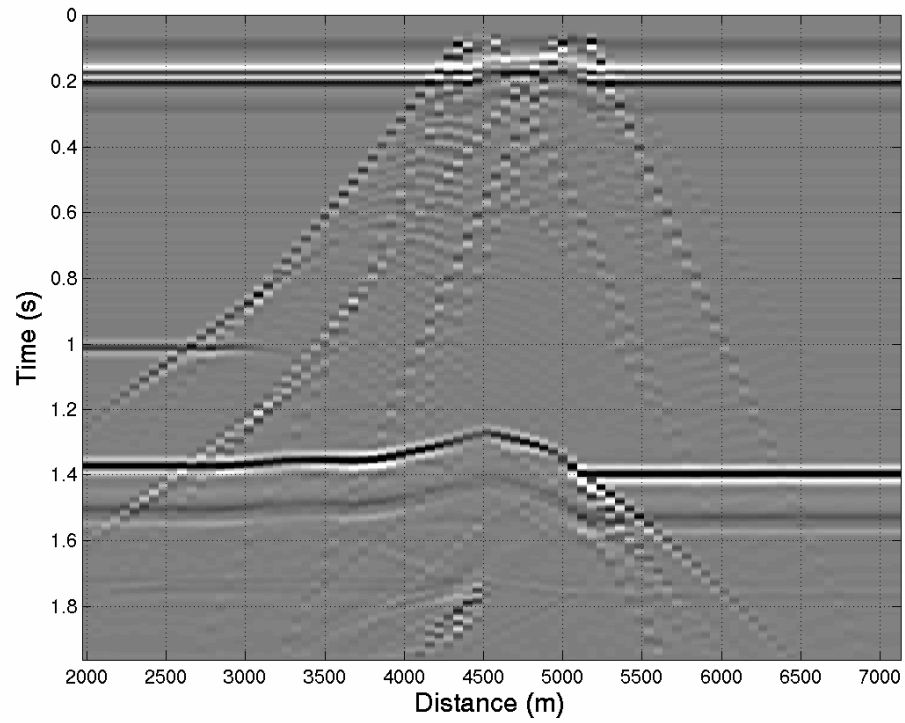


Figure 2.4: Zero-offset gather. The pull up in the base reflector (inside the ellipse) is evident and is due to the fact that it lies below highly dipping thrust-sheet.

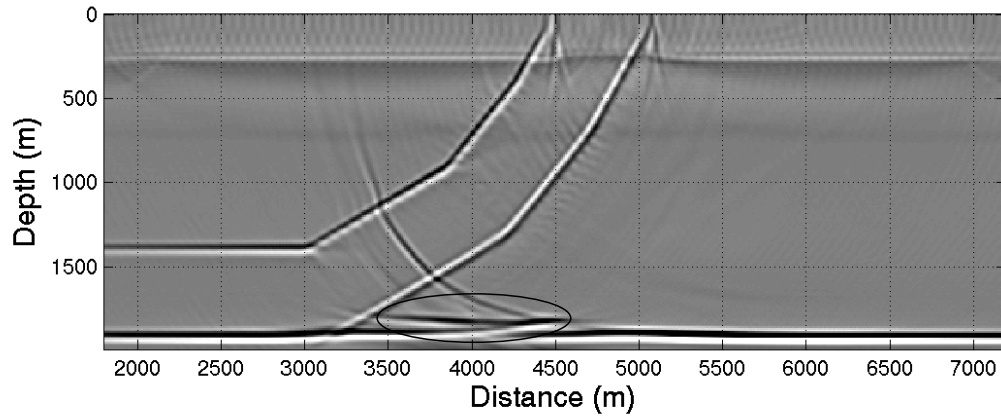


Figure 2.5: Migrated image using isotropic velocity model. The poor image of base reflector (inside the ellipse) below the dipping thrust-sheet is due to isotropic assumption in imaging.

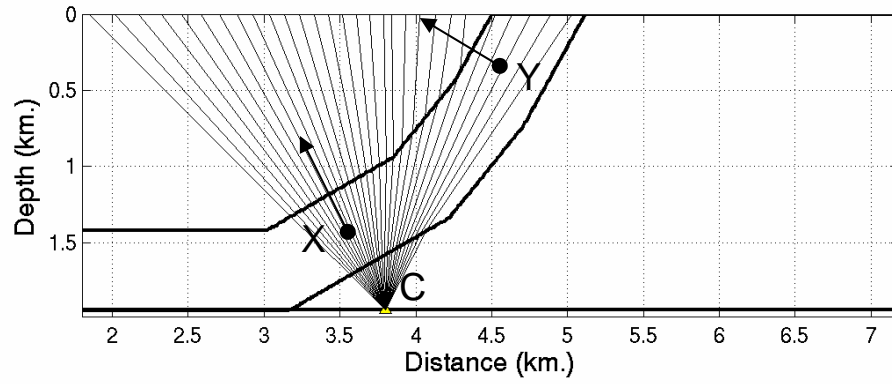


Figure 2.6: Ray tracing from focus point 'C' (Figure 2.3) to the source-receiver locations. The ray direction with respect to TI symmetry axis shown by arrow varies from near parallel at X to near horizontal at Y.

In first step of migration or velocity analysis, an operator  $\mathbf{F}_j(z_s, z_m)$  is created that synthesizes the source wavefield in such a way that only one particular subsurface gridpoint  $x_j$  at depth  $z_m$  is illuminated. Operator from equation (2.6)  $\mathbf{F}_j(z_s, z_m)$  is applied to the primary data  $\mathbf{P}_0(z_r, z_s)$  (equation 2.1) to generate a CFP gather

$$\Delta \mathbf{P}_{0,j}(z_r, z_m) = \mathbf{P}_0(z_r, z_s) \mathbf{F}_j(z_s, z_m). \quad (2.3)$$

In the above equation only the response from a single level of reflector is considered for the sake of simplicity. This focusing operator in emission is thus defined such that

$$\mathbf{I}_j(z_m) = \mathbf{W}^+(z_m, z_s) \mathbf{S}^+(z_s) \mathbf{F}_j(z_s, z_m), \quad (2.4)$$

with  $\mathbf{I}_j(z_m) = [0, 0, 0, \dots, 0, 1, 0, \dots, 0]^T$ , where 1 is positioned at the  $j^{\text{th}}$  location of this vector and corresponds to the grid point to be focused at the  $m^{\text{th}}$  depth.

The focusing operator may be defined in terms of downward propagator matrix  $\mathbf{W}^+(z_m, z_s)$  and the source matrix  $\mathbf{S}^+(z_s)$  by rewriting equation (2.3) as

$$\mathbf{F}_j(z_s, z_m) = [\mathbf{W}^+(z_m, z_s) \mathbf{S}^+(z_s)]^{-1} \mathbf{I}_j(z_m). \quad (2.5)$$

Assuming that the influence of the source matrix  $\mathbf{S}^+(z_s)$  has been removed from the data in advance by using the knowledge of source signature and deconvolution, equation (2.4) can be written as

$$\mathbf{F}_j(z_s, z_m) = [\mathbf{W}^+(z_m, z_s)]^{-1} \mathbf{I}_j(z_m). \quad (2.6)$$

It is not possible to find an exact inverse operator in space-frequency domain as it explodes in evanescent region. Hence, by using matched filter theory (Wapenaar and Berkhout, 1989) a stable and good approximation of the focusing operator is given as

$$\mathbf{F}_j(z_s, z_m) \approx [\mathbf{W}^-(z_m, z_s)]^* \mathbf{I}_j(z_m) , \quad (2.7)$$

as it represents the impulse response of  $j^{\text{th}}$  focus point at  $m^{\text{th}}$  depth. The complex conjugate of the focusing operator can be written as

$$\mathbf{F}_j(z_s, z_m)^* \approx \mathbf{W}^-(z_m, z_s) \mathbf{I}_j(z_m) \quad (2.8)$$

which is stable and when represented in time domain, defines a time-reversed version of the focusing operator. This operator defines one way propagation time from the gridpoint at  $x_j$  at the level  $z_m$  up to the surface at level  $z_s$ .

The result of application of this operator  $\mathbf{F}_j(z_s, z_m)^*$  (Equation (2.8)) on primary data matrix  $\mathbf{P}_0(z_r, z_s)$  (Equation 2.1) for one reflector is called CFP response and is written as

$$\Delta \mathbf{P}_{0,j}(z_r, z_m) = \mathbf{D}^-(z_r) \mathbf{W}^-(z_r, z_m) \mathbf{R}^+(z_m) \mathbf{I}_j(z_m). \quad (2.9)$$

After removing the influence of the receiver matrix  $\mathbf{D}^-(z_r)$  from the data by addressing the detector properties during preprocessing and by including the directivity in the propagation matrices, the related focus point response can be written as

$$\Delta \mathbf{P}_{0,j}(z_r, z_m) = \mathbf{W}^-(z_r, z_m) \mathbf{R}_j(z_m) \quad (2.10)$$

where,  $\mathbf{R}_j(z_m) = \mathbf{R}^+(z_m) \mathbf{I}_j(z_m)$ .

Once the matrix operators  $\mathbf{S}^+(z_s)$  and  $\mathbf{D}^-(z_r)$  have been removed and the sources and receivers are brought to the same level ( $z_r = z_s$ ), then assuming the correct macro model and the coinciding source and receiver locations, the comparison of equations (2.8) and (2.10) give following fundamental observations (Berkhout, 1997):

- The time-reversed focusing operator and the related response have equal traveltimes at all offsets.
- The local dip angle has no influence on the traveltimes of the response and only influences amplitudes.
- A reflectivity function may be computed by cross correlating the focus point response with the related time-reversed focusing operator.

Thus the CFP concept can be used for migration velocity analysis (MVA) as well as amplitude variation with offset (AVO) analysis. The CFP method of velocity analysis is flexible and can be adapted to space-time domain (Kabir, 1997) or plane wave ( $\tau$ - $p$ ) domain (Ferguson and Sen, 2004). The space-time domain velocity analysis can be thought of as an intermediate step of Kirchhoff migration. The plane wave domain velocity analysis can be thought of as a variant of downward continuation where error is obtained in time and not in depth. The model can be built either by layer-stripping approach, where each layer is defined by a unique set of parameters or by downward continuation and identification of reflection point at each depth location and subsequently updating the parameters locally. The CFP method can be adapted to be model independent (Bolte, 2003) or model dependent (Kabir, 1997). Though the model independent approach may yield models that do not make sense geologically, it is useful in redatuming the seismic data in a full prestack sense towards one of the reflectors below a complex overburden (Hindriks and Verschuur, 2001; Bolte and Verschuur, 2001; Kelamis et al., 2002). The focusing operator for model driven analysis can be

obtained either by traveltimes computation or by wavefield extrapolation from reflection point to source-receiver geometry. The space-time domain implementation based on traveltimes computation has advantage in handling irregular acquisition geometry. Also identification of reflection points in the model space after initial stacking makes the number of analysis points sparse when compared to the total number of grid-points based on uniform spatial sampling. The CFP domain is advantageous for converted wave analysis too where separate wavefield synthesis at source side and receiver side allows treating the two types of waves separately. This avoids the need to calculate common conversion point (CCP).

### **2.2.2 CFP SYNTHESIS IN SPACE-TIME DOMAIN**

Like any prestack domain migration, CFP domain migration treats the subsurface reflectors as superposition of several point diffractors. Each point diffractor is called a common focus point (CFP) and is addressed separately. The final subsurface reflectivity image is constructed as superposition of image of each CFP at its corresponding spatial location. For each CFP, imaging is split in two steps – (i) focusing in detection followed by (ii) focusing in emission or vice versa (see Figure 2.7). This provides a new domain of velocity analysis which is in between the two domains, i.e. before applying the second focusing step. The operator that facilitates the first focusing step is called focusing operator.

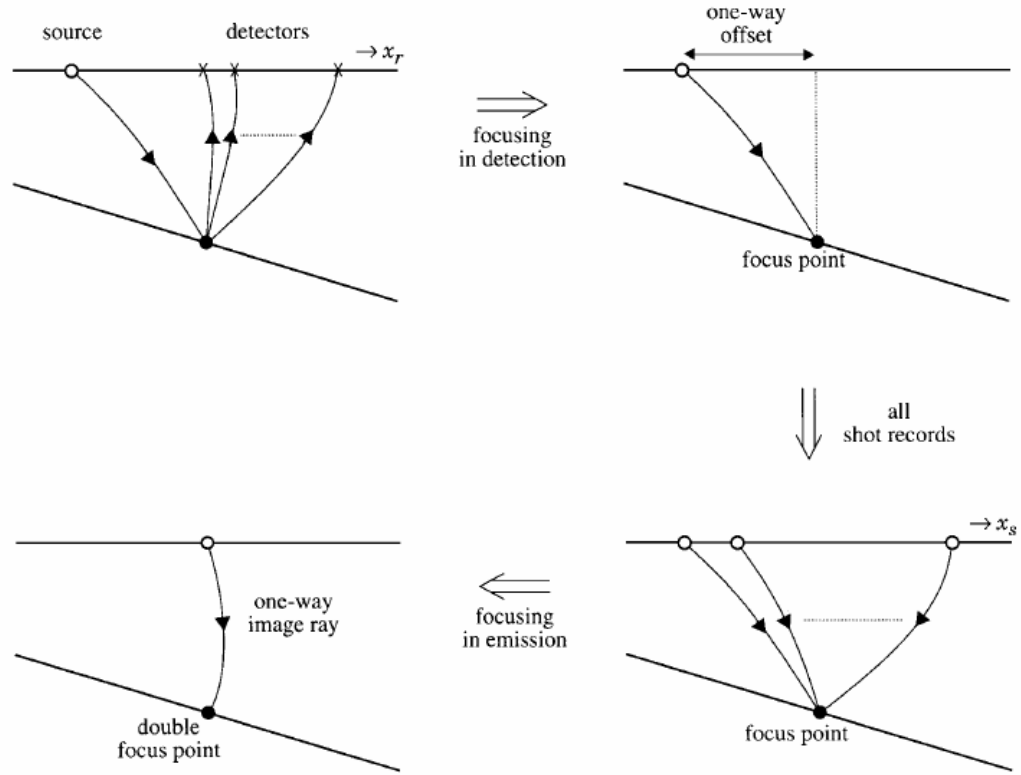


Figure 2.7: In the first focusing step, each shot record is transformed to one event of the focus-point response (Fresnel-zone stacking). In the second focusing step, all events in the focus point response are aligned at the one-way image time, followed by weighted superposition (CFP stacking). Note that here one-way image ray connects two points with the same lateral position; note also that the traveltime along this one-way image ray defines one-way image time (from Berkhout, 1997).

In time domain, the focusing operator (equation 2.8) defines one way propagation time from the gridpoint at  $x_j$  at the level  $z_m$  up to the surface at level  $z_s$ . For each reflection point, e.g. point C in Figure 2.3, a focusing operator (Fig. 2.8 (a)) is generated based on traveltime calculation from the focus point to all



receiver locations (Figure 2.6) in the recording aperture (Berkhout and Verschuur, 2001). This operator is applied to all shot gathers, and one trace is extracted from each resulting gather (Berkhout and Verschuur, 2001). Each extracted trace has the specular reflection contribution from the particular subsurface gridpoint, and each is placed within a trace-gather corresponding to its shot position (Berkhout and Verschuur, 2001). The resulting gather is called a CFP gather (Figure 2.8 (b)), and it represents the one-way time response for the subsurface point (Berkhout and Verschuur, 2001).

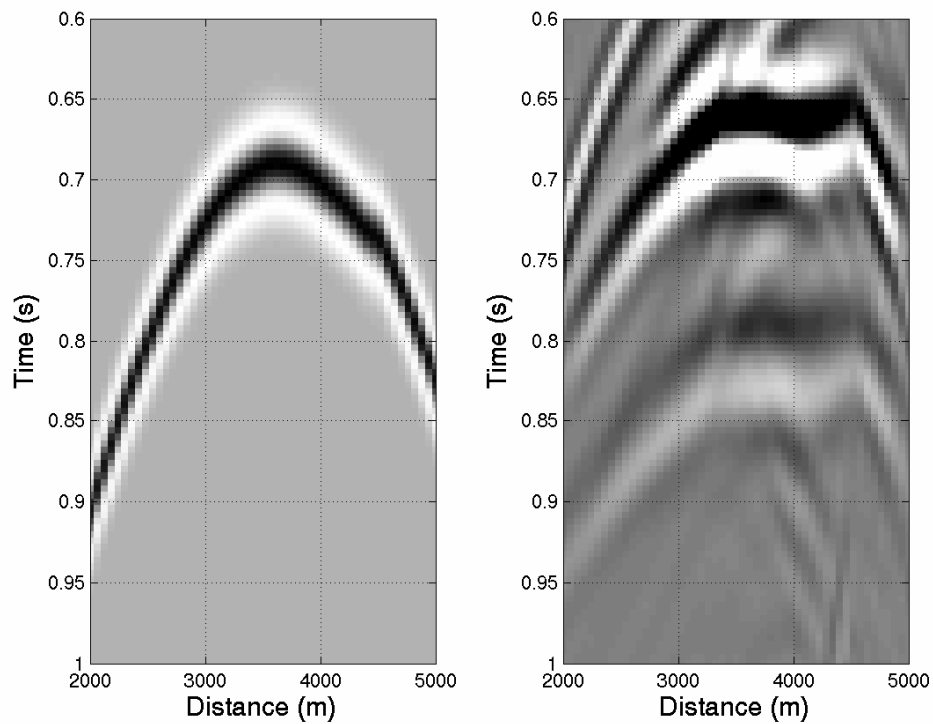


Figure 2.8 (a) CFP operator; (b) CFP gather for point 'C' (Figure 2.3) corresponding to the initial-guess model. Differences in traveltimes to the peak energy in the CFP operator and gather indicate error in the model.

It has been shown by Berkhout and Rietveld (1994), Kabir and Verschuur (1996), and Thorbecke (1997) that for a correct macro model, the time-reversed focusing operator has exactly the same traveltimes as the corresponding CFP response for all offsets (principle of equal traveltimes) producing zero differential time shift (DTS) between the operator and CFP response. Any deviation of the DTS from zero-lag indicates a velocity and/or depth error. Since the error is given directly in time for the spatial location of a particular gridpoint, this analysis is done in space and time simultaneously.

### **2.2.3 CFP SYNTHESIS IN PLANE WAVE DOMAIN**

Ferguson and Sen (2004) use the CFP method in plane wave domain to estimate the elastic parameters of anisotropic media using joint inversion of P and Sv wave traveltimes. Reflection points (CFPs) are selected in the zone of interest, and focusing operators are used to back propagate the reflection data to the CFPs. The resulting CFP gathers are then cross-correlated in time with their corresponding focusing operators (computed by forward propagating models of the seismic sources) in the radon ( $\tau$ -p) domain. For operators that exactly mimic wave propagation from the source and receiver locations to the CFP, energy corresponding to specular reflection aligns at zero-lag on the moveout corrected CFP gather. Misalignment, or differential time shift (DTS), is the result of error in estimating the heterogeneity or anisotropy of the medium above. In anisotropic media, the elastic parameters of the medium above can be picked as DTSs in the

$(\tau-p)$  domain. DTSs are time shifts ( $\Delta\tau$ ) in the  $(\tau-p)$  domain, and they relate ray parameter  $p$ , error in vertical slowness  $q$ , and error in layer thickness  $z$ . Least squares inversion can be used to estimate the anisotropic parameters using a Taylor series expansion of  $q$  in the initial values of anisotropic parameters.

### 2.3 TRAVELTIME CALCULATION IN TTI MEDIA

An integral part of CFP analysis is computation of focusing operator for a given model. The focusing operator can be computed either by minimum traveltime calculation or wavefield extrapolation from reflection point to source-receiver location. For the estimation of anisotropic parameters for foothills model, I use computation of minimum traveltimes from the reflection point to the recording surface using brute force mapping scheme (Schneider et al., 1992; Faria and Stoffa, 1994; Kumar et al., 2004). The model space is comprised of grid points of small finite dimensions. Each grid point has a set of elastic parameters associated with it. At each grid point, the approximate anisotropic group velocity is computed using the following Fourier based three-term cosine series expansion (Byun et al., 1989).

$$v_g^{-2}(\phi) = a_1 + a_2 \cos^2 \phi - a_3 \cos^4 \phi, \quad (2.11)$$

where  $v_g(\phi)$  is the group velocity in the direction that makes angle  $\phi$  with respect to TI symmetry axis, and  $a_1$ ,  $a_2$  and  $a_3$  are the coefficients needed to compute group velocity in an arbitrary direction. These coefficients are obtained by solving the simultaneous equations for group velocities at propagation

directions of 0, 90 and 45 degrees with respect to TI symmetry axis (Faria and Stoffa, 1994).

$$\begin{aligned}
 a_1 &= \frac{1}{\alpha_0^2(1+2\varepsilon)}, \\
 a_2 &= \frac{1}{\alpha_0^2} + a_3 - a_1 \\
 a_3 &= \frac{4}{v_g^2(45)} - 2a_1 - \frac{2}{\alpha_0^2}
 \end{aligned} \tag{2.12}$$

Kumar et al., (2004) propose a slight modification in group velocity expression to account for the tilt in symmetry axis (Equation 2.13).

$$v_g^{-2}(\phi) = a_1 + a_2 \cos^2(\phi - \theta) - a_3 \cos^4(\phi - \theta), \tag{2.13}$$

where,  $\theta$  is the magnitude of anticlockwise tilt in the TI axis of symmetry while  $v_g$ ,  $\phi$ ,  $a_1$ ,  $a_2$  and  $a_3$  are computed according to Equations 2.11 and 2.12.

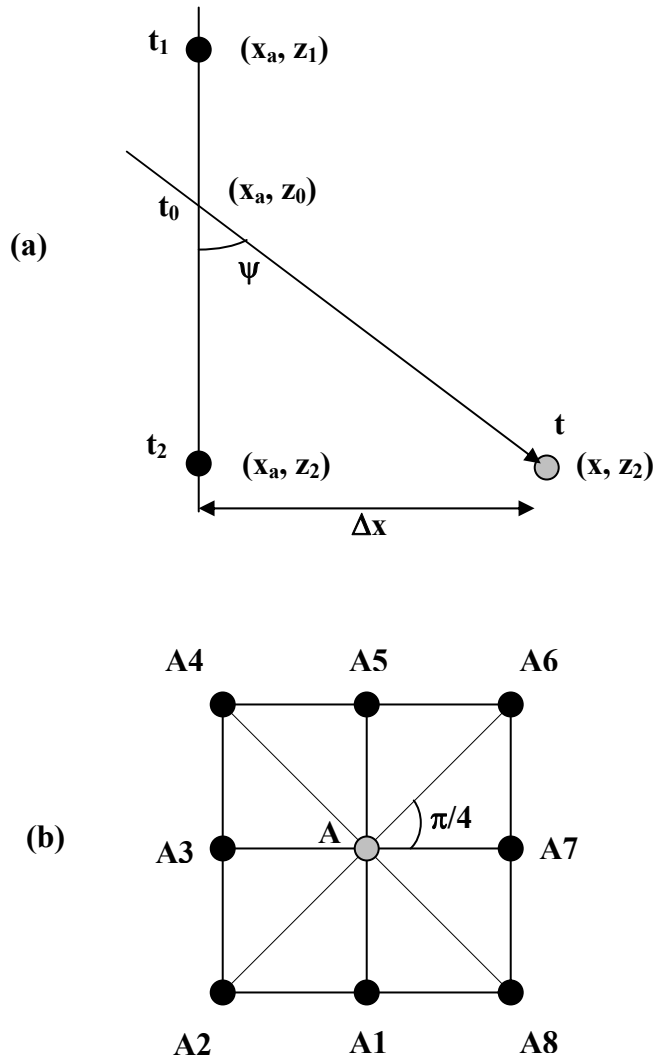


Figure 2.9: (a) Single traveltimes calculation scheme. Traveltimes  $t_1$  and  $t_2$  are known and  $t_0$  is calculated to minimize the total traveltimes  $t$ , (b) For a given point of interest  $A$ , eight traveltimes can be computed based on eight gridpoints surrounding it. The minimum of these provide the first arrival traveltimes (from Kumar et al., 2004).

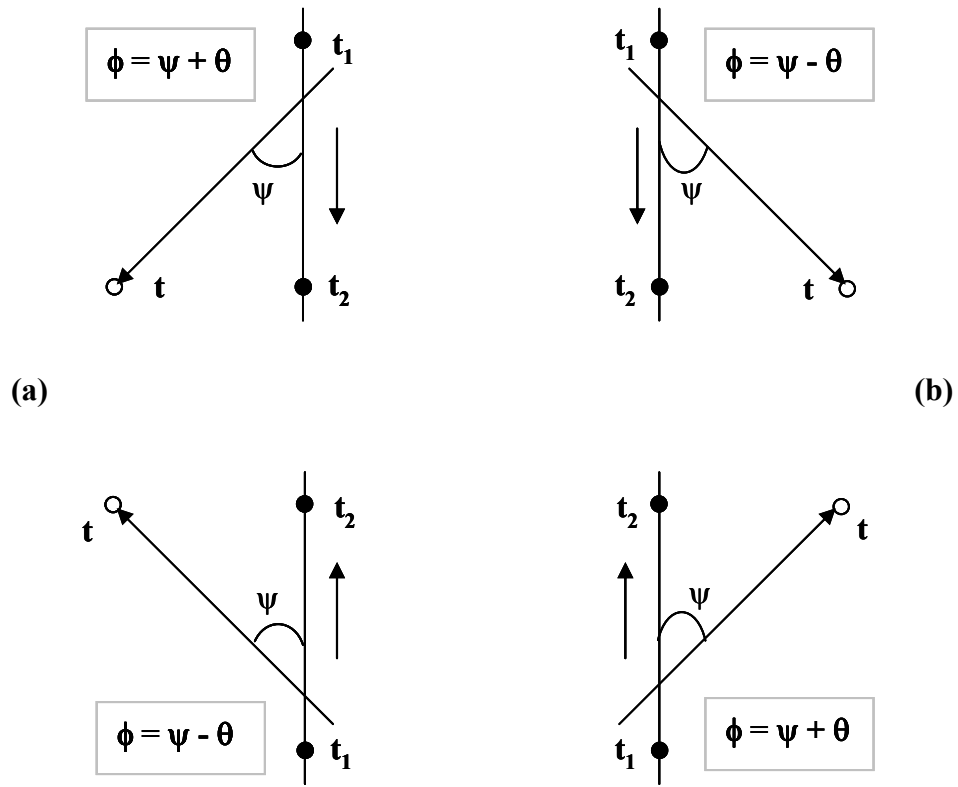


Figure 2.10 (a),(b): Traveltime mapping scheme: traveltimes for grid points on the left side of the source (a) and on the right side of the source (b) are calculated column-by-column until the left and right edge of the grid, correspondingly, are reached. (after Faria and Stoffa, 1994).

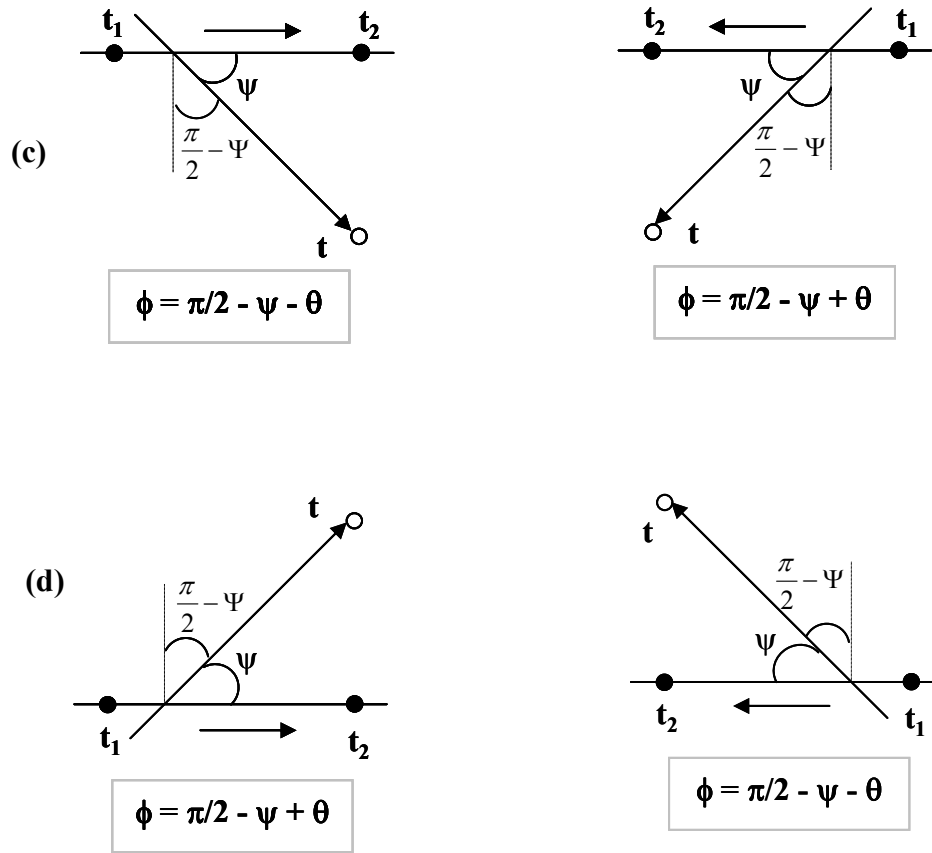


Figure 2.10 (c),(d): Traveltime mapping scheme: from left to right and right to left away from the source column, moving from the source level to the bottom of the grid (c) and from the source level to the top of the grid (after Faria and Stoffa, 1994).

For traveltime mapping, a brute force mapping scheme, proposed by Schneider et al. (1992) is used to handle complicated velocity distribution. To begin with, traveltimes at all gridpoints in the source column (or row) and the six neighboring points in adjacent columns are calculated by using slow direction P-

wave velocity and straight raypaths. Next, traveltimes computation advances across the model space, one column (or row) at a time, starting from the column containing the source (Faria and Stoffa, 1994; Kumar et al., 2004). The traveltimes  $t$  at each gridpoint is obtained by minimizing it using known traveltimes  $t_1$  and  $t_2$  at two neighboring gridpoints as shown in Figure 2.9 (a). This is repeated for all eight neighboring pairs of gridpoints (Figure 2.9 (b)) and the minimum of the eight cases is selected. To correct the possible errors introduced in initial condition, the mapping scheme is repeated eight times – right to left (Figure 2.10 (a)), left to right (Figure 2.10 (b)), top to bottom (Figure 2.10 (c)) and bottom to top (Figure 2.10 (d)), with two pairs of nearest neighbors involved each time (Faria and Stoffa, 1994; Kumar et al., 2004). This method of traveltimes mapping is robust. Faria and Stoffa (1994) implement it for TI media and vectorize the algorithm to make it fast. Kumar et al. (2004) uses this algorithm for TTI media and shows this method to be fairly accurate for weak anisotropy.

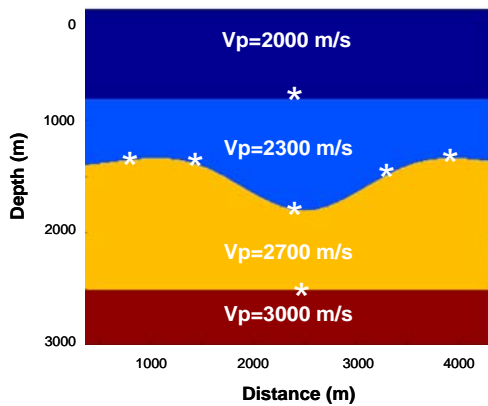


Figure 2.11: Parametrization of heterogeneous velocity model using spline interpolation.

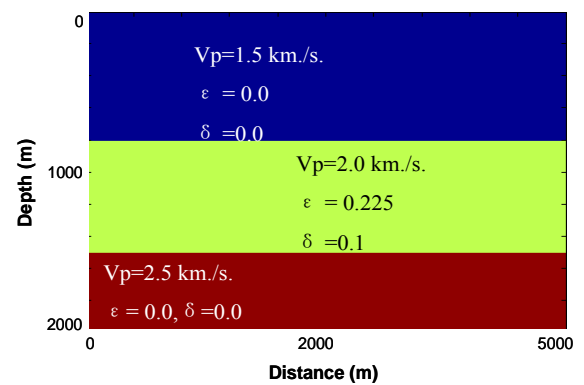


Figure 2.12: Parametrization of VTI model:  $\epsilon$  and  $\delta$  are zero for isotropic layers.



## 2.4 MODEL PARAMETERIZATION AND INVERSION

For the layer-stripping approach to CFP analysis, a model can be thought of to be made up of layers with uniform elastic parameters. For example, Figure 2.11 shows an isotropic heterogeneous model. The parameters that define the model are P-wave velocity and depth. The heterogeneity of the model has been taken into account by defining the interface using interpolation of a set of depth points. For example, the first interface, which is flat, can be defined using only one depth point, (or CFP) and the second interface, which is synclinal, has been generated by spline interpolation of five depth points (or CFPs). The approach to inversion is layer-stripping. Inversion for first layer involves two parameters – P-wave velocity and depth location of one CFP. The second layer involves six parameters – P-wave velocity and depth locations of five CFPs. For a weak VTI medium with a flat interface, a layer can be fully characterized by the three elastic parameters  $\alpha_0$ ,  $\epsilon$ ,  $\delta$  and depth, for example, layer 2 in Figure 2.12. For the Foothills model, the dips of each block of the thrust sheet, minimum P-wave velocity  $\alpha_0$ , and thickness of thrust-sheet have been obtained by isotropic velocity analysis at points A and B in Figure 2.3. I also assume that the thrust sheet is a weak, transversely-isotropic medium (Thomsen, 1986) and that parameters  $\epsilon$  and  $\delta$  are homogeneous within the sheet though the tilt of symmetry axis is varying and is perpendicular to base of thrust sheet.

Thus we need to estimate correct values of  $\epsilon$  and  $\delta$  that result in zero DTSs. I use Newton's method to obtain estimates of parameters. Let  $f_k$  represent the DTSs measured for  $M$  offsets where  $1 \leq k \leq M$ , and let  $m_j$  represent the reference

model for  $N$  anisotropic-parameters where  $1 \leq j \leq N$ . Here, we seek an updated model  $\mathbf{m} + \delta\mathbf{m}$ , where  $\mathbf{m}$  is an initial guess, so that DTSSs  $f_k(\mathbf{m} + \delta\mathbf{m})$  are zero. Expand the desired DTSSs  $f_k(\mathbf{m} + \delta\mathbf{m})$  about the measured DTSSs  $f_k(\mathbf{m})$  to get:

$$f_k(\mathbf{m} + \delta\mathbf{m}) - f_k(\mathbf{m}) = \sum_{j=1}^N \frac{\partial f_k}{\partial m_j} \delta m_j + O_k(\delta\mathbf{m}^2). \quad (2.14)$$

where  $\partial f_k / \partial m_j$  are first differentials of measured  $f_k(\mathbf{m})$  with respect to the model parameter updates. Setting  $G_{kj} = \partial f_k / \partial m_j$ ,  $f_k(\mathbf{m} + \delta\mathbf{m})$  to zero and neglecting terms of order  $\delta\mathbf{m}^2$  and higher, we obtain a set of over-determined linear equations for the variable updates  $\delta\mathbf{m}$  according to

$$\mathbf{G}\delta\mathbf{m} = -\mathbf{f} \quad (2.15)$$

where, the matrix  $\mathbf{G}$  is given as

$$\mathbf{G} = \begin{bmatrix} \frac{\partial f_1}{\partial \varepsilon} & \frac{\partial f_1}{\partial \delta} \\ \frac{\partial f_2}{\partial \varepsilon} & \frac{\partial f_2}{\partial \delta} \\ \vdots & \vdots \\ \frac{\partial f_N}{\partial \varepsilon} & \frac{\partial f_N}{\partial \delta} \end{bmatrix}, \quad (2.16)$$

the model parameter update vector  $\delta\mathbf{m}$  is

$$\delta\mathbf{m} = [\Delta\varepsilon \quad \Delta\delta]^T, \quad (2.17)$$

and the DTS vector  $\mathbf{f}$  is

$$\mathbf{f} = [f_1 \quad f_2 \quad \dots \quad f_N]^T. \quad (2.18)$$

Model update  $\delta \mathbf{m}$  is obtained by solving the over-determined Equation 2.15 in a least-squares sense by minimizing the  $L_2$  norm of objective function  $\|\mathbf{G}\delta \mathbf{m} + \mathbf{f}\|^2$  (see, for example Menke, 1989, page 36) as

$$\delta \mathbf{m} = -(\mathbf{G}^T \mathbf{G})^{-1} \mathbf{G}^T \mathbf{f}. \quad (2.19)$$

To obtain the model update, therefore, we need to compute  $\mathbf{f}$  and  $\mathbf{G}$  at each offset. From the plot of DTS panel (Figure 2.13), DTSs  $\mathbf{f}$  are picked using a graphical interface. Computation of the derivatives of  $\mathbf{f}$  numerically through model parameter perturbation requires calculation of DTS panel and picking for every parameter perturbation. This is an expensive and cumbersome process. To avoid this, I compute the derivatives of  $f_k(\mathbf{m})$  directly from the minimum traveltime  $\mathbf{t}(\mathbf{m})$  from the focus point to surface locations in perturbed media following Kabir (1997). In the neighborhood of solution, the DTSs ( $\mathbf{f}$ ) represent the actual error in two-way traveltime from the focus point to shot-receiver array for the assumed model. Thus the DTSs ( $\mathbf{f}$ ) can be expressed in terms of one way traveltime from focus point to surface locations as

$$\mathbf{f} = 2 \times (\mathbf{t}_{real} - \mathbf{t}(\mathbf{m})), \quad (2.20)$$

where  $\mathbf{t}_{real}$  is the one way traveltime from focus point to shot-receiver array for the real subsurface and  $\mathbf{t}(\mathbf{m})$  is the corresponding traveltime for the assumed model  $\mathbf{m}$ . The derivative of Equation 2.17 can be written as

$$\mathbf{f}' = -2\mathbf{t}'(\mathbf{m}), \quad (2.21)$$

as  $\mathbf{t}_{real}$  is constant.

Thus the partial derivatives of DTSs ( $\mathbf{f}$ ) can be numerically obtained by calculating one way traveltime for the assumed model ( $\mathbf{m}=[\varepsilon \ \delta]^T$ ) and perturbed model ( $\mathbf{m}+d\mathbf{m}=[\varepsilon+d\varepsilon \ \delta+d\delta]^T$ ) and using the following equations

$$\frac{\partial \mathbf{f}}{\partial \varepsilon} \approx -2 \times \frac{\mathbf{t}(\varepsilon + d\varepsilon) - \mathbf{t}(\varepsilon)}{d\varepsilon}, \quad (2.22)$$

and

$$\frac{\partial \mathbf{f}}{\partial \delta} \approx -2 \times \frac{\mathbf{t}(\delta + d\delta) - \mathbf{t}(\delta)}{d\delta}; \quad (2.23)$$

to compute derivatives for  $\varepsilon$  and  $\delta$  respectively.

Hence to compute  $\mathbf{G}$  matrix, I create a gridded model of assumed model parameters, compute the minimum traveltime at shot-receiver locations, perturb each parameter one by one and for each perturbation, create the gridded model, compute the minimum traveltime and use Equation (2.1) to create the  $\mathbf{G}$  matrix. Each time the traveltimes are computed using brute force mapping (Kumar et al., 2004) as explained in section 2.3. Calculating the  $\mathbf{G}$  matrix in this way is much faster and efficient than calculating the DTS panel and subsequent picking for each model parameter perturbation.

However, every time a model update ( $\delta\mathbf{m}$ ) obtained using Equation 2.19 is applied; I compute and pick the DTSs for the new model  $\mathbf{m}$ . This makes the inversion more accurate and robust. The DTSs are true representation of traveltime error only in the close proximity of solution, (for e.g. less than 20% error in model parameters). Iteratively, the model error gets reduced and the DTSs approach true error in traveltime. This ensures that the correct solution is reached when DTSs become zero assuming that a unique solution exists.

## 2.5 PARAMETER ESTIMATION FOR FOOTHILLS MODEL DATA

In the thrust sheet model, we seek anisotropic parameters for the thrust sheet that correctly focuses reflection energy at image point C in Figure 2.3. We start with an assumed velocity model. In this case, the assumed model has isotropic thrust sheet. We compute the minimum one-way traveltime from C to the shot-receiver locations. This traveltime is used to construct a time reversed focusing operator called CFP operator (Figure 2.8(a)). This operator is applied to all shot gathers, resulting in one trace per shot gather, containing the response of the reflection point. The resulting traces when placed within a trace-gather corresponding to its shot position form the CFP gather (Figure 2.8(b)). The CFP gather represents one way time response of the focus point C. Figure 2.6 shows the raypaths corresponding to the wave propagation from C to shot locations. It can be seen that the raypaths correspond to near vertical to near horizontal propagation with respect to TI symmetry axis and is well suited for well-constrained inversion. For a true velocity model, the CFP operator and CFP gather should be identical as both represent wave propagation through same path. The difference of CFP operator and CFP response obtained through cross-correlation is called the differential time shifts (DTS) and it represents the error in our model assumption (Figure 2.13). Our inversion seeks anisotropic parameters that make the DTSs near zero.

In the current velocity analysis, we make several a priori assumptions about the subsurface model as limited offset P-wave reflection data is insufficient for estimating anisotropic parameters and depth simultaneously (Tsvankin and

Thomsen, 1994; Tsvankin and Thomsen, 1995; Sen and Mukherjee, 2003). We use the a priori assumptions to construct the isotropic velocity model as follows.

- i) The top and bottom of the non-dipping thrust sheet block and the bottom reflector with pull up below highly dipping thrust-sheet are easily identified in the zero-offset gather (Figure 2.4). Isotropic velocity analysis at lateral locations A ( $X=2300$  m.) and B (5900 m.) (Figure 2.3) gives the background velocity and depth of the top of the non-dipping thrust sheet block and bottom reflector.
- ii) An assumption that the bottom reflector is flat and coincident with the base of horizontal thrust-sheet block gives us the thickness of thrust-sheet as the difference in depth at locations A and B.
- iii) The vertical two-way travelttime from the base of horizontal thrust-sheet block divided by twice the thickness of thrust-sheet obtained in step (ii) gives the vertical P-wave velocity  $\alpha_0$  of the thrust-sheet.
- iv) A quick constant velocity migration using the background medium's P-wave velocity gives the true spatial location of top of the thrust sheet and hence the dips of the thrust-sheet blocks.
- v) The base of the thrust sheet is reconstructed using the assumption that all thrust sheet blocks have constant thickness. Thus the complete isotropic velocity model is obtained.

However, migration using this isotropic model results in de-focused and mis-positioned image below the highly dipping thrust sheet (Figure 2.5). It is intuitive that the poor image quality results from incorrect elastic parameter estimation for the thrust sheet, or simply negligence of anisotropy in the thrust sheet. For correct imaging we need to obtain the remaining parameters  $\epsilon$  and  $\delta$  for the thrust sheet. The angles of tilt of TI symmetry axis for all blocks are obtained using the assumption that they are orthogonal to bedding. Now we perform velocity analysis in CFP domain to obtain anisotropic parameters that focuses the reflection energy to the correct position of the reflection point C (X=3800 m.) (Figure 2.3), below the highly dipping thrust sheet.

## 2.6 RESULTS

First, we obtain the background velocity of the media by analysis at reflection point A and reflection point B as shown in Figure 2.3. Isotropic velocity analysis at point A gives us a value of 2740 ( $\pm 30$ ) m./s. for P-wave velocity and 1410 ( $\pm 20$ ) m. for depth of top of thrust sheet. Similar analysis at point B gives us a background velocity of 2740 ( $\pm 40$ ) m./s. for P-wave velocity and 1935 ( $\pm 25$ ) m. for depth. Using the reflector depth at A and B, we estimate the thickness of the thrust-sheet to be nearly 535 ( $\pm 50$ ) m. Using the vertical traveltimes from base of thrust sheet at location A, we obtain the parameter  $\alpha_0$  (vertical P-wave velocity) for the thrust sheet as 2917 ( $\pm 32$ ) m./s. We use the knowledge of thickness of thrust sheet and the assumption of constant thickness to create the base of the

thrust sheet in our velocity model. Thus we obtain the isotropic velocity model of subsurface. When we perform migration using this isotropic model, we see that the reflector below highly dipping thrust sheet is mis-positioned and poorly imaged (Figure 2.5). For correct imaging of base reflector we need to obtain the parameters  $\varepsilon$  and  $\delta$  for thrust sheet that focuses reflected energy at correct depth location.

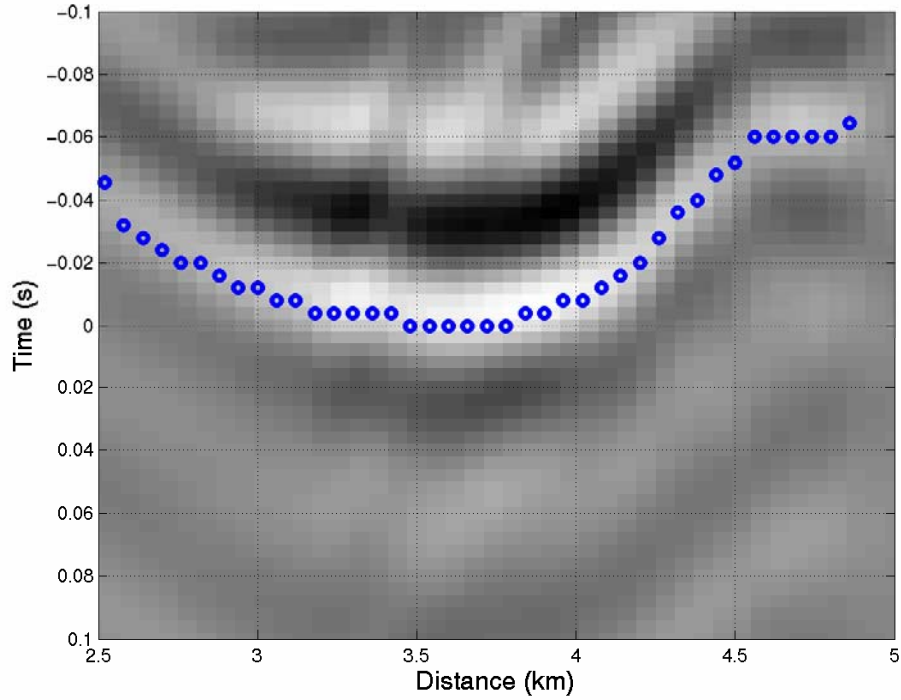


Figure 2.13: DTS panel for point ‘C’ (Figure 1) corresponding to the initial-guess model.

We start with an assumption of isotropic thrust sheet ( $\varepsilon = \delta = 0$ ). The CFP operator in x-t domain is generated by placing the source wavelet at the minimum



traveltime from CFP to each surface location (Figure 2.8a). The operator is applied to each shot gather to obtain a trace containing one-way response of focus point. Together, they constitute CFP response (Figure 2.8b) that represents one-way traveltime from the focus point to the shot location. For an assumed model, the difference in the CFP operator and the CFP response represents the two-way traveltime error, called DTS. We perform trace by trace cross-correlation of the operator and the response to obtain DTS panel (Figure 2.13) and then use a graphical interface to pick the values of DTSs or  $f_k(\mathbf{m})$  to be used in equation (2.15). The partial derivatives of DTSs with respect to model parameters ( $G_{kj} = \partial f_k / \partial m_j$ ) are computed numerically (Kabir, 1997). Then, equation (2.18) is used to obtain model update  $\delta \mathbf{m}$ . After a few iterations, we find that the focusing operator and CFP gather are much more similar (Figure 2.14). This results in a flat DTS panel (Figure 2.15). The migration using the newly obtained anisotropic parameters, given in table 2.1, give a better focused and correctly positioned image of the reflector below the highly dipping thrust sheet (Figure 2.16).

Parameters	Real value	Initial guess	After inversion
$\epsilon$	0.150	0.0	0.156±0.018
$\delta$	0.081	0.0	0.075±0.026

Table 2.1: Result of anisotropic parameter estimation for Foothills model. The true, initial guess and final model parameters obtained after inversion.

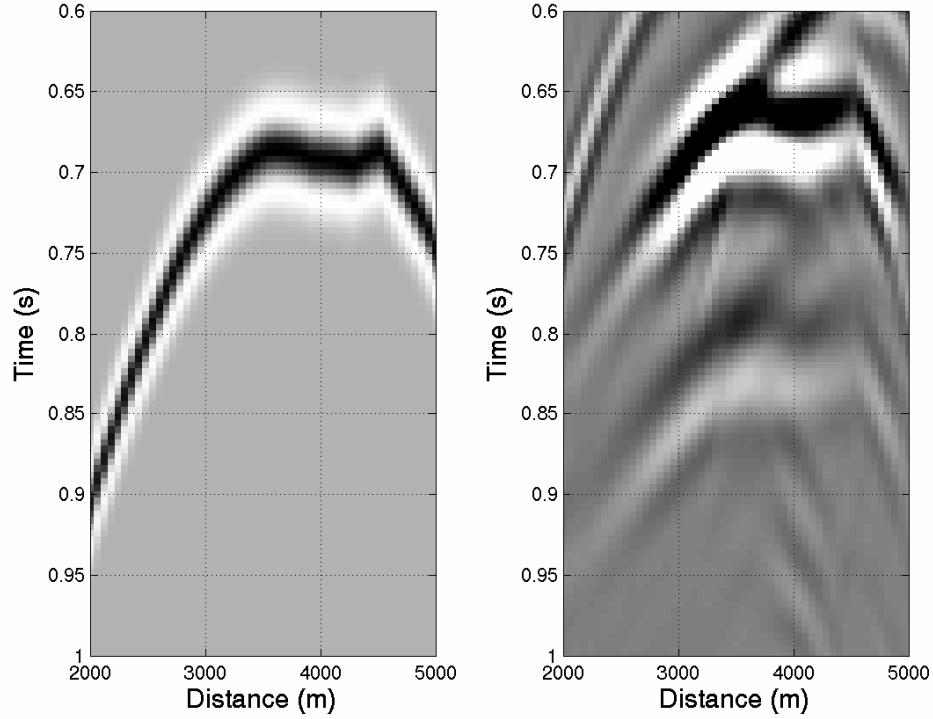


Figure 2.14 (a) CFP operator; (b) CFP response for point ‘C’ (Figure 1), after inversion and model update. Traveltimes to reflectoion peaks are similar, as the model updates are approaching their true values.

This work has some important implications for velocity analysis in regions of complex geology. For example, we may have a TI layer overlain by structurally complex overburden. Here, NMO or DMO based methods will fail, due to the assumption of flat layer or constantly dipping layer. For such media, we can employ layer stripping approach to obtain the velocities of the complex overburden. Having obtained the overburden, we can use the current approach of CFP domain analysis to invert for anisotropic parameters of TI medium. For

unique estimation of anisotropic parameter using only P-wave data, we still need the a priori depth information. In some instances, the depth information can be obtained from well-logs or VSP data or a combination of geology and lateral continuity of structures. In the absence of such information, we need the converted Sv-wave data. The joint inversion of P-wave and converted Sv-wave data will help constrain depth while giving the anisotropic parameters.

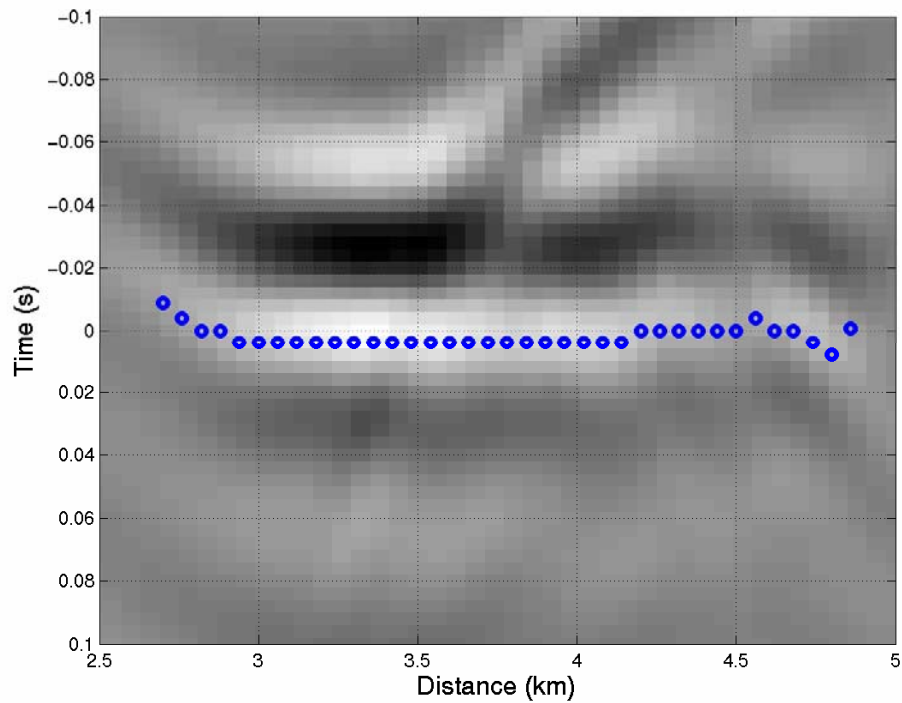


Figure 2.15: The DTS panel after inversion and model update. Traveltime picks align with zero lag to indicate an improved model.

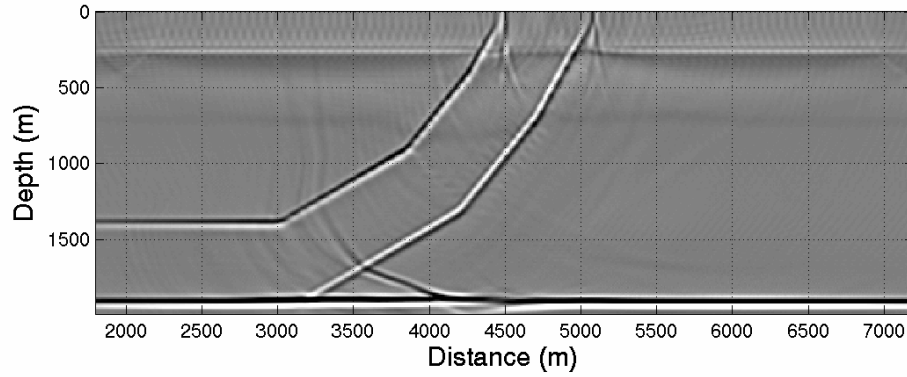


Figure 2.16 : Migrated image using anisotropic velocity model obtained through inversion.

## 2.7 CONCLUSION

The isotropic model based pre-stack migration of the synthetic data of the foothills thrust model produces erroneous image below the thrust sheet. In CFP domain velocity analysis, the error in imaging is seen as non-zero differential time shifts (DTS) between CFP operator and CFP response in the poorly imaged region. An estimate of anisotropic parameters for the thrust sheet  $\epsilon$  and  $\delta$  is obtained using a least square solution of Newton's equation that makes the DTSs zero. The obtained parameter values are very close to the actual parameters. The migration performed after incorporating the newly obtained anisotropic parameters into the model gives a better focused and correctly positioned reflector below the highly dipping thrust sheet.

## Chapter 3: Traveltime Sensitivity Analysis

### 3.1 INTRODUCTION

Time domain velocity analysis in isotropic layered media involves estimating the P-wave normal moveout velocity ( $V_{pNMO}$ ) that fits the short-spread hyperbolic moveout (Dix, 1955). For a weak VTI medium (Thomsen, 1986), short-spread moveout remains hyperbolic (Tsvankin and Thomsen, 1994) and the NMO velocity that fits the hyperbolic moveout is a function of  $\alpha_0$  and  $\delta$ . Because moveout velocity  $V_{pNMO}$  and  $\alpha_0$  are not related directly, inversion of  $V_{pNMO}$  in TI media yields erroneous layer thicknesses and interval velocities, and an irresolvable velocity-depth ambiguity occurs (Tsvankin and Thomsen, 1994). The same observation holds for a layered sequence of weak VTI formations where root-mean-squared (rms) vertical velocity  $V_{pRMS}$  takes the form of  $\alpha_0$ , and average anisotropy takes the place of  $\delta$  (Tsvankin and Thomsen 1995).

For acquisition of very long offset data (offset/depth  $>1$ ), Tsvankin and Thomsen (1994) provide a quartic moveout coefficient to account for nonhyperbolic moveout for P and Sv waves. Their non-hyperbolic P-wave moveout provides two parameters –  $V_{pNMO}$  (a combination of  $\alpha_0$  and  $\delta$ ) and  $\eta$  (a combination of  $\epsilon$  and  $\delta$ ) called anellipticity (Tsvankin and Thomsen, 1994). For depth migration, however, we cannot obtain  $\alpha_0$ ,  $\epsilon$  and  $\delta$  from  $V_{pNMO}$  and  $\eta$ , rather we require long offset P and Sv data to invert jointly for  $\alpha_0$ ,  $\epsilon$  and  $\delta$ . For the long spread Sv wave, however, the quartic moveout coefficient may fail at very large offsets (Tsvankin and Thomsen, 1994).

In this chapter, I perform traveltime sensitivity analysis to investigate the feasibility of estimating elastic parameters, dip, and layer thickness for transversely isotropic subsurface using reflection seismic data. My study separately takes into account the effect of different experimental conditions like offset to depth ratios, availability of multi-component data, and a priori knowledge of subsurface geometry. To study the impact of measurement errors in traveltime data on the estimates of subsurface model parameters I perform sensitivity analysis that includes theoretical uncertainty (prediction error) caused by the physics of the forward problem (Sen and Stoffa, 1995). Knowing these uncertainties, resources of data acquisition can be better applied to give the least erroneous estimates possible if we design acquisition such that prediction error has a very sharp minimum in the vicinity of the estimated solution. The solution will be well determined and precise in the sense that it has small variance. Conversely, where prediction error has a broad minimum, the estimated solution has large variance, and the estimated parameters are highly uncertain.

The variance of an estimator is related to the curvature of prediction error at its minimum through the second derivative of prediction error (Menke, 1989, page 58). When a linear inverse problem is solved in a least square sense, the second derivative of prediction error can be computed directly from the Hessian (Menke, 1989, page 59). In reflection seismology, traveltime is not linearly related to anisotropic parameters. However, in the vicinity of a solution, the problem can be posed as a linear relationship between model parameter update and error in traveltime, e.g., using a generalized Newton's method (Ferguson and

Sen, 2004). Using this linearization, uncertainty in parameter updates, and hence the parameters, can be computed directly from the Hessian, and a limited number of iterations performed until the parameter updates are close to zero (Ferguson and Sen, 2004). For our analysis, we set up the forward problem in the plane wave ( $\tau$ - $p$ ) domain (Stoffa et. al. 1981; Sen and Mukherjee 2003; Ferguson and Sen 2004), where  $\tau$  is intercept time and  $p$  is horizontal slowness. The plane wave domain is advantageous as exact analytical expressions for  $\tau$  exist in terms of  $p$  and the desired anisotropy parameters (Daley and Hron, 1977). Extension to multi-layer problems is straightforward and requires only the algebraic sum of delay times for individual layers.

The results of this analysis are relevant in the context of pre-stack domain parameter estimation using a layer-stripping or downward continuation approach. For example, in common focus point (CFP) technology (Berkhout, 1997), traveltimes error is directly used for parameter estimation. For each subsurface layer, a focusing operator is computed using a model of elastic parameters with which a CFP gather can be constructed using seismic data. Assuming local homogeneity, the resulting differential time shifts (DTSSs) represent error in the model due to anisotropy and error in thickness (Ferguson and Sen 2004). In the ( $\tau$ - $p$ ) domain, the DTSSs are intercept time errors ( $\Delta\tau$ ) that connect error in layer thickness  $z$ , vertical slowness  $q$  and ray parameter  $p$ . The vertical slowness on the other hand is a function of  $p$  and anisotropic parameters.

My analysis shows quantitatively the limitation of P-wave data in resolving anisotropic parameters when depth of reflector is unknown. When the reflector

depth is known, anisotropic parameters can be reasonably constrained for large offset to depth ratio. When the tilt of symmetry axis is known and is large in magnitude, anisotropic parameters as well as depth can be reasonably constrained. The most important outcome of my analysis is that the anisotropic parameters as well as depth can be constrained if we use limited offset P-P (incident P, reflected P) and P-SV (incident P, reflected SV) data jointly. This holds true for joint inversion of P-P and SV-SV data as well, the later being better constrained than the former.

### 3.2 THEORY

Sensitivity analysis makes use of the relationship between the observed attributes  $\mathbf{d}$  (data) and the desirable attributes or parameters  $\mathbf{m}$  (model) (Menke, 1989, page 60). The analytical relationship that maps the model space  $\mathbf{m}$  to the data space  $\mathbf{d}$  is called ‘forward problem’ ( $\mathbf{d}=f(\mathbf{m})$ ). The process of estimating the model parameters  $\mathbf{m}$ , using the observed data  $\mathbf{d}$  is called ‘inversion’. In reflection seismology, the process of inversion is called velocity analysis and it uses the observed time of arrival of reflected energy and source-receiver geometry as observed data ( $\mathbf{d}$ ) to estimate the depth structure of subsurface parameters like velocity of wave propagation ( $\mathbf{m}$ ). For an assumed set of model parameters ( $\mathbf{m}$ ), the estimated arrival time of reflections at different offsets ( $\mathbf{d}^{est}$ ) may not be the same as those in the recorded data ( $\mathbf{d}$ ) due to the presence of noise. Error in trveltime ( $\mathbf{e}$ ) is a vector of the discrepancy between estimated and recorded traveltimes at different offsets ( $\mathbf{d}-\mathbf{d}^{est}$ ). Since seismic data is often contaminated



with noise, the parameter estimator needs to be robust. Estimator robustness is the ability of the estimator to be relatively uninfluenced by errors in a small portion of the data set. Sensitivity analysis tries to quantify the robustness of parameter estimation. Quantification of estimator robustness uses perturbation analysis to assess the effects of variability on estimates. One popular approach is sums of errors method. If we have an analytic forward problem, we can calculate the sensitivities based on the following relation

$$\mathbf{e} = \sum \frac{\partial \tau}{\partial m_i} \Delta m_i \quad (3.1)$$

This expression comes from the truncated Taylor series expansion about the true data values and may be useful only in the vicinity of the solution (less than 20% or so)  $\mathbf{m}$ . It is important to analyze how an error in a parameter reflects itself as error in collected data. Figure (3.1) shows the error in P-wave traveltimes for Cretaceous Mesaverde clayshale at different offset to depth ratio for approximately 10% error in the anisotropic parameters. Here, for example, the traveltimes error resulting from error in parameter  $\delta$  is very small even at very large offset to depth ratio of 2. If the picking has an uncertainty of the order of 4 ms, we cannot invert for this parameters with great confidence. Figure (3.2) shows the error in Sv-wave traveltimes for Mesaverde clayshale. We can see that at offset to depth ratio of approximately 1, the traveltimes error due to error in  $\delta$  is of the order of 10 ms. So, if we have less noisy data, we may hope to invert  $\delta$  by using P and Sv data jointly.

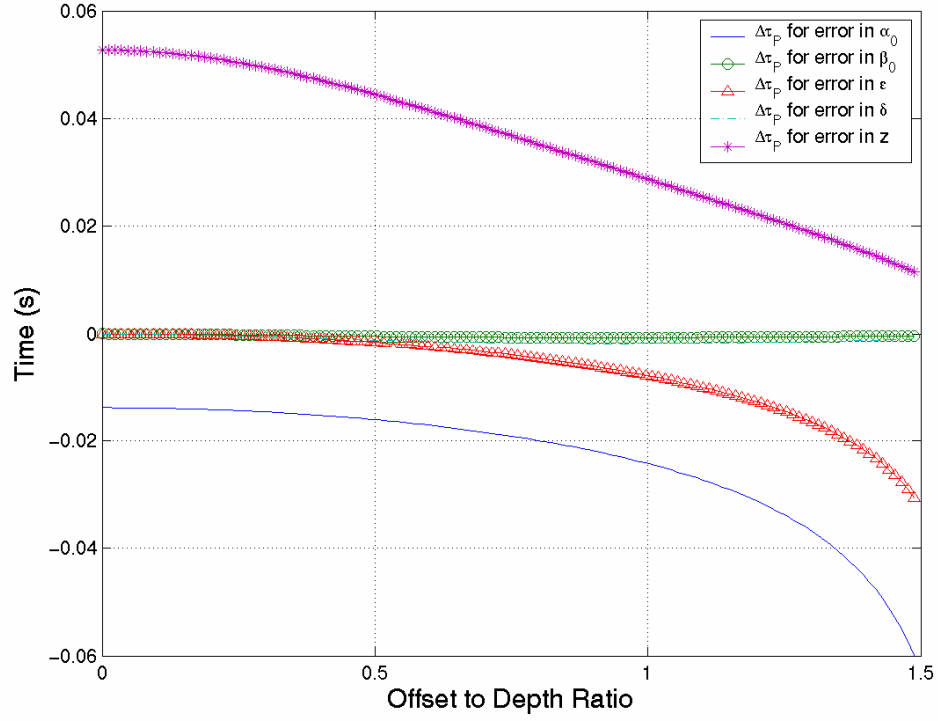


Figure 3.1. Plot of offset to depth ratio versus error in vertical traveltime ( $\Delta\tau$ ) for P-arrival resulting from approximately 10% error in the model parameters  $[\alpha_0, \beta_0, \epsilon, \delta, z]$ .

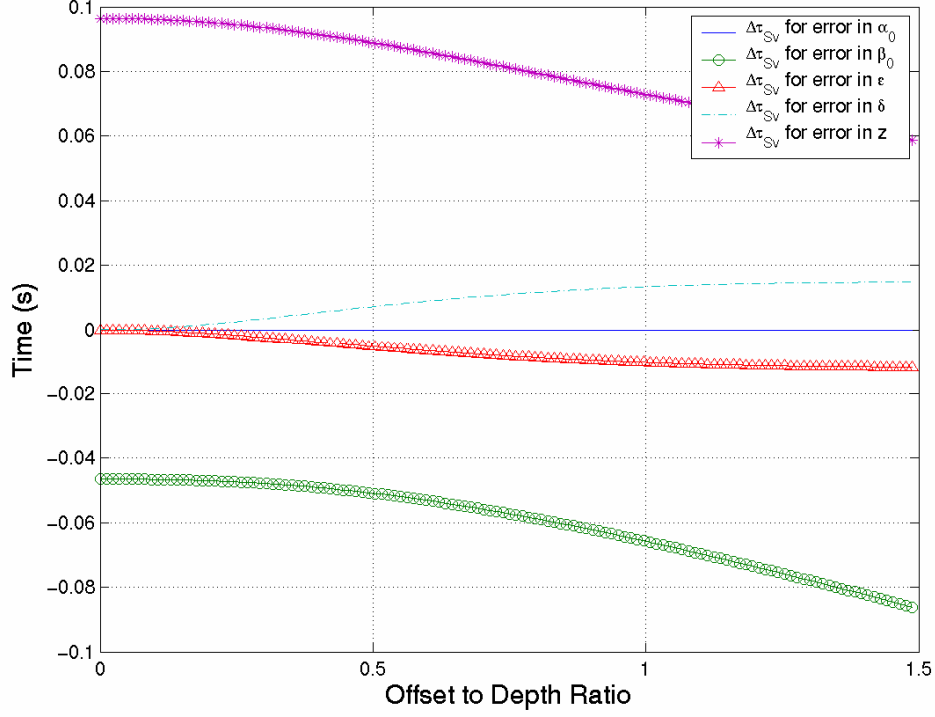


Figure 3.2. Plot of offset to depth ratio versus error in vertical traveltime ( $\Delta\tau$ ) for Sv-arrival resulting from approximately 10% error in the model parameters  $[\alpha_0, \beta_0, \epsilon, \delta, z]$ .

Prediction error for the model  $\mathbf{m}$  is defined as  $E(\mathbf{m}^{est}) = \mathbf{e}^T \mathbf{e}$  and is a scalar.

The nature of prediction error is useful in predicting the effect of noise in data ( $\mathbf{d}$ ) to the accuracy or confidence in estimated parameters ( $\mathbf{m}^{est}$ ). Figure 3.3 shows a plot of traveltime prediction error against estimated P-wave velocity for a flat reflector in a homogeneous isotropic medium when (i) depth is fixed, and (ii) when depth is allowed to vary within a certain range. In the later case, the value of minimum traveltime error within the given depth range is plotted. We can see that

for a predication error of  $0.005 \text{ sec.}^2$ , the error in estimated P-wave velocity for case (i) is 150 m/s., and that for case (ii) is only 60 m/s. indicating that the solution is well-determined for case (ii) as compared to case (i). This over-determined problem has a sharp minimum in the vicinity of estimated parameter (P-wave velocity) for case (i) indicating that the solution is well-determined in the sense that it has small variance. For case (ii)  $E(\mathbf{m})$  has a broad minimum indicating large variance of the estimated parameter and hence poorly determined solution (Menke, 1989). The curvature of the error function is a measure of the sharpness of its minimum and the variance of the solution is related to the curvature. Hence, an estimate of how well a solution is constrained can be obtained from the curvature of prediction error. In the vicinity of solution, the curvature of the prediction error can be measured by its second derivative.

In the plane wave domain, expressions for vertical slowness for quasi P-waves ( $q_p$ ) and quasi SV-waves ( $q_{sv}$ ) in terms of Thomsen's parameters are given by,

$$q_p = \frac{1}{2} \sqrt{2\beta_0^{-2} + 2\alpha_0^{-2} - 4Sp^2 - 4R} \quad , \quad (3.2)$$

and

$$q_{sv} = \frac{1}{2} \sqrt{2\beta_0^{-2} + 2\alpha_0^{-2} - 4Sp^2 + 4R} \quad , \quad (3.3)$$

where,

$$S = \frac{1}{2} \frac{\alpha_0^2}{\beta_0^2} [\varepsilon - \delta^*] + \frac{1}{2} \varepsilon + 1, \quad (3.4)$$

and

$$R = \frac{1}{2} \sqrt{4p^4 [S^2 - 2\varepsilon - 1] + 4 \left( \frac{p}{\beta_0} \right)^2 [2\varepsilon - S + 1] + 4 \left( \frac{p}{\alpha_0} \right)^2 [1 - S] + (\beta_0^{-2} - \alpha_0^{-2})^2} \quad . \quad (3.5)$$

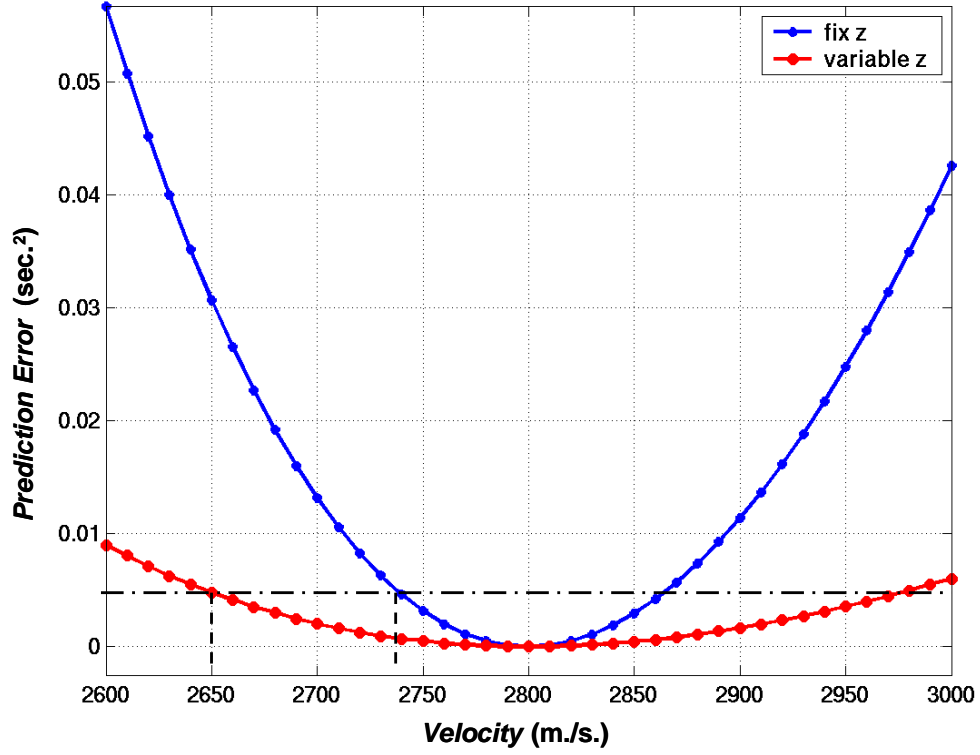


Figure 3.3. Plot of  $V_p$  versus error for fixed  $z$  and variable  $z$ . For fixed  $z$ , error has a sharp curvature at the minimum compared to that for variable  $z$ .

Vertical traveltime ( $\tau_p$ ) for P-wave (incident P, reflected P) is given by,

$$\tau_p = 2zq_p \quad , \quad (3.6)$$

and vertical traveltime ( $\tau_{sv}$ ) for Sv-wave (incident Sv, reflected Sv) is given by,

$$\tau_{sv} = 2zq_{sv} \quad . \quad (3.7)$$

For a converted P-SV-wave, vertical traveltime ( $\tau_{p-sv}$ ) (incident P, reflected Sv) is given by,

$$\tau_{p-sv} = z(q_p + q_{sv}) \quad . \quad (3.8)$$

Exact analytical expressions for partial derivatives of vertical traveltimes with respect to the model parameters exist, using equations 3.6, 3.7, 3.8 and equations 3.2 and 3.3, for use in a generalized Newton's equation (2.15) to obtain model updates  $\Delta \mathbf{m}$ . Error ( $E$ ) for an estimated model parameter is given by

$$E = \Delta \mathbf{t}' \Delta \mathbf{t}, \quad (3.9)$$

where ' indicates transpose.

Without assuming weak TI, the model space for VTI medium is given by  $\mathbf{m} = [\alpha, \beta, \varepsilon, \delta, z]$ , and for tilted TI medium is  $\mathbf{m} = [\alpha, \beta, \varepsilon, \delta, z, \theta]$ , where  $\theta$  is tilt angle of symmetry axis with respect to vertical.

As mentioned before, the curvature of prediction error depends can be measured by its second partial derivative. For the model parameter vector  $\mathbf{m}$ , the matrix containing the second partial derivatives of prediction error is called sensitivity matrix ( $\mathbf{S}$ ), and is given by

$$\mathbf{S} = \frac{\partial^2 E}{\partial m_i \partial m_j} \quad (3.10)$$

where the  $i, j$  partial derivatives are with respect to the  $i$  and  $j$  model parameter  $\mathbf{m}$ .

It can be shown that  $\mathbf{S}$  (Equation 3.11) is approximately equal to twice  $\mathbf{G}^T \mathbf{G}$  and the covariance matrix is given by (Menke, 1989),

$$[Cov(\mathbf{m})] = \sigma^2 [\mathbf{G}^T \mathbf{G}]^{-1} = \sigma^2 \left[ \frac{1}{2} \mathbf{S} \right]^{-1} \quad (3.11)$$

where,  $\sigma$  is the standard deviation of data.

The uncertainty associated with the model parameter  $m_i$  is related to square root of  $i^{\text{th}}$  diagonal element of covariance matrix. In this way, the curvature of error surface is mapped to the uncertainty in model parameter estimate.

### 3.3 SENSITIVITY ANALYSIS

In this section, I show the results of performing sensitivity analysis for Mesaverde clayshale (Thomsen, 1986), whose anisotropic parameters are  $\alpha_0=3794$  m/s,  $\beta_0=2074$  m/s,  $\varepsilon=0.189$ , and  $\delta=0.204$ . Though, I show my results for a particular rock type, a similar analysis can be performed for any transversely isotropic rock.

#### 3.3.1 SENSITIVITY ANALYSIS FOR VTI MEDIA

Table 3.1 lists the uncertainty in the estimates of the anisotropic parameters for different types of data. The only cases when anisotropic parameters can be estimated with a reasonably small uncertainty are P-P data with known depth, joint P-P and P-Sv data, and joint P-P and Sv-Sv data. It can be seen that for all these three cases, uncertainty in estimates decreases with an increase in offset to depth ratio (Figure 3.2, 3.3 and 3.4). The joint inversion of either P-P and Sv-Sv data or P-P and P-Sv data provides improved estimates of model parameters even when depth is not known.

#### 3.3.2 SENSITIVITY ANALYSIS FOR TTI MEDIA

A similar analysis has been performed for tilted TI medium when angle of tilt of symmetry axis is known, say from geology of overlying formations. It can be seen (Table 3.2) that using only P-wave data it is feasible to estimate  $\alpha_0$ ,  $\varepsilon$ ,  $\delta^*$  and  $z$  if the tilt angle is known and is large in magnitude. For a near zero tilt of symmetry axis, the uncertainty in the estimation of anisotropic parameters  $\alpha_0$ ,  $\varepsilon$ ,  $\delta^*$  and  $z$  for limited offset involves very high uncertainty. We may have a TI medium, in which the angle of tilt of symmetry axis of the medium is laterally

variable. In such a case, if the angle of tilt is known at more than one location, a joint inversion of P-wave data from these locations coupled with the knowledge of tilt angles constrain the elastic parameters well (Table 3.2).

Data Type	%age uncertainty in elastic parameters				
	$\alpha_0$	$\beta_0$	$\epsilon$	$\delta^*$	$z$
PP (fix $z$ , weak TI)	0.12	-	16.54	34.6	-
PP (fix $z$ , strong TI)	0.15	$9.3 \times 10^3$	103	7961	-
PP (var $z$ , weak TI)	2431	$1.8 \times 10^4$	$1.4 \times 10^4$	2431	-
PP (var $z$ ), strong TI)	$4.3 \times 10^5$	$1.2 \times 10^6$	$3.1 \times 10^6$	$3.4 \times 10^6$	$4.3 \times 10^5$
PSv (var $z$ , strong TI)	$4.9 \times 10^4$	$1.1 \times 10^4$	$3.5 \times 10^5$	$5.5 \times 10^5$	$1.0 \times 10^4$
PP-SvSv (var $z$ , strong TI)	1.39	1.42	12.5	5.3	1.4
PP-PSv (var $z$ , strong TI)	10.3	10.3	85.5	47.1	10.3

Table 3.1. Uncertainty in elastic parameter estimates for different types of data as calculated analytically. Maximum offset to depth ratio is 1.5 and standard deviation is 4 ms.



Tilt angles	Uncertainty Estimates (%age)			
	$\alpha_0$	$\varepsilon$	$\delta^*$	$z$
$1^0$	1631	1010	7875	1380
$10^0$	41	265	212	33
$20^0$	13.5	94	247	8.8
$30^0$	1	11	42	1
$40^0$	1.7	15.7	31	1.18
$0^0, 10^0$	4	25	24	3.3
$0^0, 20^0$	1	7	11	0.8
$0^0, 10^0, 20^0$	1	7	11	0.8
$0^0, 30^0, 50^0$	.1	0.9	6.3	0.15

Table 3.2. Uncertainty in elastic parameter estimates for different tilt angles for a TTI medium using P-wave data only when tilt angle of the TI medium is known.

When tilt angle of the TI medium is not known, a joint inversion of PP and SvSv data may be used to estimate all the parameters, i.e.  $\alpha_0, \beta_0, \varepsilon, \delta^*, \theta$  (tilt angle), and  $z$  (depth) simultaneously. However, this approach will yield fruitful result only when the TI medium has a reasonable tilt. For a near VTI medium, this approach will result in high uncertainty for certain parameters, when tilt angle is also a model parameter (Table 3.3).

Table 3.3 shows that uncertainty of parameters decreases with increase in angle of tilt of the symmetry axis. This observation is attributed to the fact that

with an increase in tilt angle, the slowness curve becomes more asymmetric (Figure 3.5). Thus for the same range of ray parameter values, the effects of much larger incidence angles are incorporated. The assumption here is that the layer interfaces are flat even though the symmetry axis of transverse isotropy is not vertical.

Tilt Angle	Uncertainty in %age for					
	$\alpha_0$	$\beta_0$	$\epsilon$	$\delta^*$	Tilt angle	Z
$1^0$	27	56	195	107	1431	26
$10^0$	2	1	24	32	140	1
$20^0$	2	5	28	77	19	2
$30^0$	2	.3	30	25	10	.7
$40^0$	1	.4	19	12	.2	.6
$50^0$	1	.4	16	12	.2	.6
$60^0$	.6	.3	12	7	.1	.9

Table 3.3: Uncertainty in elastic parameter estimates for different tilt angles for Joint Inversion of PP and SvSv data for offset to depth ratio of 1 and standard deviation of 4 ms. The angle of tilt of TI medium is also a model parameter.

### 3.4 SUMMARY

Sensitivity analysis presented here helps us in quantifying the limitations of resolving anisotropic parameters for a VTI media. This paper assesses the feasibility of Joint inversion of P-P and Sv-Sv data and P-P and P-Sv data in

estimating anisotropic parameters as well as depth. Though P-P data or P-Sv data alone do not provide unique estimates of anisotropic parameters and depth, the Joint inversion provide highly resolved estimates. For tilted TI medium overlying a flat reflector, Joint inversion of P-P and Sv-Sv data, however, may help estimating depth, anisotropic parameters, and tilt angle as well.

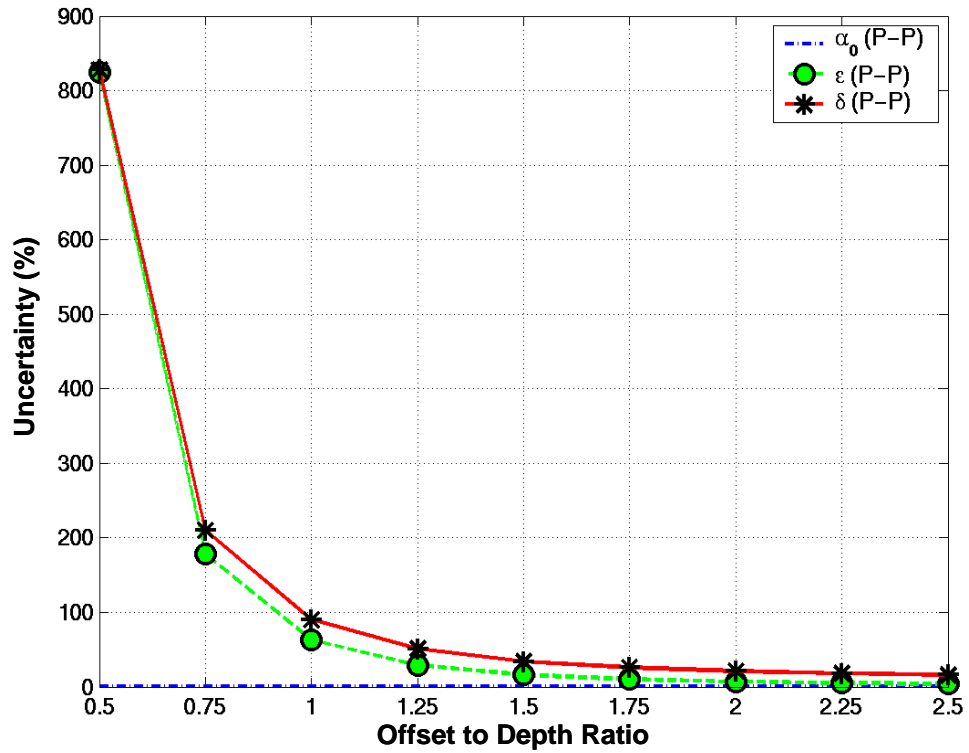


Figure 3.4: Plot of parameter uncertainty versus offset to depth ratio for P-P data, when depth is known. As the offset to depth ratio increases, parameter uncertainty for  $\epsilon$  and  $\delta$  decreases, while uncertainty for  $\alpha_0$  remains low and nearly constant.

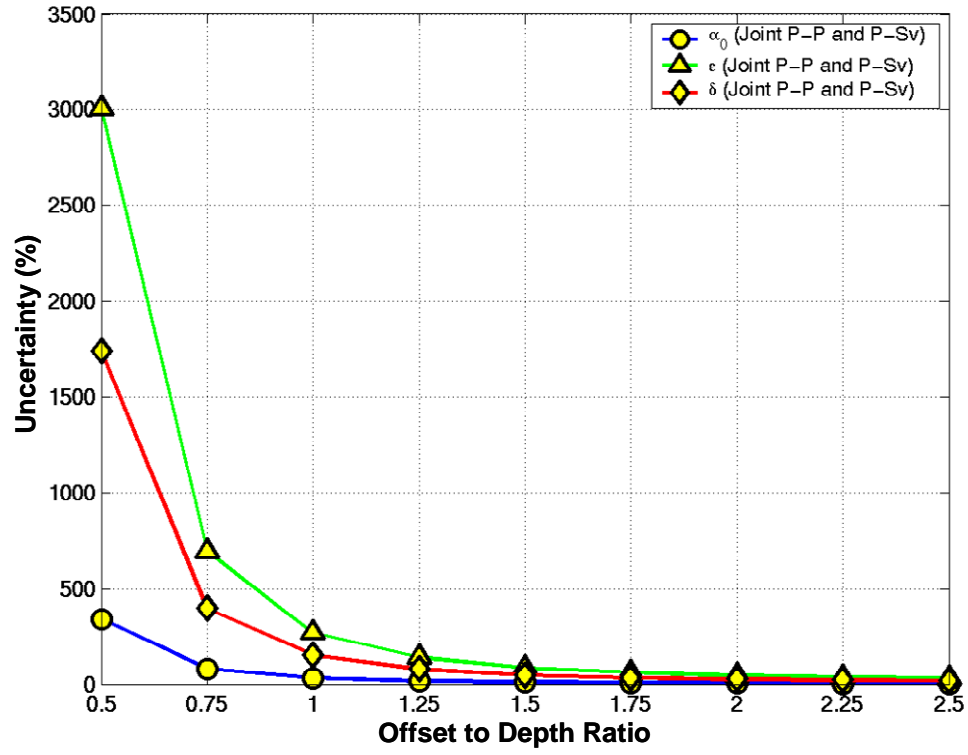


Figure 3.5: Plot of parameter uncertainty versus offset to depth ratio for joint inversion of P-P and P-Sv data. As the offset to depth ratio increases, parameter uncertainty decreases.

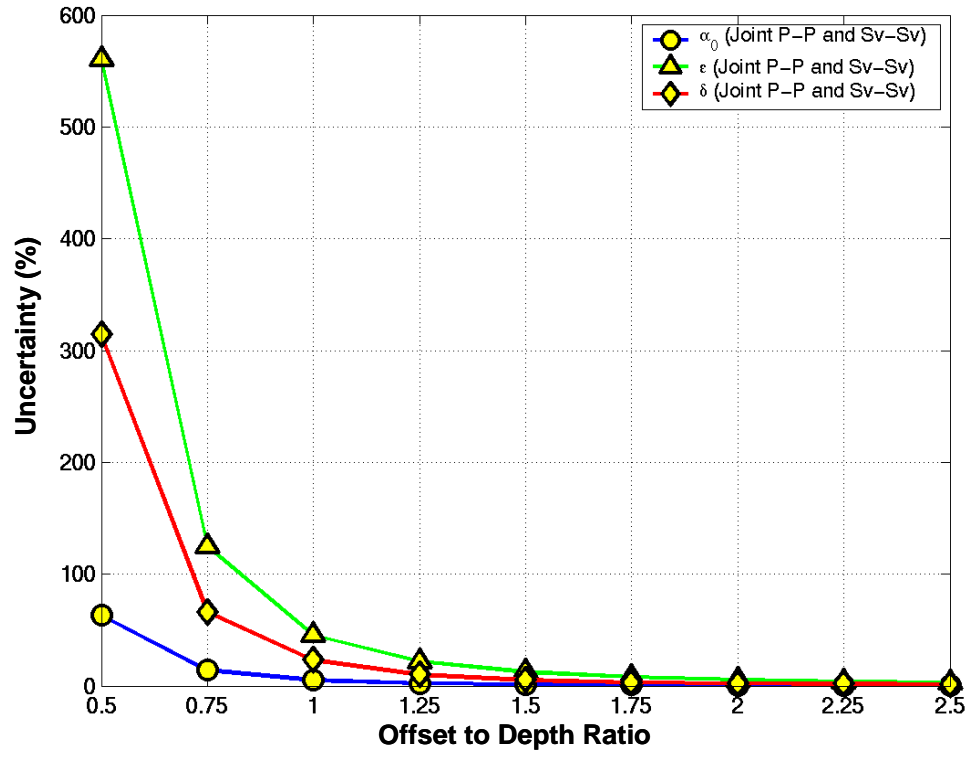


Figure 3.6: Plot of parameter uncertainty versus offset to depth ratio for joint inversion of P-P and Sv-Sv data. As the offset to depth ratio increases, parameter uncertainty decreases.

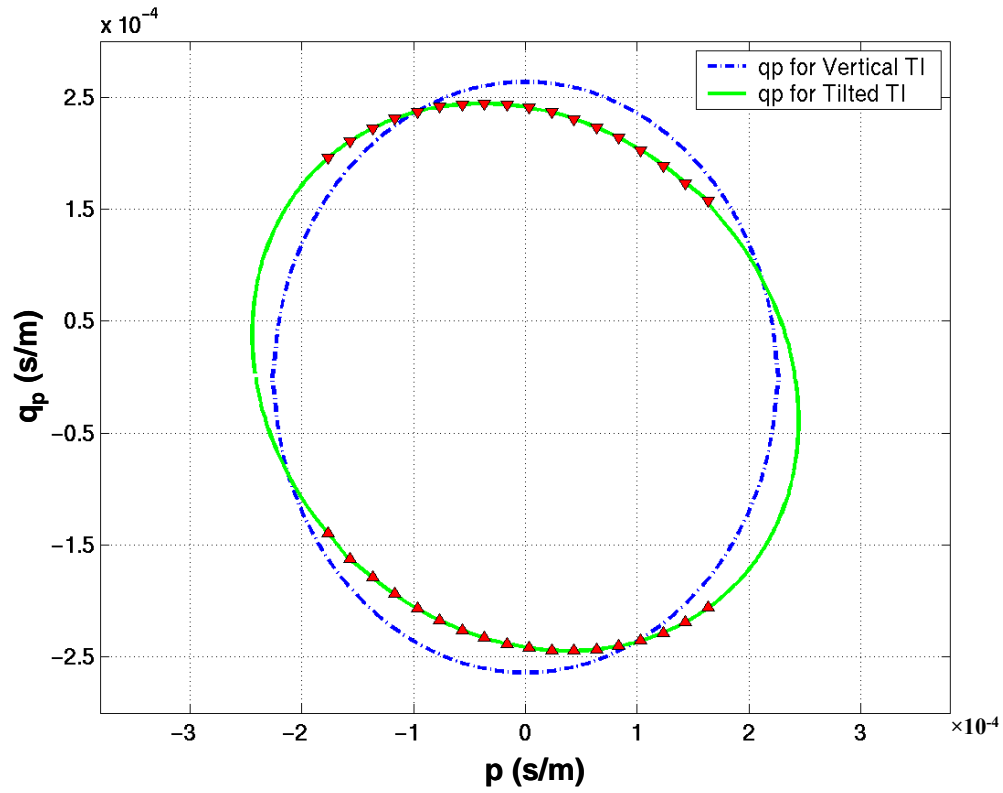


Figure 3.7. Slowness curves for Mesaverde clayshale. The dotted blue line is slowness curve when symmetry axis is vertical. The continuous green line is slowness curve when symmetry axis is tilted by  $45^\circ$  w.r.t. vertical. The '▽'s are slownesses for downgoing waves and 'Δ's for upgoing waves corresponding to a certain range of ray parameters.

## **Chapter 4: Joint Inversion of P-P and P-Sv Data**

### **4.1 INTRODUCTION**

Acquisition of multicomponent seismic data has received considerable attention (Tatham and McCormack, 1991; Hoffe et al., 2000; Stewart et al., 2002, 2003). Though it is possible to record all nine components (P-P, P-Sv, P-Sh, Sv-P, Sv-Sv, Sv-Sh, Sh-P, Sh-Sv and Sh-Sh), pure mode Sv-Sv data are rare. The use of mode-converted P-Sv data has gained popularity with the advent of Ocean Bottom Cable (OBC) technology and Vertical Seismic Profiling (VSPs) technology (Barr, 1997; Granli et al., 1999; Jin et al., 2000; Yuan, 2001). Converted waves provide significant advantages for imaging in certain cases: examples are imaging through gas clouds (Granli et al., 1999; Li et al., 2001), imaging low P-wave contrasts (Engelmark, 2000), imaging below high velocity complex salt structures (Purnell, 1992), imaging fractures (Ata and Michelena, 1995) and imaging 3D channels (Margrave et al., 1998) and seismic characterization of reservoirs (Graotta et al., 1985; Blott et al., 1999; Li et al., 1999).

The mode converted data P-S data have several advantages over direct S-S data. Generally the images generated from converted P-S data often have resolution and signal to noise advantages over those from pure mode S-S data (Tatham and Goolsbee, 1984). In addition to difficulties with generating shear waves directly, shear source operation is relatively complicated, since recording of two perpendicularly polarized emissions are required for each source location

(Garotta, 2002). P-wave sources require only 3-component geophones to record both P-P and P-S data, with perhaps some adjustment to recording time. Also S-S data have longer recording time than P-S data. In terms of processing, S-S reflection data need a solution for relatively large shot and receiver statics while P-S data benefit from previously determined P-wave source statics (Garotta et al., 2002). The frequency content of the S-S data is often lower than P-S data, and hence S-S data are sometimes contaminated by low frequency, source generated noise (Garotta et al., 2002).

Conventionally, velocity analysis for P-wave reflection seismic data uses CMP sorting and estimating a suitable moveout velocity (Dix, 1955). For P-S data it is necessary to account for the asymmetrical travel path of converted waves. A straightforward albeit approximate method of converted wave analysis is to map the data into CCP (common conversion point) bins. The CCP sorting is based on finding conversion points based on assumptions made on the  $V_p/V_s$  ratio (Tessmer et al., 1990; van der Baan, 2005) and is successful only for low relief data. For example, CCP binning and P-S DMO are only partial solutions to the asymmetry problem and face some difficulty with structural data. However, depth migration requires accurate determination of the P-wave and S-wave velocity models (Schneider, 2002) in order to ensure consistency between depths estimated for the PP and PS reflection events.

Pre-stack velocity analysis in CFP domain avoids the need to compute the conversion point location (Berkhout and Verschuur, 2000). Since CFP method is based on separate focusing of seismic data at the source and receiver sides, the



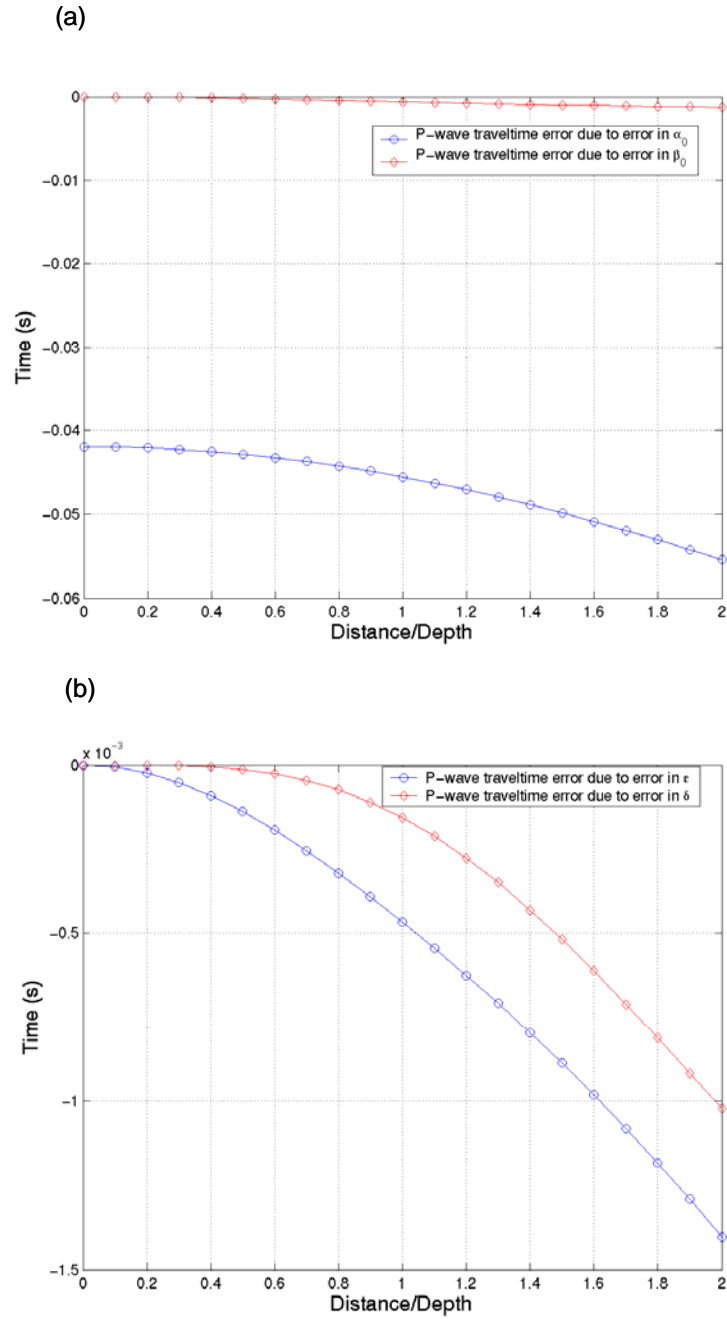


Figure 4.1: Plot of offset to depth ratio versus error in traveltimes for P-P waves for 20% error in parameters (a)  $\alpha_0$ ,  $\beta_0$  and (b)  $\epsilon$ ,  $\delta$ . The rock parameters of Mesaverde shale (Thomsen, 1986) used.

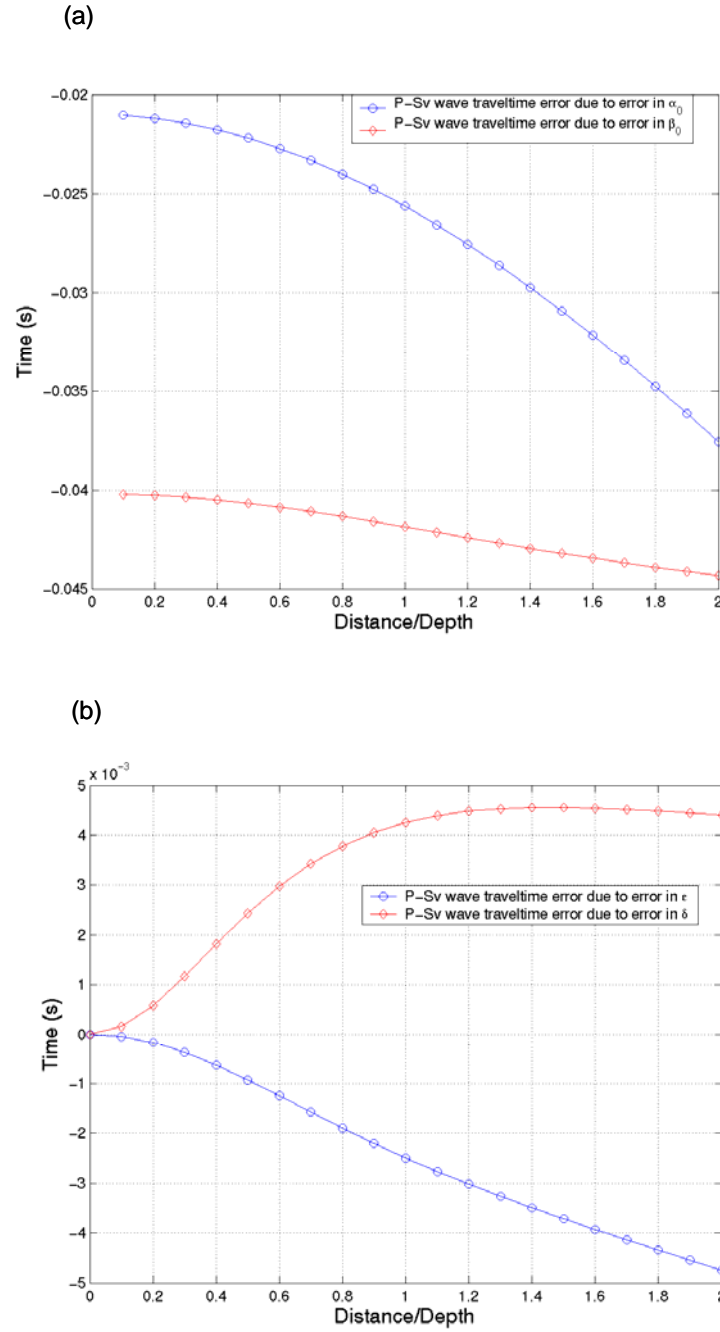


Figure 4.2: Plot of offset to depth ratio versus error in traveltimes for P-Sv waves for 20% error in parameters (a)  $\alpha_0$ ,  $\beta_0$  and (b)  $\epsilon$ ,  $\delta$ . The rock parameters of Mesaverde shale (Thomsen, 1986) used.

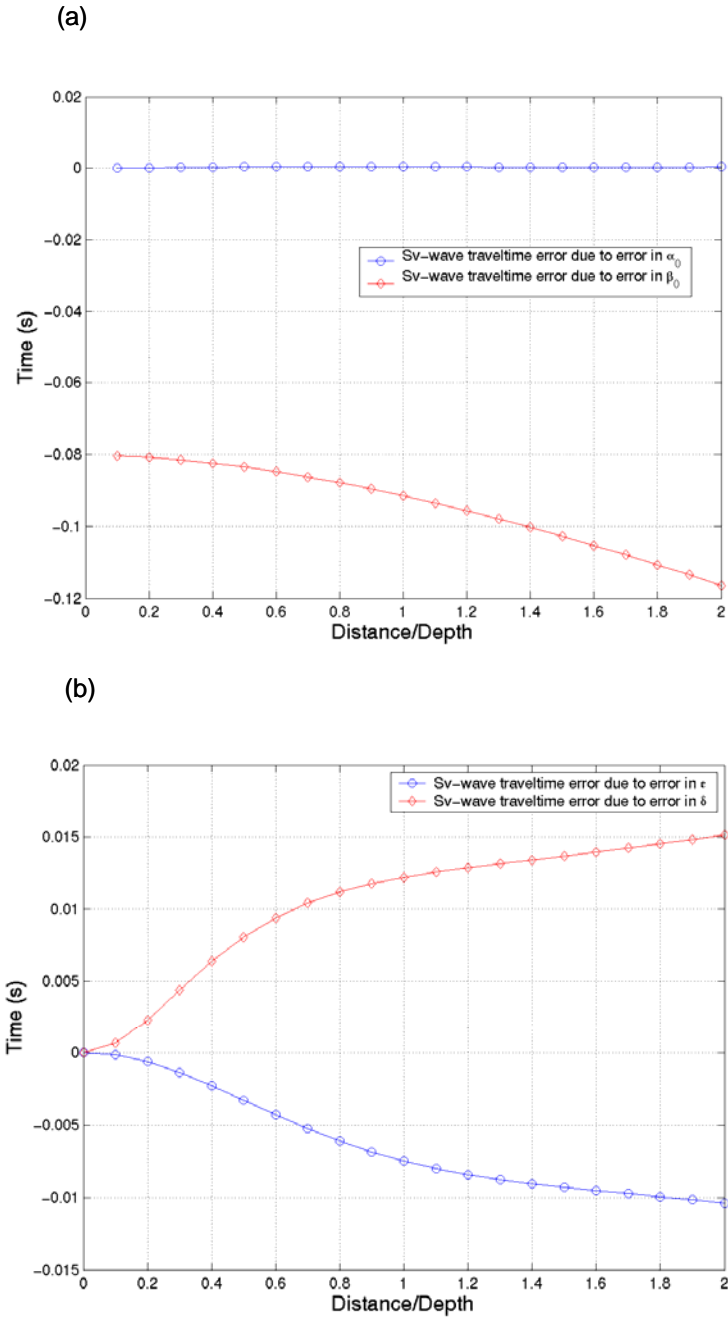


Figure 4.3: Plot of offset to depth ratio versus error in traveltimes for Sv-Sv waves for 20% error in parameters (a)  $\alpha_0$ ,  $\beta_0$  and (b)  $\epsilon$ ,  $\delta$ . The rock parameters of Mesaverde shale (Thomsen, 1986) used.

operator for focusing in detection may address another wave type than the operator for focusing in emission (Berkhout, 1997).

Velocity analysis for TI media using P-wave traveltime fails to yield unique anisotropy parameter estimates due to velocity-depth ambiguity (Faria, 1993; Tsvankin and Thomsen, 1994; Tsvankin and Thomsen, 1995). Thus, to obtain well-constrained anisotropic parameters using P-wave reflection data, we need to have *a priori* knowledge of the reflector depth, either from well-logs or from a VSP experiment. Compared to P-wave, S-wave is more sensitive to anisotropy and offset, therefore, better suited for estimation of anisotropic parameters. Since pure mode Sv data are rare, mode converted P-Sv data can be used together with P-P data to obtain constraints on anisotropy parameters (Faria, 1993).

The effect of perturbing anisotropic parameters by 20% on the recorded arrival time of P-P wave, P-Sv wave and Sv-Sv wave are shown in Figures 4.1 and 4.2 and 4.3 respectively for a 500 m thick VTI medium. It can be seen that compared to P-wave, Sv wave arrivals are far more sensitive to error in  $\epsilon$  and  $\delta$  and hence anisotropy is more detectable in Sv waves. However, the Sv-wave arrivals are almost insensitive to parameter  $\alpha_0$ , whereas P-wave arrivals are almost insensitive to parameter  $\beta_0$ . Hence, in order to obtain a constrained estimate of all five TI anisotropy parameters, we need both P-wave and Sv-wave traveltimes. In Chapter 3, I have established quantitatively that joint inversion of P-wave and S-wave data result in better constrained elastic parameter and depth estimation for a TI medium. Though joint inversion of (i) P-P and Sv-Sv and (ii) P-P and P-Sv are both suitable for estimating TI anisotropy parameters, joint P-P and Sv-Sv

inversion is better constrained than joint P-P and P-Sv inversion for the same recording aperture. This can also be understood from Figure 4.1 and Figure 4.2. For the same offset to depth ratio, the error in Sv-Sv traveltimes is larger than that of P-Sv traveltimes, which in turn is larger than P-P traveltimes. However, converted P-Sv data are more commonly available than pure Sv-Sv data.

For my study I use the geology of Blackfoot field located near Strathmore in southeastern Alberta. Figure 4.4 shows a vertical cross-section of Blackfoot field. The exploration target is Glauconitic incised valleys in Lower Manville group of lower Cretaceous channel system with three phases of valley incision. The lower and upper members are porous while the middle one is relatively denser lithic sandstone (Miller et al., 1995). In the Blackfoot field, the channel system is 40 m thick and 100 m wide and located at a depth of approximately 1700m. All three phases of channel are not present everywhere. The upper channel is gas-prone whereas the lower channel is oil-prone.

The geology of Blackfoot is interesting for joint P-P and P-Sv analysis for mainly two reasons – (i) gas is often associated with porous sandstone channel which is imaged better using migration of P-S data than pure mode P-P data, and (ii) the channel being overlain by anisotropic formations, the depth estimation will be incorrect without taking into account anisotropy. Thus it makes for a suitable case to test improvement in anisotropy estimation using joint inversion of P-P and P-Sv data.

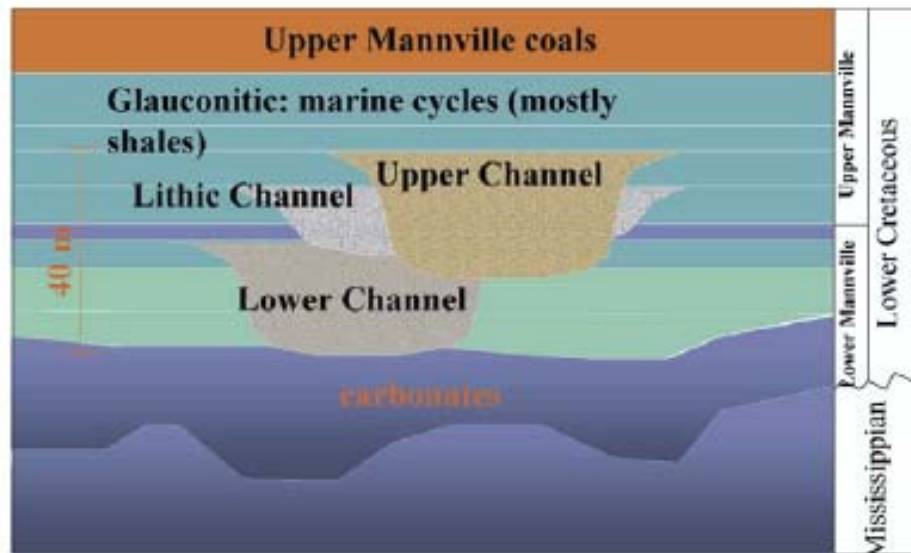


Figure 4.4: The glauconite channel system at Blackfoot oil field, Alberta, is a sequence of sand and shale filled valleys incised into Lower Cretaceous and Mississippian carbonates. The Blackfoot interpretation has an upper and lower channel that are prospective and separated by a non-porous lithic channel fill (from Margrave et al., 2001).

I choose to perform joint inversion in plane wave or delay time-phase slowness ( $\tau$ - $p$ ) domain as it offers several advantages over  $x$ - $t$  domain inversion (baan and Kendall, 2002; Ferguson and Sen, 2004; Sen and Mukherjee, 2004). The  $\tau$ - $p$  curves depend on phase velocities and are simpler to compute compared to ray tracing based  $x$ - $t$  curves that require group velocity (baan and Kendall, 2002). However, phase velocities need to be expressed in terms of horizontal slownesses either using analytical expression or by solving Christoffel equation (baan and Kendall, 2002). For TI anisotropy, exact analytical expressions for

phase velocity in terms of horizontal slowness exist (baan and Kendall, 2002; Ferguson and Sen, 2004). The  $\tau$ - $p$  curve for laterally homogeneous stratified media are exact and is able to handle kinks and cusps in Sv traveltimes (baan and Kendall, 2002). Also layer stripping in  $\tau$ - $p$  domain is linear process and hence both effective (average) and local (interval) estimates can be made (baan and Kendall, 2002; Ferguson and Sen, 2004; Sen and Mukherjee, 2004).

In this chapter, first I perform analytic joint inversion of P-wave and Sv-wave response for different anisotropic layers in Blackfoot model under different noise conditions. The analytic study suggests that joint inversion of limited aperture and limited bandwidth data involving thin layers is highly sensitive to noise and is unstable even under moderate noise conditions. Hence, I build an anisotropic model with the same geology, but with amplified layer thicknesses. I generate synthetic data for this model using staggered grid finite differencing 4<sup>th</sup> order in space and 2<sup>nd</sup> order in time. For this data, I perform joint inversion in plane wave domain. The joint inversion for this model gives good estimate of depth and anisotropic parameters.

## 4.2 THEORY

The CFP domain analysis is especially suitable to converted wave analysis as separate focusing at receiver side and source side allows addressing one wave type at a time. For example, for P-Sv data, receiver side focusing (*focusing in detection*) addresses Sv-wave propagation from focus point (CFP) to receiver array whereas source side focusing (*focusing in emission*) addresses P-wave

propagation from source array to focus point (CFP). This allows focusing at CFPs of interest without explicitly calculating the location of a conversion point.

#### 4.2.1 WRW FORMULATION FOR MULTI-COMPONENT DATA

The WRW formulation for P-wave reflection data has been discussed in chapter 2. It can be easily generalized to include any kind of mode conversions for reflection as well as propagation. The primary data matrix (Berkhout, 1987) can be written as

$$\mathbf{P}_0(z_r, z_s) = \mathbf{D}^{-1}(z_r) \mathbf{X}_0(z_r, z_s) \mathbf{S}^+(z_s), \quad (4.1)$$

where each column of source matrix  $\mathbf{S}^+(z_s)$  defines the downgoing source wavefield at the depth level  $z_s$  for one source array, and the corresponding columns of  $\mathbf{P}_0(z_r, z_s)$  define the resulting upgoing wavefields that are measured at the receiver array at the depth level  $z_r$ .  $\mathbf{D}^{-1}(z_r)$  is the detector array.  $\mathbf{X}_0(z_r, z_s)$  is the transfer function, one element of which defines the upgoing wavefield at one individual receiver element due to a unit source at one individual source point.

The transfer function  $\mathbf{X}_0(z_r, z_s)$  is defined as

$$\mathbf{X}_0(z_r, z_s) = \sum_{m=1}^M [\mathbf{W}^-(z_r, z_m) \mathbf{R}^+(z_m) \mathbf{W}^+(z_m, z_s)] , \quad (4.2)$$

where columns of  $\mathbf{W}^+(z_m, z_s)$  and rows of  $\mathbf{W}^-(z_r, z_m)$  define the propagation respectively between depth levels  $z_s$  and  $z_m$  and between  $z_m$  and  $z_r$ .  $\mathbf{R}^+(z_m)$  defines the reflection operator for the downgoing wavefields at depth level  $z_m$ .

The WRW model as given by equations (4.1) and (4.2) can be easily generalized to include any kind of mode conversion (reflection as well as propagation) for any wave type (P as well as S) at any emission ( $z_s$ ) and any detection ( $z_r$ ) level by defining the primary data matrix as



$$\mathbf{P}_0(z_r, z_s) = \begin{bmatrix} \mathbf{P}_{PP}(z_r, z_s) & \mathbf{P}_{PS}(z_r, z_s) \\ \mathbf{P}_{SP}(z_r, z_s) & \mathbf{P}_{SS}(z_r, z_s) \end{bmatrix}, \quad (4.3)$$

where  $\mathbf{P}_{PP}(z_r, z_s)$  defines P-P mode data (emission in P, detection in P),  $\mathbf{P}_{PS}(z_r, z_s)$  defines S-P mode data (emission in S, detection in P),  $\mathbf{P}_{SP}(z_r, z_s)$  defines P-S mode data (emission in P, detection in S) and  $\mathbf{P}_{SS}(z_r, z_s)$  defines S-S mode data (emission in S, detection in S). The source matrix  $\mathbf{S}^+(z_s)$  is defined as

$$\mathbf{S}^+(z_s) = \begin{bmatrix} \mathbf{S}_P(z_s) & \mathbf{0} \\ \mathbf{0} & \mathbf{S}_S(z_s) \end{bmatrix}, \quad (4.4)$$

where  $\mathbf{S}_P(z_s)$  is P-wave source matrix and  $\mathbf{S}_S(z_s)$  is S-wave source matrix. The upward propagation matrix  $\mathbf{W}^-(z_r, z_m)$  from level  $z_m$  to receiver level  $z_r$  is defined as

$$\mathbf{W}^-(z_r, z_m) = \begin{bmatrix} \mathbf{W}_{PP}(z_r, z_m) & \mathbf{W}_{PS}(z_r, z_m) \\ \mathbf{W}_{SP}(z_r, z_m) & \mathbf{W}_{SS}(z_r, z_m) \end{bmatrix}, \quad (4.5)$$

where  $\mathbf{W}_{PP}(z_r, z_m)$  represent upward propagation of reflected P-wave resulting from incident P-wave,  $\mathbf{W}_{PS}(z_r, z_m)$  represent upward propagation of reflected P-wave resulting from incident S-wave,  $\mathbf{W}_{SP}(z_r, z_m)$  represent upward propagation of reflected S-wave resulting from incident P-wave and  $\mathbf{W}_{SS}(z_r, z_m)$  represent upward propagation of S-wave resulting from incident S-wave. The downward propagation matrix  $\mathbf{W}^+(z_m, z_s)$  from level  $z_s$  to receiver level  $z_m$  is defined as

$$\mathbf{W}^+(z_m, z_s) = \begin{bmatrix} \mathbf{W}_{PP}(z_m, z_s) & \mathbf{W}_{PS}(z_m, z_s) \\ \mathbf{W}_{SP}(z_m, z_s) & \mathbf{W}_{SS}(z_m, z_s) \end{bmatrix}, \quad (4.6)$$

where  $\mathbf{W}_{PP}(z_m, z_s)$  represent downward propagation of source P-wave,  $\mathbf{W}_{PS}(z_m, z_s)$  represent downward propagation of source S-wave that gets mode-converted to P-wave at level  $z_m$ ,  $\mathbf{W}_{SP}(z_m, z_s)$  represent downward propagation of P-wave source that gets mode-converted to S-wave at level  $z_m$ , and  $\mathbf{W}_{SS}(z_r, z_m)$  represent

downward propagation of S-wave source that does not undergo mode conversion.

The reflection operator for downgoing wave is defined as

$$\mathbf{R}^+(z_m, z_m) = \begin{bmatrix} \mathbf{R}_{PP}^+(z_m, z_m) & \mathbf{R}_{PS}^+(z_m, z_m) \\ \mathbf{R}_{SP}^+(z_m, z_m) & \mathbf{R}_{SS}^+(z_m, z_m) \end{bmatrix}, \quad (4.7)$$

where  $\mathbf{R}_{PP}^+(z_m, z_m)$  represents reflection coefficients for incident P and reflected P wave at depth level m,  $\mathbf{R}_{PS}^+(z_m, z_m)$  represents reflection coefficients for incident S and reflected P wave,  $\mathbf{R}_{SP}^+(z_m, z_m)$  represents reflection coefficients for incident P and reflected S wave and  $\mathbf{R}_{SS}^+(z_m, z_m)$  represents reflection coefficients for incident S and reflected S wave. The detector matrix  $\mathbf{D}(z_s)$  is defined as

$$\mathbf{D}(z_s) = \begin{bmatrix} \mathbf{D}_P(z_r) & \mathbf{0} \\ \mathbf{0} & \mathbf{D}_S(z_r) \end{bmatrix}, \quad (4.8)$$

where  $\mathbf{D}_P(z_r)$  represents the P-wave detector matrix and  $\mathbf{D}_S(z_d)$  represents the S-wave detector matrix.

If the events due to mode conversion during one-way propagation (down or up) are neglected, then Equation 4.1 can be represented by four independent equations:

$$\mathbf{P}_{PP}(z_r, z_s) = \mathbf{D}_P(z_r) \sum_{m=1}^M [\mathbf{W}_{PP}^-(z_r, z_m) \mathbf{R}_{PP}^-(z_m, z_m) \mathbf{W}_{PP}^+(z_m, z_s)] \mathbf{S}_P(z_s), \quad (4.9)$$

$$\mathbf{P}_{SP}(z_r, z_s) = \mathbf{D}_S(z_r) \sum_{m=1}^M [\mathbf{W}_{SS}^-(z_r, z_m) \mathbf{R}_{SP}^-(z_m, z_m) \mathbf{W}_{PP}^+(z_m, z_s)] \mathbf{S}_P(z_s), \quad (4.10)$$

$$\mathbf{P}_{PS}(z_r, z_s) = \mathbf{D}_P(z_r) \sum_{m=1}^M [\mathbf{W}_{PP}^-(z_r, z_m) \mathbf{R}_{PS}^-(z_m, z_m) \mathbf{W}_{SS}^+(z_m, z_s)] \mathbf{S}_S(z_s), \quad (4.11)$$

$$\mathbf{P}_{SS}(z_r, z_s) = \mathbf{D}_S(z_r) \sum_{m=1}^M [\mathbf{W}_{SS}^-(z_r, z_m) \mathbf{R}_{SS}^-(z_m, z_m) \mathbf{W}_{SS}^+(z_m, z_s)] \mathbf{S}_S(z_s). \quad (4.12)$$

When the receiver side has both P and S-wave recording while the source side has only P-wave source (e.g. OBC data), equations (4.9) and (4.10) should be used. The expression for P-wave focusing operator (Equation 2.8) has been derived in

section 2.2.1 of chapter 2. The P-wave operator (Equation 2.8) for P-P data can be applied on mode converted P-S data to remove source side downward propagation effect. Similar to its P-wave counterpart, S-wave operator required for removing receiver side upward propagation for  $j^{\text{th}}$  grid point at  $m^{\text{th}}$  depth level is given by

$$\mathbf{F}_j(z_m, z_r) = [\mathbf{W}_{SS}^-(z_r, z_m)]^{-1} \mathbf{I}_j(z_m), \quad (4.13)$$

where  $\mathbf{F}_j(z_m, z_r)$  is S-wave focusing operator,  $\mathbf{W}_{SS}^-(z_r, z_m)$  is upward propagation matrix from depth level  $z_m$  to receiver level  $z_r$  and  $\mathbf{I}_j(z_m) = [0, 0, 0, \dots, 0, 1, 0, \dots, 0]^T$ , where 1 is positioned at the  $j^{\text{th}}$  location of this vector and corresponds to the grid point to be focused at the  $m^{\text{th}}$  depth.

#### 4.2.2 SPACE-TIME DOMAIN CFP ANALYSIS OF C-WAVE

The time domain version of S-wave focusing operator (Equation 4.13) defines one way propagation from gridpoint  $x_j$  at depth level  $z_m$  to the depth level of detectors  $z_r$ . Here I demonstrate the time domain focusing of P-P and P-Sv data for a simple layered vti medium. I use a synthetic data generated using staggered grid finite difference modeling that is 4<sup>th</sup> order in space and 2<sup>nd</sup> order in time (Virieux, 1986; Levander, 1988). In CFP analysis, the two steps of focusing can be applied interchangeably, i.e., focusing in detection (removal of receiver side propagation) followed by focusing in emission (removal of source side propagation) or vice-versa. Here I apply focusing in detection followed by focusing in emission.

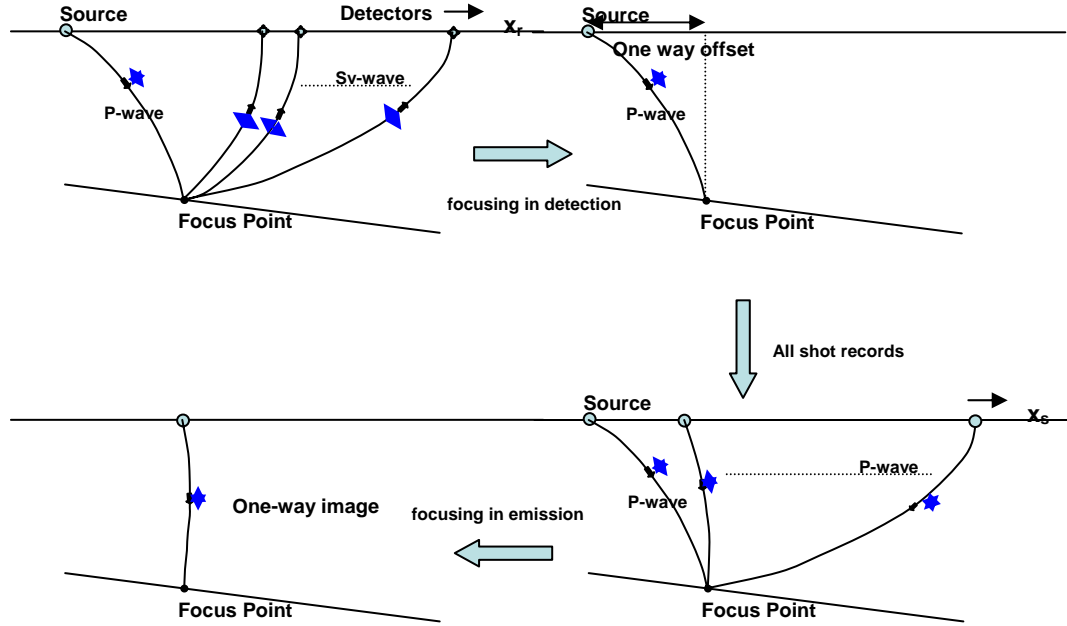


Figure 4.5: In the first focusing step, each shot record is transformed to one event of the focus-point response (Fresnel-zone stacking). In the second focusing step, all events in the focus point response are aligned at the one-way image time, followed by weighted superposition (CFP stacking). Note that here one-way image ray connects two points with the same lateral position; note also that the traveltime along this one-way image ray defines one-way image time.

Figure 4.6 (a) shows the receiver side P-wave operator representing P-wave traveltime from a grid point  $(x_j, z_m)$  to the receiver depth level  $z_r$  and Figure 4.6 (b) shows the receiver side Sv-wave operator representing Sv-wave traveltime from grid point  $(x_j, z_m)$  to receiver depth level  $z_r$ . For an identical source-receiver position, the source side P-wave operator is the same as receiver side P-wave operator (Figure 4.6 (a)). First, I perform focusing in detection by applying the P-wave operator on P-P data and Sv-wave operator on P-Sv data. This results in a

CFP gather which is the P-wave response of the focus point  $(x_j, z_m)$  to the source level  $z_s$ . For correct elastic parameters, the resulting gathers look identical to the P-wave operator (Figure 4.7 (a) and (b) and Figure 4.8 (a) and (b)). The traveltimes error can be obtained by cross-correlating the CFP operator and CFP gather. For correct model parameters, this results in zero differential time shifts (DTSSs) (Figure 4.9 (a) and (b)). However, neglecting anisotropy in velocity model results in non-identical operator and CFP response (Figure (4.10) (a) and (b); Figure 4.11 (a) and (b)) and non-zeros DTSSs (Figure 4.12 (a) and (b)). The error can be picked from DTS panel using a graphical interface and can be used iteratively to obtain updates of erroneous parameters.

#### **4.2.3 PLANE WAVE DOMAIN CFP ANALYSIS OF C-WAVE**

Ferguson and Sen (2004) use the CFP method in the plane wave domain to estimate the elastic parameters of anisotropic media using joint inversion of P-P and Sv-Sv wave traveltimes. A summary of this method has been presented in Section 2.2.3 of Chapter 2. For P-Sv mode data, the methodology differs only in the fact that the receiver side focusing, i.e. focusing in detection is done in Sv-wave while source side focusing, i.e. focusing in emission is done in P-wave. For P-P mode, the procedure remains same as explained in Chapter 2. The plane wave domain analysis is particularly significant for analysis of converted wave as space-time domain inversion gets complicated due to triplication of Sv mode (Baan and Kendall, 2002). For analysis of synthetic data for the elastic model based on Blackfoot geology, I use plane wave ( $\tau$ - $p$ ) domain analysis due to Ferguson and Sen, 2002.

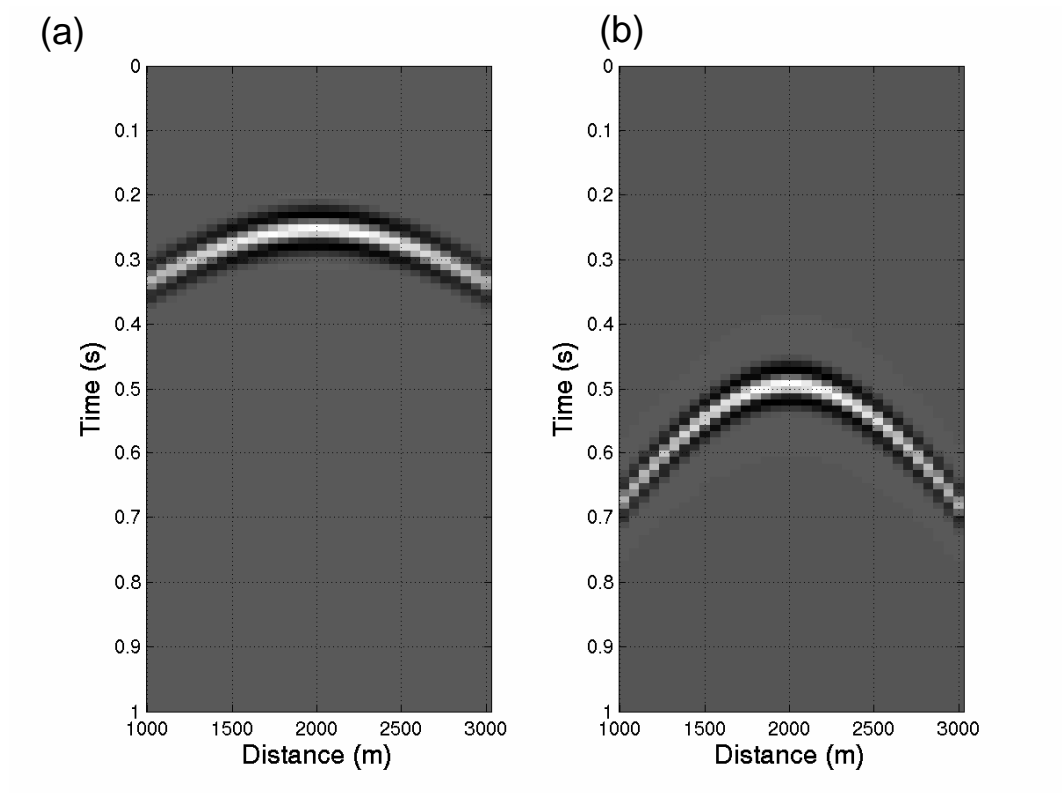


Figure 4.6: (a) P-wave focusing operator used for focusing P-P data, (b) Sv-wave focusing operator used for focusing converted wave P-Sv data.

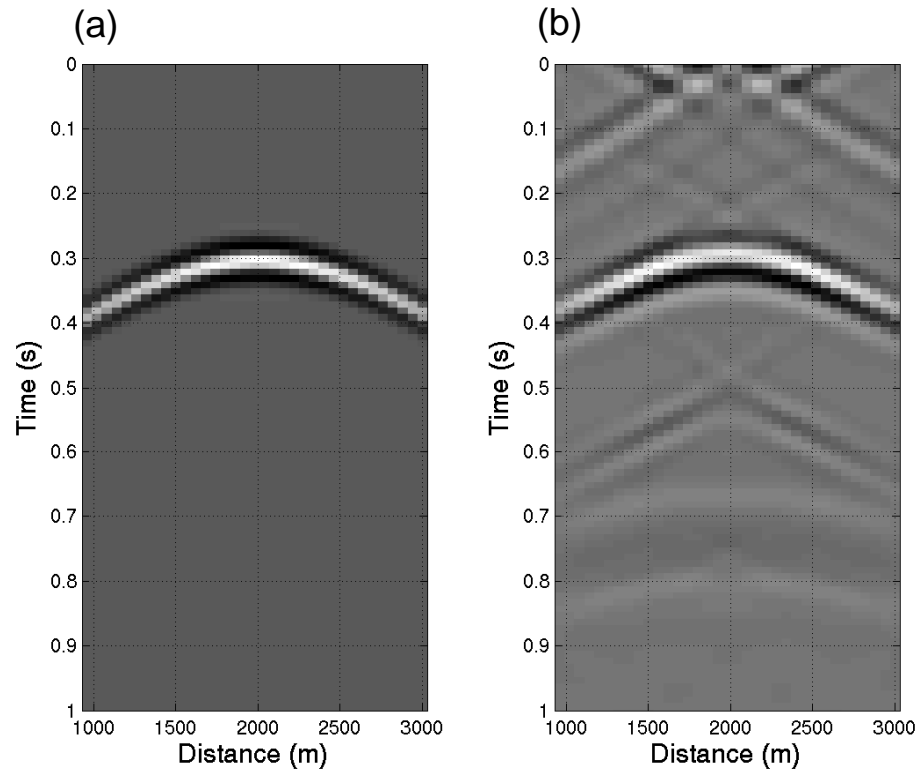


Figure 4.7: (a) P-wave focusing operator versus (b) CFP gather for P-P data after focusing at receiver end using P-wave focusing operator in Fig. 4.6 (a).

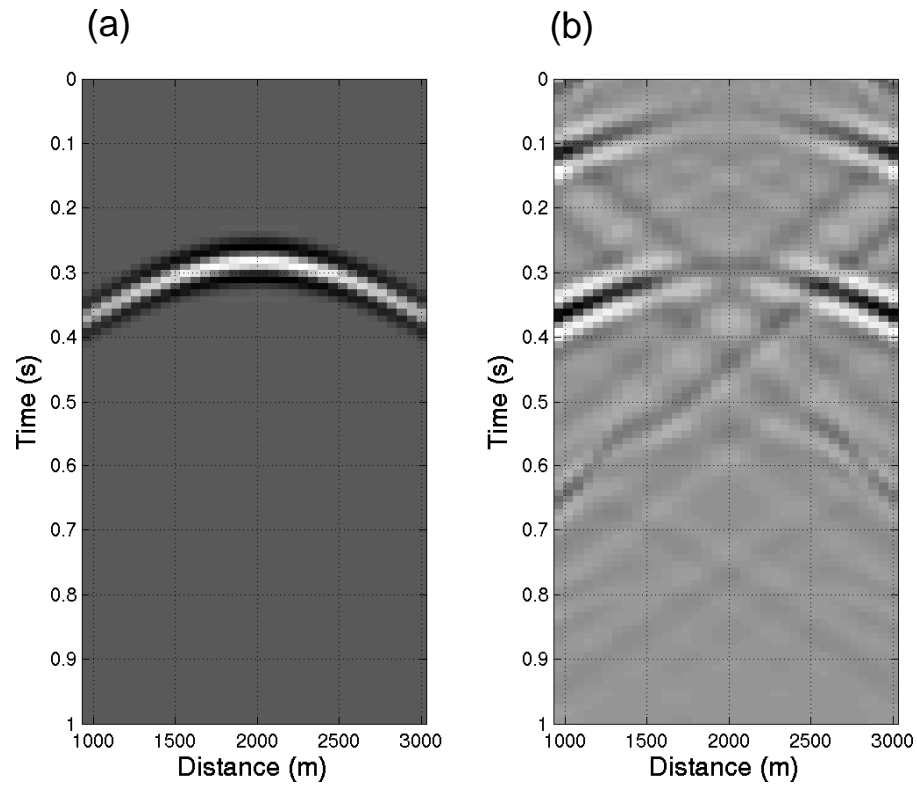


Figure 4.8: (a) P-wave focusing operator versus (b) CFP gather for P-Sv data after focusing at receiver end using Sv-wave focusing operator in Fig. 4.6 (b).



### 4.3 METHOD

In the Blackfoot field, the anisotropic layers of coal and shales overlying the target channel (Figure 4.4) are flat. This makes layer based model parameterization simpler. Each layer can be represented by a set of model parameters  $\mathbf{m}=[\alpha_0 \ \beta_0 \ \varepsilon \ \delta \ z]^T$ . For joint inversion, error involved in P-wave and Sv-wave propagation can be obtained by picking DTSs obtained using the steps outlined in the previous section. In  $\tau$ - $p$  domain, the DTSs resulting from P-P data represent error in two-way vertical delay time ( $\tau$ ) for P-wave corresponding to different horizontal slownesses ( $\mathbf{p}$ ). The DTSs resulting from P-Sv data represent the sum of error in one way P-wave propagation from depth level of focus point to depth level of source locations and one-way Sv-wave propagation from depth level of focus point to depth level of receiver locations corresponding to different horizontal slownesses ( $\mathbf{p}$ ). Let  $f_k^{PP}$  represent the DTSs measured for  $N_{PP}$  horizontal slownesses where  $1 \leq k \leq N_{PP}$ ,  $f_k^{PSv}$  represent the DTSs measured for  $N_{PSv}$  horizontal slownesses where  $1 \leq k \leq N_{PSv}$  and let  $m_j$  represent the model for  $M$  anisotropic-parameters where  $1 \leq j \leq M$ . As shown in Chapter 2, model update can be obtained by solving a set of over-determined linear equations for the variable updates  $\delta\mathbf{m}$  according to

$$\mathbf{G}\delta\mathbf{m} = -\mathbf{f}, \quad (4.14)$$

where,

$$\mathbf{G} = \begin{bmatrix} \frac{\partial f_1^{PP}}{\partial \alpha_0} & \frac{\partial f_1^{PP}}{\partial \beta_0} & \frac{\partial f_1^{PP}}{\partial \varepsilon} & \frac{\partial f_1^{PP}}{\partial \delta} & \frac{\partial f_1^{PP}}{\partial z} \\ \frac{\partial f_2^{PP}}{\partial \alpha_0} & \frac{\partial f_2^{PP}}{\partial \beta_0} & \frac{\partial f_2^{PP}}{\partial \varepsilon} & \frac{\partial f_2^{PP}}{\partial \delta} & \frac{\partial f_2^{PP}}{\partial z} \\ \vdots & \vdots & \vdots & \vdots & \vdots \\ \frac{\partial \dot{f}_{N_{PP}}^{PP}}{\partial \alpha_0} & \frac{\partial \dot{f}_{N_{PP}}^{PP}}{\partial \beta_0} & \frac{\partial \dot{f}_{N_{PP}}^{PP}}{\partial \varepsilon} & \frac{\partial \dot{f}_{N_{PP}}^{PP}}{\partial \delta} & \frac{\partial \dot{f}_{N_{PP}}^{PP}}{\partial z} \\ \frac{\partial f_1^{PSv}}{\partial \alpha_0} & \frac{\partial f_1^{PSv}}{\partial \beta_0} & \frac{\partial f_1^{PSv}}{\partial \varepsilon} & \frac{\partial f_1^{PSv}}{\partial \delta} & \frac{\partial f_1^{PSv}}{\partial z} \\ \frac{\partial f_2^{PSv}}{\partial \alpha_0} & \frac{\partial f_2^{PSv}}{\partial \beta_0} & \frac{\partial f_2^{PSv}}{\partial \varepsilon} & \frac{\partial f_2^{PSv}}{\partial \delta} & \frac{\partial f_2^{PSv}}{\partial z} \\ \vdots & \vdots & \vdots & \vdots & \vdots \\ \frac{\partial \dot{f}_{N_{PSv}}^{PSv}}{\partial \alpha_0} & \frac{\partial \dot{f}_{N_{PSv}}^{PSv}}{\partial \beta_0} & \frac{\partial \dot{f}_{N_{PSv}}^{PSv}}{\partial \varepsilon} & \frac{\partial \dot{f}_{N_{PSv}}^{PSv}}{\partial \delta} & \frac{\partial \dot{f}_{N_{PSv}}^{PSv}}{\partial z} \end{bmatrix}, \quad (4.15)$$

$$\delta \mathbf{m} = [\Delta \alpha_0 \quad \Delta \beta_0 \quad \Delta \varepsilon \quad \Delta \delta \quad \Delta z]^T, \quad (4.16)$$

and

$$\mathbf{f} = [f_1^{PP} \quad f_2^{PP} \quad \dots \quad f_{N_{PP}}^{PP} \quad f_1^{PSv} \quad f_2^{PSv} \quad \dots \quad f_{N_{PSv}}^{PSv}]^T.$$

The solution for the model updates  $\delta \mathbf{m}$  is obtained by solving the over-determined Equation 4.14 in the least square sense by minimizing the  $L_2$  norm of objective function  $\|\mathbf{G} \delta \mathbf{m} + \mathbf{f}\|^2$  (Menke, 1989, page 36) as

$$\delta \mathbf{m} = -(\mathbf{G}^T \mathbf{G})^{-1} \mathbf{G}^T \mathbf{f} \quad (4.17)$$

The DTSs for P-P and P-Sv data can be written as

$$\mathbf{f}^{PP} = 2 \times (\boldsymbol{\tau}_{\text{real}}^P - \boldsymbol{\tau}^P(\mathbf{m})), \quad (4.18)$$

$$\mathbf{f}^{PSv} = (\boldsymbol{\tau}_{\text{real}}^P - \boldsymbol{\tau}^P(\mathbf{m})) + (\boldsymbol{\tau}_{\text{real}}^{Sv} - \boldsymbol{\tau}^{Sv}(\mathbf{m})). \quad (4.19)$$

The partial derivatives of Equation 4.18 and 4.19 give

$$\frac{\partial \mathbf{f}^{\text{PP}}}{\partial m_k} = -2 \times \frac{\partial \boldsymbol{\tau}^{\text{P}}}{\partial m_k} , \quad (4.20)$$

$$\frac{\partial \mathbf{f}^{\text{PSv}}}{\partial m_k} = - \left( \frac{\partial \boldsymbol{\tau}^{\text{P}}}{\partial m_k} + \frac{\partial \boldsymbol{\tau}^{\text{Sv}}}{\partial m_k} \right) . \quad (4.21)$$

For TI anisotropy, exact analytical expressions for vertical delay time ( $\tau$ ) in terms of horizontal slowness and Thomsen's parameters exist. I use the exact analytical partial derivatives of vertical delay time ( $\tau$ ) with respect to Thomsen's parameters to build the  $\mathbf{G}$  matrix using equations 4.20 and 4.21. The model update obtained using Equation (4.17) is applied iteratively until near zero DTSs ( $\mathbf{f}$ ) are obtained.

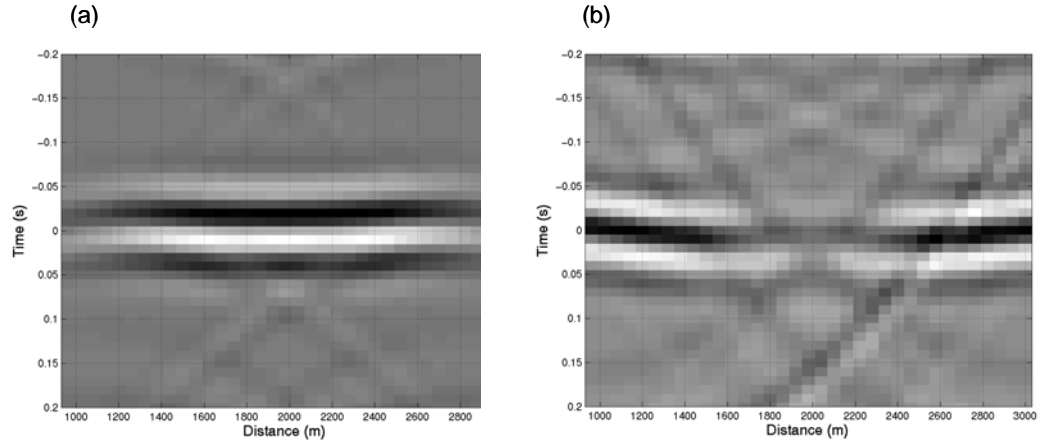


Figure 4.9: (a) DTS panel obtained by cross-correlating P-wave operator in Fig. 4.7 (a) and CFP gather in Fig. 4.7 (b), (b) DTS panel obtained by cross-correlating P-wave operator in Fig. 4.8 (a) and CFP gather in Fig. 4.8 (b).

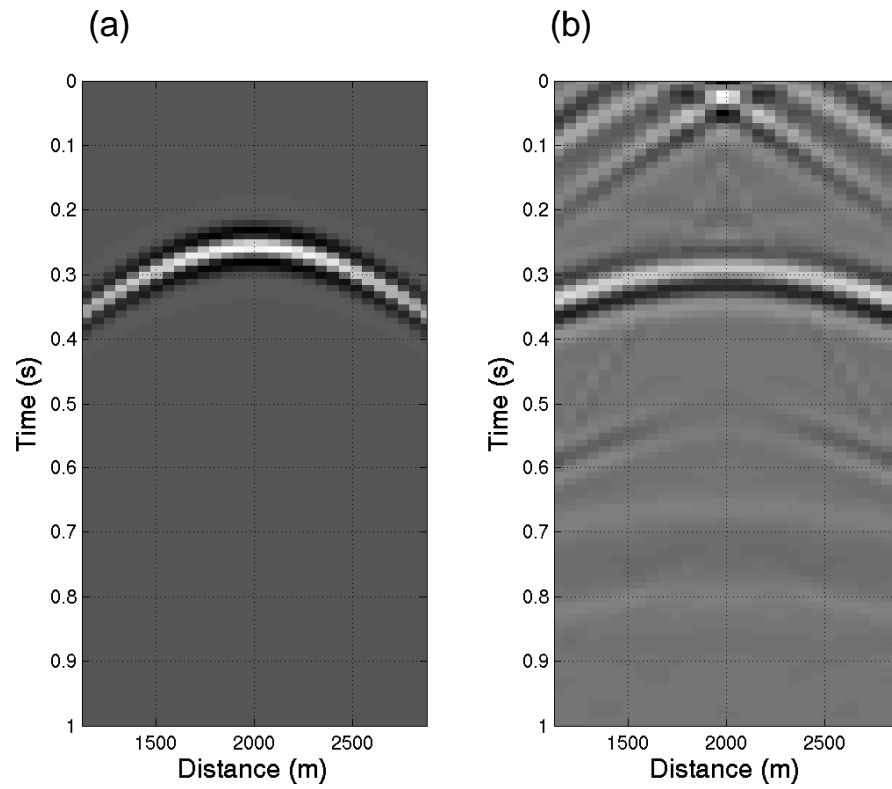


Figure 4.10: (a) P-wave focusing operator versus (b) CFP gather for P-P data for 10% error in model parameters.

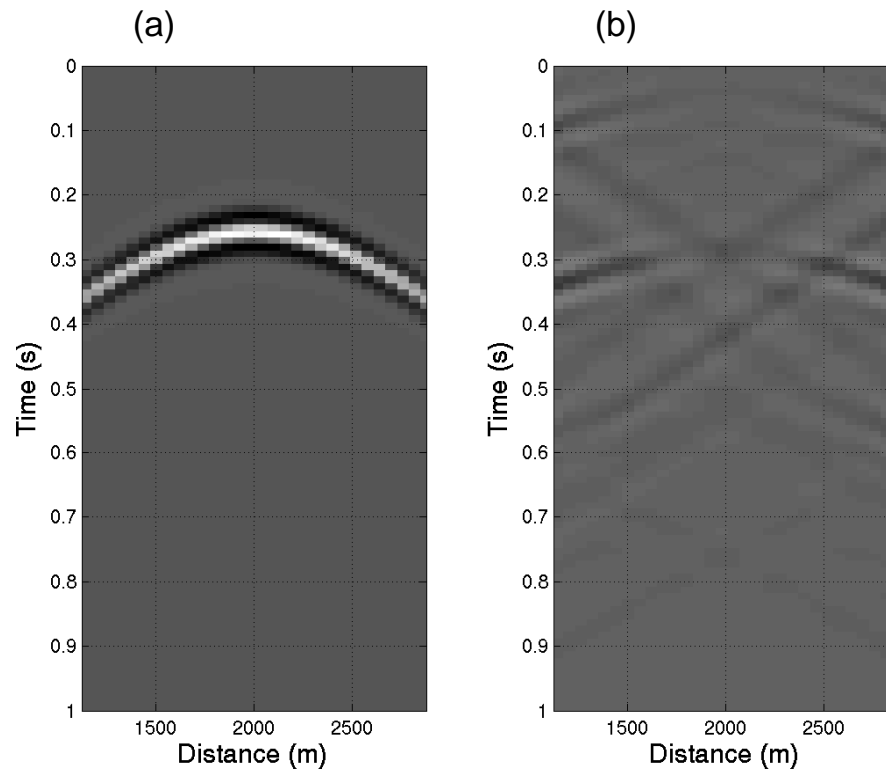


Figure 4.11: (a) P-wave focusing operator versus (b) CFP gather for P-Sv data for 10% error in model parameters.

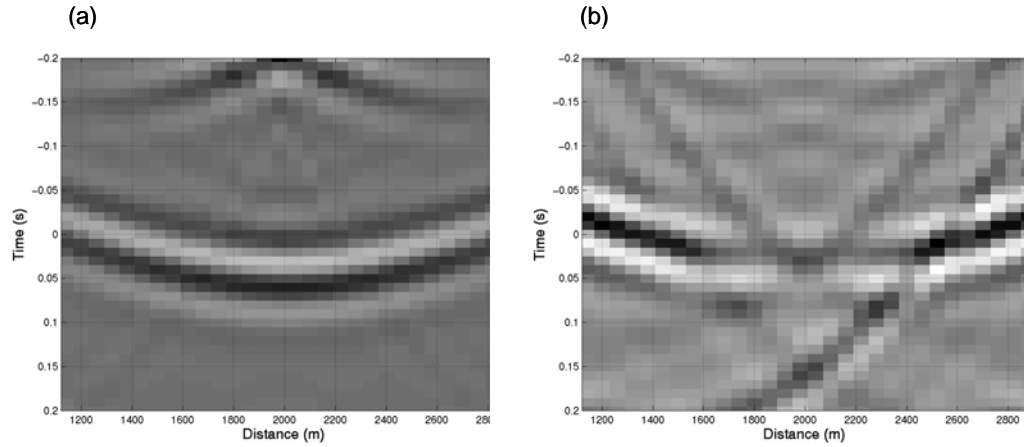


Figure 4.12: (a) DTS panel obtained by cross-correlating P-wave operator in Fig. 4.10 (a) and CFP gather in Fig. 4.10 (b), (b) DTS panel obtained by cross-correlating P-wave operator in Fig. 4.11 (a) and CFP gather in Fig. 4.11 (b) for 10% erroneous model.

#### 4.4 ANALYTIC EXAMPLE

In the Blackfoot field, the target zone is located at a depth of approximately 1700 m. The layers thicknesses are in the range of 40 to 120 m. This allows very small aperture even when maximum offset to depth ratio is high. The small thicknesses of layers lead to increased uncertainty in correct picking of a particular event. Moreover, the effect of anisotropy on traveltimes resulting from thin layers is very small and difficult to identify in limited aperture, limited bandwidth data. This makes estimation of local parameters based on layer-stripping difficult and unstable.

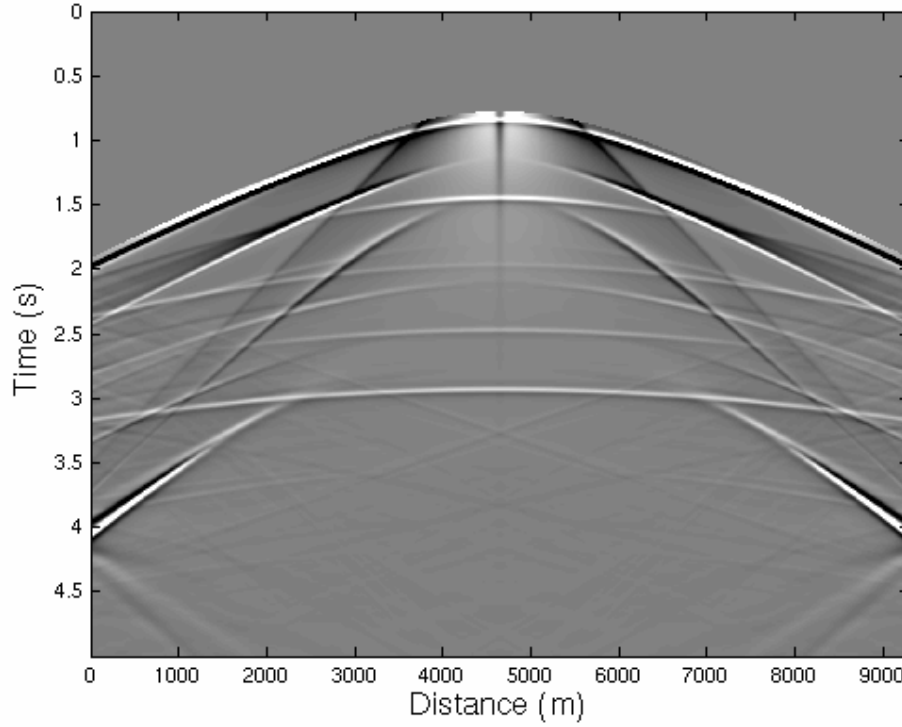


Figure 4.13: The z-component of shot gather generated by finite differencing modeling for an elastic model based on Blackfoot geology after removal of direct arrival.

For the given geology, first I perform joint inversion analytically by assuming that there is no noise or picking error. For no noise, the joint inversion of P-wave response and Sv-wave response gives a constrained estimate for most of the anisotropic layers (Table 4.1). However, this is an ideal condition. Real data invariably contains noise. So I introduce random noise of the order of 1 ms that may be associated with very small picking error in a high quality data. For this case also I am able to obtain parameter estimates which are reasonably close to the real values for most layers (Table 4.1). However, when I introduce random

error of the order of 10 ms which is reasonable for the Blackfoot model, the inversion becomes unstable for anisotropic layers (Table 4.1). Thus it is very difficult to obtain anisotropic parameter estimate for each layer overlying the channel. Instead the average parameter for the coal and shale layers overlying the channel should be obtained and used for estimation of depth of channels.

Layer	Real parameters	Parameters after Inversion		
		No error	1 mils random error	10 mils random error
Isotropic Overburden	$\alpha_0=2860$ m/s $\beta_0=1430$ m/s $z=1710$ m	2860 m/s 1430 m/s 1710 m	2860.1 m/s 1430.1 m/s 1710.1 m	2859.5 m/s 1429.8 m/s 1709.8 m
Fisch Scale Zone	$\alpha_0=3300$ m/s $\beta_0=1520$ m/s $\varepsilon=0.23$ $\delta=0.06$ $z=120$ m	3670 m/s 1689.7 m/s 0.0152 0.0232 133.4 m	3735 m/s 1721.5 m/s 0.0075 0.0282 135.9 m	unstable
Mannville Coal	$\alpha_0=3860$ m/s $\beta_0=2322$ m/s $\varepsilon=0.189$ $\delta=0.204$ $z=90$ m	3859.2 m/s 2329.8 m/s 0.1844 0.2040 90.2 m	3903 m/s 2349 m/s 0.136 0.1738 90.7 m	unstable
Glaucinite Shale	$\alpha_0=3945$ m/s $\beta_0=2025$ m/s $\varepsilon=0.24$ $\delta=0.12$ $z=90$ m	4004 m/s 2057 m/s 0.213 0.1207 91.4 m	4184 m/s 2168 m/s 0.1042 0.0921 95.9 m	unstable
Glaucinite Channel porous	$\alpha_0=4300$ m/s $\beta_0=2513$ m/s $\varepsilon=0.097$ $\delta=0.091$ $z=40$ m	4285 m/s 2506 m/s 0.0888 0.0915 39.9 m	4317 m/s 2570 m/s 0.0747 0.1306 40.2 m	unstable

Table 4.1: Result of analytic inversion for the anisotropic layers in the Blackfoot model.



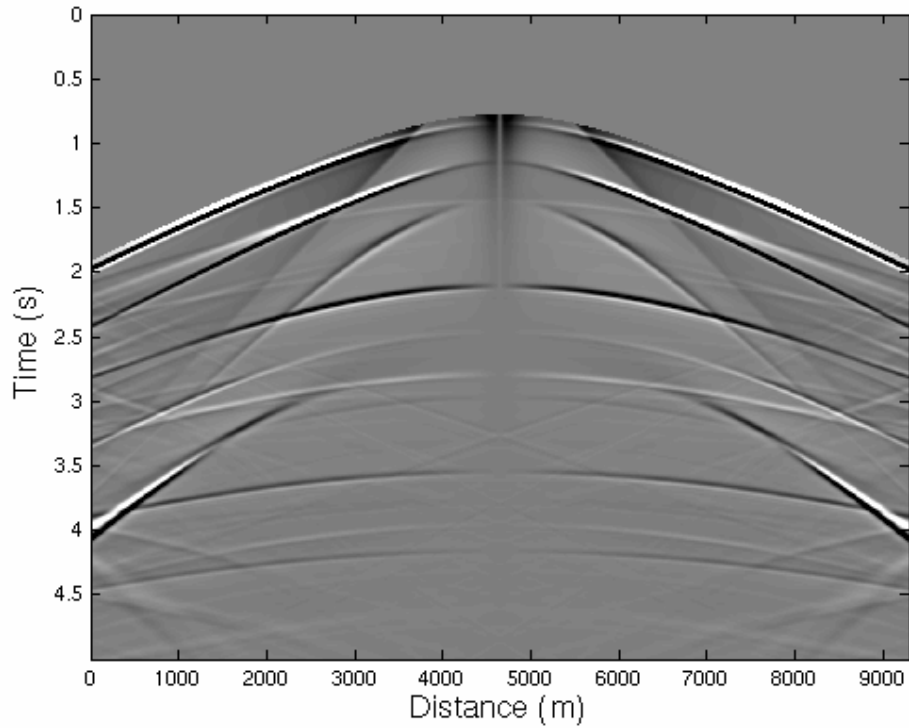


Figure 4.14: The x-component of shot gather generated by finite differencing modeling for an elastic model based on Blackfoot geology after removal of direct arrivals.

#### 4.5 SYNTHETIC DATA EXAMPLE

The results of analytic inversion suggest that it is difficult to obtain a constrained estimate of anisotropic parameters and depth for each layer by using joint inversion of P-P and P-Sv data for the true geology of Blackfoot field. However, to test the effectiveness of joint inversion in constraining parameter estimates, I create a model with similar geology as Blackfoot field but with greatly amplified layer thicknesses. For this model, I generate synthetic data using

staggered grid finite differencing, 4<sup>th</sup> order in space and 2<sup>nd</sup> order in time (Virieux, 1986; Levander, 1988). Figure 4.13 shows the vertical component and Figure 4.14 shows the horizontal component of recorded data after removal of direct arrival and some preprocessing. I apply a radon transform to convert the data from  $x-t$  domain to  $\tau-p$  domain. Figure 4.15 and 4.16 show the vertical and horizontal component of recorded data in  $\tau-p$  domain. The P-P and P-Sv data cannot be separated completely as both are present in each recording component (vertical and horizontal) of data. The vertical component predominantly represents the P-P data and the horizontal component predominantly represents P-Sv data. I perform inversion in a layer-stripping fashion. Here I present the result of inversion for Fisch Scale zone formation. I use the  $\tau-p$  domain version of CFP method to obtain traveltimes errors (DTSS). Figure 4.17 and 4.18 show the DTS picking for P-P and P-Sv data for initial guess model. After a few iterations, I obtain a parameter set that makes the DTSSs for both P-P and P-Sv data nearly zero (Figure 4.19 and 4.20). Table 4.2 shows the true parameter and the parameter obtained from inversion. The parameters obtained from inversion are fairly close to true parameters.

Parameters	Effective Parameter	Inverted Parameter
$\alpha_0$	3300 m/s	3324 m/s
$\beta_0$	1520 m/s	1500 m/s
$\varepsilon$	0.23	0.27
$\delta$	0.06	0.007
$z$	1000 m	1005 m

Table 4.2: Results of parameter inversion using CFP method for the anisotropic parameters of Fisch Scale layer in the Blackfoot model.

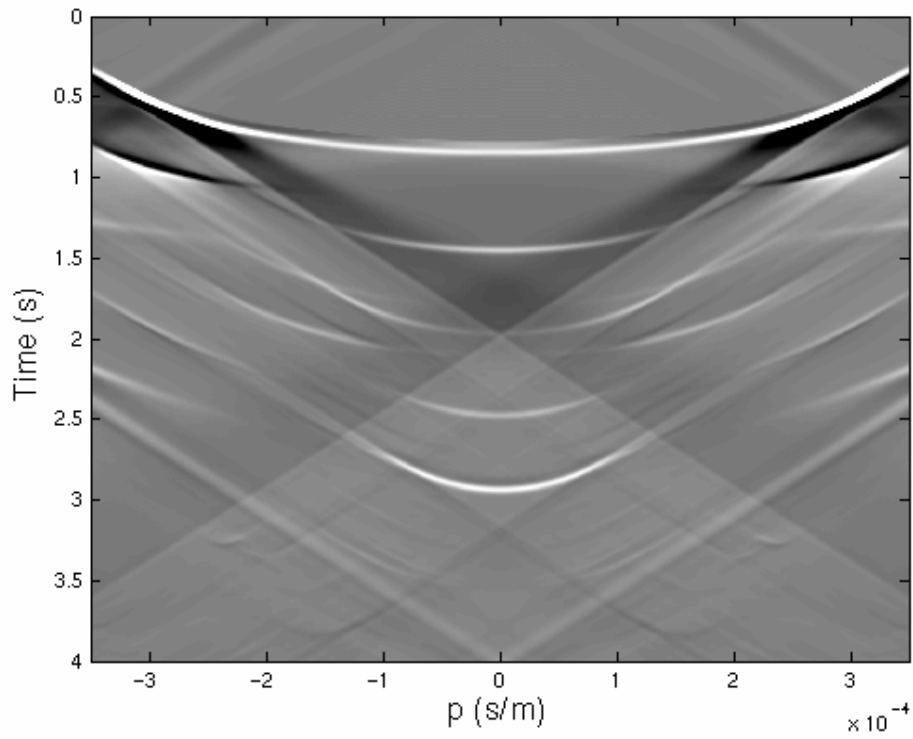


Figure 4.15: The z-component of shot gather in Figure 4.13, after performing radon transformation.

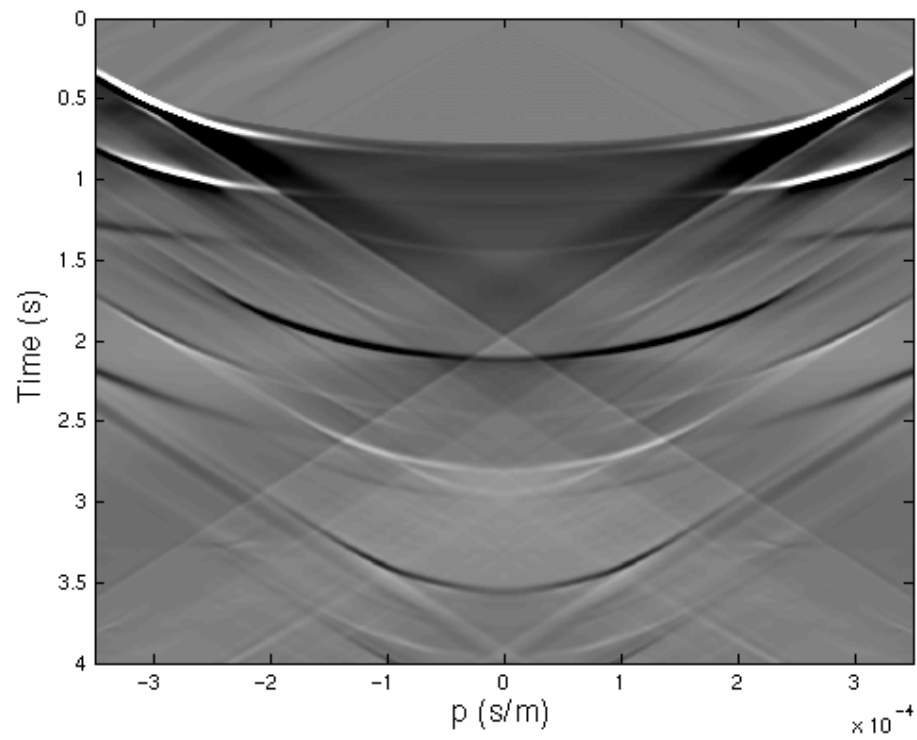


Figure 4.16: (a) The x-component of shot gather in Figure 4.13, after performing radon transformation.

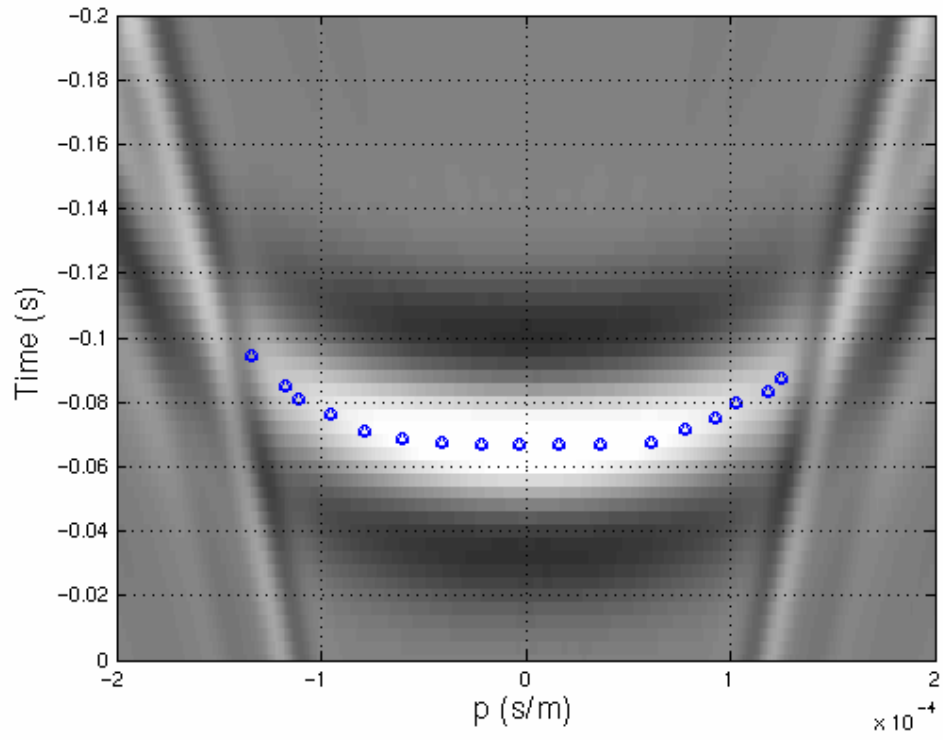


Figure 4.17: The picking of differential time shift (DTS) on P-P mode data for the initial guess model.

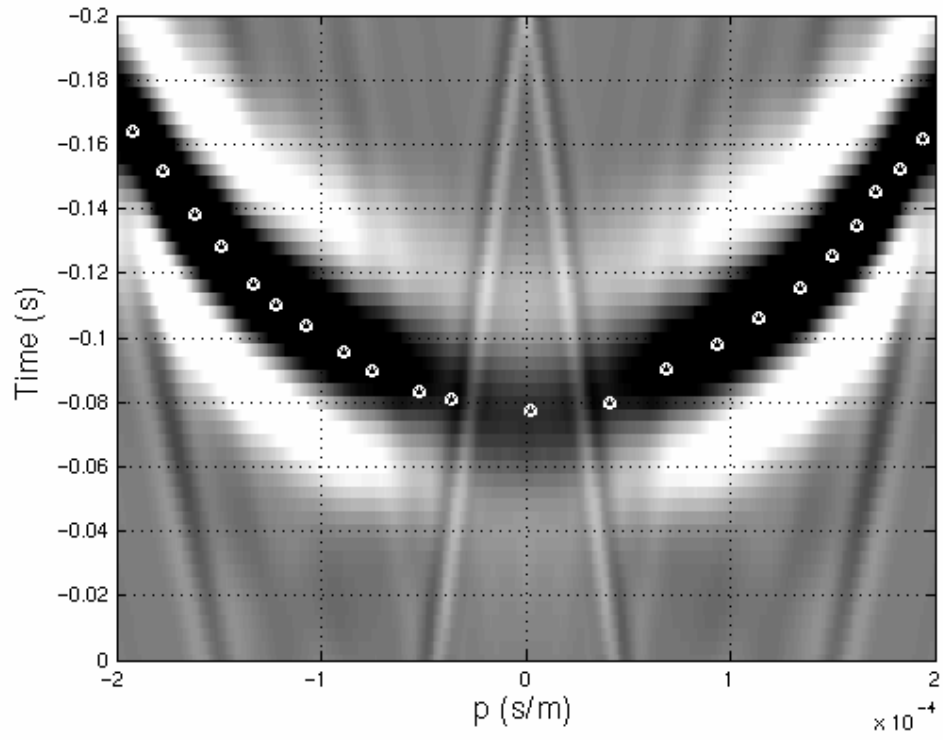


Figure 4.18: The picking of differential time shift (DTS) on P-Sv mode data for the initial guess model.

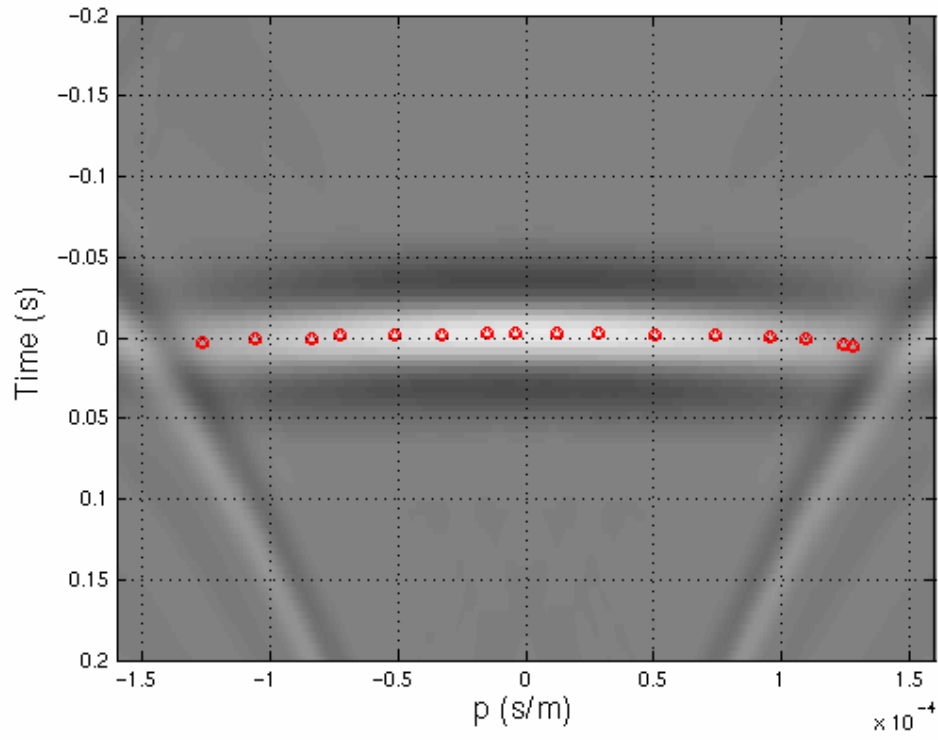


Figure 4.19: The picking of differential time shift (DTS) on P-P mode data for the model after inversion.

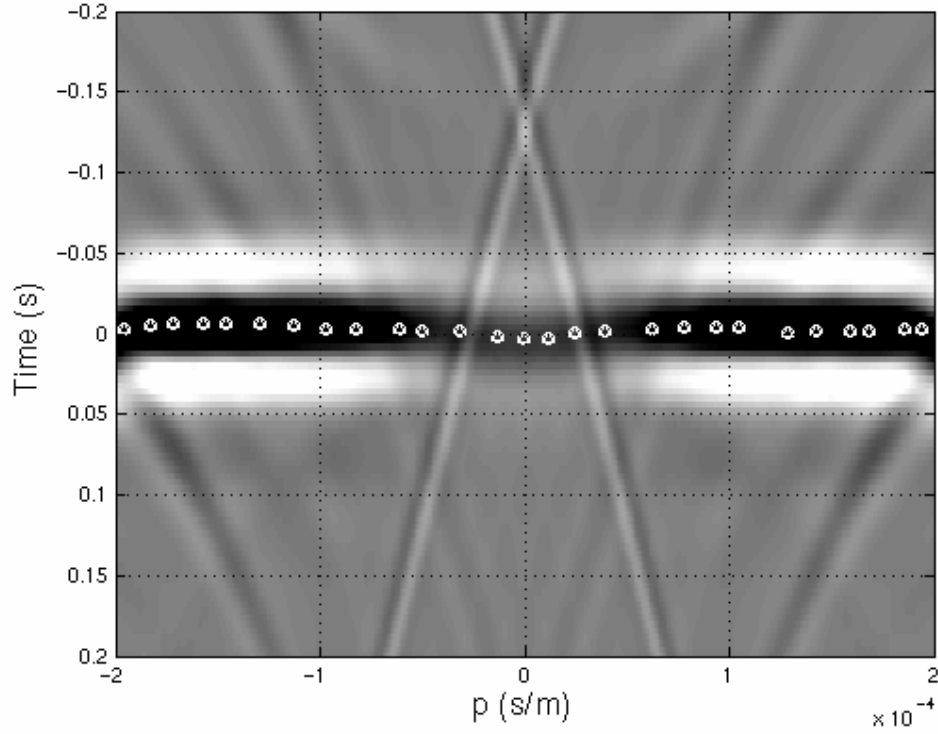


Figure 4.20: The picking of differential time shift (DTS) on P-Sv mode data for the model obtained from inversion.

#### 4.6 SUMMARY

CFP domain analysis has advantages in dealing with converted wave (P-Sv) data due to separate focusing at receiver side and source side. This obviates the need of data binning based on estimation of common conversion point (CCP) location. The joint inversion in  $\tau$ - $p$  domain has been performed on synthetic dataset for the geology encountered in the Blackfoot field. The analytic joint inversion of P-P and P-Sv traveltimes for the given model yields satisfactory result when picking uncertainty and noise level is extremely low. However, when the



picking uncertainty is moderate, the inversion becomes unstable. The cause of instability in inversion lies in very small effect of anisotropy on traveltime due to the small thicknesses of anisotropic layers. To demonstrate the efficacy of joint inversion in constrained estimation of depth as well as anisotropic parameters, I build a model having same geology but increased layer thicknesses. The result of inversion using synthetic dataset for this model is stable and yields values close to the true parameter values.

## **Chapter 5: Summary and future work**

### **5.1 SUMMARY**

When the subsurface is heterogeneous and/or anisotropic, prestack depth migration of seismic reflection data using a subsurface model derived from isotropic velocity analysis may lead to incorrect positioning of the target reflector in depth image. This may result in erroneous interpretation of the target zone. The source of error is often not the forward problem of wave propagation, but the incorrect or insufficient elastic parameters (e.g. neglecting anisotropy) derived from inversion. The problem with anisotropy estimation is it being highly sensitive to noise requires very precise mapping of moveout residual to error in model parameter. The NMO based analysis is not suitable for complex geology as it is based on assumption of flat or constantly dipping layers. The CIG method gives the residual moveout in terms of depth error. The CFP domain analysis has an advantage in the fact that the error is given in time and mapping of error in travelttime to the error in model parameters becomes more robust. The CFP domain analysis has been used to estimate isotropic heterogeneous subsurface velocity model (Kabir, 1997). For my research, I extend the CFP based analysis to the estimation of anisotropic parameters for a heterogeneous subsurface.

Our ability to estimate subsurface model depends on several factors like source-receiver geometry (e.g. maximum reflection aperture for target horizon), type of data (e.g. single component versus multi-component), amount of noise, temporal resolution of data etc. For a given geological setting and data acquisition

it is important to evaluate our ability or limitation in estimating subsurface elastic parameters which in turn can aid in assessment of risk involved with a certain interpretation. Common Focus Point (CFP) domain prestack velocity analysis using a layer-stripping approach can help in isolating the effects of anisotropy from the imprints of complex overburden. This makes it possible to quantitatively analyze the effects of acquisition geometry, temporal and spatial bandwidth on the uncertainty associated with parameter estimation. In this dissertation, the uncertainty associated with anisotropic parameter estimation for a transversely isotropic (TI) media have been assessed quantitatively under different experimental settings. The experimental conditions include maximum offset to depth ratio (spatial aperture), layer thickness, tilt in symmetry axis of TI medium, and the use of mode converted data.

In Chapter 1, the key concepts like anisotropy, migration velocity analysis, inversion, sensitivity analysis etc. that are integral to elastic parameter estimation using seismic reflection data have been introduced and defined. Also the objective and organization of my dissertation have been provided in this chapter.

As explained in chapter 2, the *Common Focus Point* (CFP) technology defines a recent method of prestack migration velocity analysis which has several advantages over other popular methods. One remarkable advantage is that the imaging error is given directly in time allowing easier model updates through inversion. The CFP technique has been used in recent past for estimating isotropic heterogeneous velocity model for geologically complex subsurface. For my research, this method has been extended to anisotropic parameter inversion by

suitable implementation of the space-time domain version of CFP method for picking the traveltimes error resulting from the incorrect guess model. This approach has been successfully implemented for anisotropy estimation of the shale thrust-sheets in the Canadian Foothills model. This model had targets of interest below transversely isotropic shale thrust-sheets and estimating anisotropic parameters was important for proper depth imaging of target zone. The synthetic P-mode data used for the analysis has been generated using a finite difference algorithm.

In chapter 3, the advantages or limitations of CFP domain velocity analysis in estimating the anisotropic parameters has been assessed quantitatively. To this end, a *sensitivity analysis* has been performed under different experimental settings like different observation apertures, layer thicknesses, tilt in symmetry axis, picking error and the use of mode converted data. The results have quantitatively established the advantage of joint inversion of P-P and Sv-Sv data or P-P and P-Sv data over the conventional inversion of solely P-P data in constraining the depth and anisotropic parameters. Also it has been established that the constraint on parameter estimation improves with increase in angle of tilt of symmetry axis with respect to the reflector.

In chapter 4, the advantages of CFP domain analysis in dealing with mode converted P-Sv data has been shown by focusing of different wave types at the receiver side and the source side. In complex media, this helps avoid the cumbersome calculation of common conversion point (CCP) location. The CFP analysis has been applied for estimating anisotropic parameters as well as layer

thickness by *joint inversion* of P-P and P-Sv synthetic data for the geology encountered in Blackfoot field.

## **5.2 FUTURE WORK**

Here I have used manual picking of traveltime error from a graphical display of DTS panel. For inversion I have used quasi-linear approach of Newton's method for obtaining parameter updates. For complex models, the manual picking at every analysis point may be cumbersome and prone to error. So for future research, I suggest the use of global optimization approach of Very Fast Simulated Annealing (VFSA) (Varela et al., 1998; Sen and Stoffa, 1995). For this approach, interpreter intervention will be required only to restrict the search space (Varela et al., 1998).

I also suggest a similar sensitivity analysis to study the resolvability of vertical or lateral velocity gradients and the anisotropic parameters. It may give insight into the resolvability of heterogeneity from anisotropy when they are present simultaneously. The analysis can also be extended to azimuthally anisotropic media. Uncertainty estimation based on the theory presented here can also be used to predict the success of amplitude variation with offset (AVO) analysis for a given geological and data acquisition setting.

In the current research, I use first arrival travel times to generate focusing operators. Though velocity analysis using first arrival was adequate for this research, in more complex situations the strongest reflected energy may not correspond to first arrival. A more adequate operator should be built that takes

into account triplications and multi-pathing. Further research may be carried out to design such operators without significant loss of efficiency.

An important constraint on use of CFP domain velocity analysis and migration is that it is computationally expensive. This makes its application to 3-D data and velocity models very difficult. However, it is possible to make CFP technology more efficient by use of parallel computing. The data can be decomposed into different frequency components and the processing for each component can be distributed to different processors and finally the results can be combined. For future research, I suggest that an algorithm should be developed that makes use of parallel computing to make this analysis feasible and useful for 3-D analysis of large datasets.

## References

- Ahmed, I., 2003, Imaging the Lower Slope, Offshore Nicaragua and Costa Rica using a New Residual Migration Velocity Analysis Technique in the Space-Offset domain: Ph.D. thesis, University of Texas at Austin.
- Alkhalifah, T., 1996, Transformation to zero offset in transversely isotropic media: *Geophysics*, 61, 947-963.
- Alkhalifah, T., 1997, Velocity analysis using nonhyperbolic moveout in transversely isotropic media: *Geophysics*, 62, 1839-1854.
- Alkhalifah, T., and Tsvankin, I., 1995, Velocity analysis for transversely isotropic media: *Geophysics*, 60, 1550-1566.
- Al-Chalabi, M., 1973, Series approximations in velocity and traveltimes computations: *Geophys. Prosp.*, 21, 783-795.
- Al-Yahya, K., 1989, Velocity analysis by iterative profile migration, *Geophysics*, 54, 718-729.
- Anderson, D. L., Minster, B. and Cole, N., 1974, The effect of oriented cracks on seismic velocities: *J. Geophys. Res.*, 79, 4011-4015.
- Ata, E., and Michelena, R. J., 1995, Mapping distribution of fractures in a reservoir with P-S converted waves: *The Leading Edge*, 14, no. 6, 664-673.
- baan, M. van der and Kendall, J. M., 2002, Estimating anisotropy parameters and traveltimes in the  $\tau$ -p domain, *Geophysics*, 67, 1076-1086.
- Backus, G. E., 1962, Long-wave elastic anisotropy produced by horizontal layering: *J. Geophys. Res.*, 67, 4427-4440.
- Bamford, D. and Nunn, K. R., 1979, In situ seismic measurements of crack anisotropy in the carboniferous limestone of northwest England: *Geophys. Pros.*, 27, 322-338.
- Banik, N.C., 1984, Velocity anisotropy of shales and depth estimation in North Sea basin, *Geophysics*, 50, 1411-1419.
- Barr, F. J., 1997, Dual-sensor OBC technology: *The Leading Edge*, 16, 45-51.

- Bergler, S., Chira, P., Mann, J., Vieth, K.-U., and Hubral, P., 2002, *Stacking velocity analysis with CRS Stack attributes*. In 64th Mtg. EAGE, Extended Abstracts, Session B003.
- Berkhout, A. J., 1980, Seismic Migration, Imaging of acoustic energy by wavefield extrapolation, Theoretical Aspects: Elsevier (2<sup>nd</sup> 1982; 3<sup>rd</sup> ed., 1985).
- Berkhout, A. J., 1992, Areal shot record technology: Journal of Seismic Exploration, Vol. 1, p. 251-264.
- Berkhout, A. J., 1997a, Pushing the limits of seismic imaging, Part I: Prestack migration in terms of double dynamic focusing: Geophysics, Vol. 62, p. 937-953.
- Berkhout, A. J., 1997b, Pushing the limits of seismic imaging, Part II: Integration of prestack migration, velocity estimation, and AVO analysis: Geophysics, Vol. 62, p. 954-969.
- Berkhout, A. J., and Rietveld, W. E., 1994, Determination of macro models for prestack migration: Part 1, estimation of macro velocities: 64<sup>th</sup> Ann. Internat. Mtg., Soc. Expl. Geophys., Expanded Abstracts, 1330-1333.
- Berkhout, A. J., and Verschuur, D. J., 1997, Estimation of multiple scattering by iterative inversion, part I: theoretical considerations: Geophysics, 62, no. 5, 1586-1595.
- Berkhout, A. J., and Verschuur, D. J., 2000, CFP-approach to multicomponent imaging: 70<sup>th</sup> Ann. Internat. Mtg., Soc. Expl. Geophys., Expanded Abstracts, 774-777.
- Berkhout, A. J., and Verschuur, D. J., 2001, Seismic imaging beyond depth migration: Geophysics, 66, 1895-1912.
- Berkhout, A. J. and Wapenaar, C. P. A., 1990, Delphi: Delft philosophy on acoustic and elastic inversion: The Leading Edge, Vol. 9, p. 30-33.
- Biloti, R., L. T. Santos and M. Tygel, 2001, Layered velocity model from kinematic attributes, Expanded Abstracts of the 7th International Congress of the Brazilian Geophysical Society, 7CISBGf/TS9, 1055-1058.



- Blott, J. E., Davis, T. L., and Benson, R. D., 1999, Morrow sandstone reservoir characterization: A 3-D multicomponent seismic success: The Leading Edge, 18, no. 3, 394-397.
- Bolte, J. F. B., 2003, Estimation of focusing operators using the Common Focal Point method: Ph.D. thesis, Delft Univ. Tech.
- Bolte, J. F. B., and Verschuur, D. J., 2001, Application of the 3D Common Focal Point matrix in pre-stack data analysis of migration aperture and acquisition design, 63<sup>rd</sup> EAGE Conference, Amsterdam, the Netherlands, extended abstracts, P164.
- Budiansky, B. and O'Connell, R. J., 1976, Elastic moduli of a cracked solid: Int. J. Solids Structure, 12, 81-97.
- Byun, B. S., Corrigan, D., and Gaiser, J., 1989, Anisotropic velocity analysis for lithology discrimination: Geophysics, 54, 1564-1574.
- Castle, R. J., 1994, A theory of normal moveout: Geophysics, 59, 983-999.
- Cholet, J., and Richard, H., 1954, A test on elastic anisotropy measurement at Berriane (North Sahara): Geophysical Prospecting, 2 (3), 232-246.
- Crampin, S., 1978, Seismic wave propagation through a cracked solid: Polarization as a possible dilatancy diagnostic: Geophys. J. R. astro. Soc., 53, 467-496.
- Crampin, S., 1981, A review of wave motion in anisotropic and cracked elastic media: Wave Motion, 3, 343-391.
- Crampin, S., 1984, Anisotropy in exploration geophysics: First Break, 2, No. 3, 19-21.
- Crampin, S., 1984, An introduction to wave propagation in anisotropic media: Geophys. J. R. Astr. Soc., 76, 17-28.
- Crampin, S., Chesnokov, E.M., and Hipkin, R.G., 1984, Seismic anisotropy – the state of The art:II., Geophys. J. of Royal Astr. Soc., 76, no. 1, 1-16.
- Daley, P. F., and Hron, F., 1977, Reflection and transmission coefficients for transversely isotropic media: Bull., Seis. Soc. Am., 67, 661-675.

- Dewangan, P., and Grechka, V., Inversion of multicomponent, multiazimuth, walkaway VSP data for the stiffness tensor, *Geophysics*, 68, 1022-1031.
- Diebold, J. B., and Stoffa, P. L., 1981, The travelttime equation, tau-p mapping, and inversion of common midpoint data, *Geophysics*, 46, 238-254.
- Dix, C. H., 1955, Seismic velocities from surface measurements: *Geophysics*, 20, 68-86.
- Engelmark, F., 2000, Using converted shear waves to image reservoirs with low impedance contrasts: *The Leading Edge*, 19, no. 6, 600-603.
- Faria, E. L., 1993, Modeling, migration and focusing analysis in transversely isotropic media: Ph.D. thesis, Univ. of Texas at Austin.
- Faria, E. L., and Stoffa, P. L., 1994, Travelttime computation in transversely isotropic media: *Geophysics*, Vol. 59, p. 272-281.
- Fei, T., Dellinger, J. A., Murphy, G. E., Hensley, J. L., and Gray, S. H., 1998, Anisotropic true-amplitude migration: 68<sup>th</sup> Annual Internat. Mtg., Soc. Expl. Geophys., Expanded Abstracts, 1677-1679.
- Ferguson, R. J. and Margrave, G. F., 2002, Depth imaging in anisotropic media by symmetric non-stationary phase shift: *Geophysical Prospecting*, 50, 281-288.
- Ferguson, R. J., and Sen, M. K., 2002,  $\tau$ -p domain estimation of elastic parameters in VTI media: 72<sup>nd</sup> Ann. Internat. Mtg., Soc. of Expl. Geophys.
- Ferguson, R. J., and Sen, M. K., 2004, Estimating the elastic parameters of anisotropic media using a joint inversion of P-wave and SV-wave travelttime error: *Geophysical Prospecting*, 52, 547-557.
- Garotta, R., Marechal, P., and Magesan, M., 1985, Two-component acquisition as a routine procedure for recording p-waves and converted waves: *J. Can. Soc. Expl. Geophys.*, 21, no. 1, 40-53.
- Garotta, R., 2000, Shear waves from acquisition to interpretation: SEG/EAGE Distinguished Instructor Series 3, Soc. Expl. Geophys., Tulsa.
- Garotta, R., Granger, P. Y., and Dariu, H., 2002, Combined interpretation of PP and PS data provides direct access to elastic rock properties, *The Leading Edge*, June 2002, 532-535.

- Geoltrain, S. and Brac, J., 1993, Can we image complex structures with first-arrival traveltimes? , *Geophysics*, 58, 564-575.
- Granli, J. R., Arntsen, B., Sollid, A., and Hilde, E., 1999, Imaging through gas-filled sediments using shear-wave data: *Geophysics*, 64, 668-677.
- Grechka, V. Y., 1998, Transverse isotropy versus lateral heterogeneity in the inversion of P-wave reflection traveltimes, *Geophysics*: 63, 204-212.
- Grechka, V., and Tsvankin I., 1998, Feasibility of nonhyperbolic moveout inversion in transversely isotropic media: *Geophysics*, 63, 957-969.
- Grechka, V., Pech, A., Tsvankin, I., and Han, B., 2001, Velocity analysis for tilted transversely isotropic media: A physical modeling example: *Geophysics*, 66, 904-910.
- Hake, H., Helbig, K. and Mesdag, C. S., 1984, Three-term Taylor series for  $t^2$ - $x^2$  curves over layered transversely isotropic ground, *Geophys. Pros.*, 32, 828-850.
- Hale, D., Hill, N. R., and Stefani, J., 1992, Imaging salt with turning waves: *Geophysics*, 57, 1453-1463.
- Harrison, M., 1992, Processing of P-Sv surface-seismic data: Anisotropy analysis, dip moveout and migration: Ph.D. thesis, University of Calgary.
- Helbig, K., 1984, Transverse isotropy in exploration seismics: *Geophys. J. Roy. Astr. Soc.*, 76, 79-88.
- Helbig, K., 1998, Layer-induced elastic anisotropy – part I: Forward relations between constituent parameters and compound medium parameters: *Revista Brasileira de Geofísica*, vol. 16(2/3), 103-112.
- Hindriks, C., and Verschuur, D. J., 2001, CFP approach to the complex near surface: 71<sup>st</sup> Ann. Internat. Mtg., Soc. Expl. Geophys., Expanded abstracts, 1863-1866.
- Hoffe, B. H., Lines, L. R., and Cary, P. W., 2000, Applications of OBC recording: *The Leading Edge*, 19, no. 4, 382-391.
- Hubral, P., 1983, Computing true amplitude reflections in a laterally inhomogeneous earth: *Geophysics*, 48, 1051-1062.

- Hubral, P., and Krey, T., 1980, Interval velocities from seismic reflection traveltimes measurements: Soc. Expl. Geophys.
- Hudson, J. A., 1981, Wave speeds and attenuation of elastic waves in materials containing cracks: Geophys. J. R. Astr. Soc., 64, 133-150.
- Issac, J. H., and Lawton, D. C., 1999, Image mispositioning due to dipping TI media: A physical seismic modeling study: Geophysics, Vol. 64, p. 1230-1238.
- Jager, R., Mann, J., Hocht, G., and Hubral, P. (2001). Common-reflection-surface stack: Image and Attributes, Geophysics, 66(1), 97-109.
- Jiao, J., Stoffa, P. L., Sen, M. K., and Seifoullaev, R. K., 2002, Residual migration-velocity analysis in the plane-wave domain, Geophysics, 67, 1258-1269.
- Jin, S., Gambois, G., and Vuillermoz, C., 2000, Shear-wave velocity and density estimation from PS-wave AVO analysis: Application to an OBS dataset from the North Sea: Geophysics, 65, 1446-1454.
- Kabir, M. M. N., 1997, Velocity estimation of the complex subsurface using the common focus point technology: Ph.D. thesis, Delft Univ. Tech.
- Kabir, M. M. N., and Verschuur, D. J., 1996, Migration velocity analysis using the common focus point technology: 66<sup>th</sup> Ann. Internat. Mtg., Soc. Expl. Geophys., Expanded Abstracts, p. 1611-1613.
- Kabir, M. M. N., and Verschuur, D. J., 2000, A constrained parametric inversion for velocity analysis based on CFP technology: Geophysics, Vol. 65, p. 1210-1222.
- Kelamis, P., Erickson, K. E., Verschuur, D. J., and Berkhout, A. J., 2002, Velocity-independent redatuming: A new approach to the near-surface problem in land seismic data processing, The Leading Edge, 21, no. 8, 730-735.
- Kennett, B. L. N., 1983, Seismic wave propagation in stratified media: Cambridge University press.
- Krey, T. H., and Helbig, K., 1956, A theorem concerning anisotropy of stratified media and its significance for reflection seismics: Geophys. Prosp., 4, 294-302.

- Kumar, D., Sen, M. K. and, Ferguson, R. J., 2004, Traveltime calculation and prestack depth migration in tilted transversely isotropic media, *Geophysics*, 69, 37-44.
- Kumar, C., Ferguson, R. J., and Sen, M. K., 2004, Migration velocity analysis in transversely isotropic media: A Common Focus Point approach: 5<sup>th</sup> Conference and Exposition on Petroleum Geophysics, Expanded Abstracts.
- Leslie, J. M. and Lawton, D.C., 1998, Anisotropic prestack depth migration: The Recorder, 3, No. 10, p. 23-26.
- Levander, A. R., 1988, Fourth-order finite-difference P-Sv seismograms: *Geophysics*, 53, 1425-1436.
- Love, A. E. H., 1944, A Treatise on the mathematical theory of elasticity: Dover Publ., Inc.
- Levin, F. K., 1979, Seismic velocities in transversely isotropic media: *Geophysics*, 44, 918-936.
- Li, X. Y., Yuan, J., Ziolkowski, A., Strijbos, F., 1999, Estimating  $V_p/V_s$  ratio from converted waves – a 4C case example: 61st Ann. Internat. Mtg., Eur. Ass. of Expl. Geophys., Expanded abstracts, P066.
- Li, X. Y., Dai, H., Mueller, M. C., and Barkved, O. I., 2001, Compensating for the effects of gas clouds on C-wave imaging: A case study from Valhall: *The Leading Edge*, 20, no. 12, 1351-1360.
- Liu, Z., and Bleistein, N., 1995, Migration velocity analysis: Theory and an iterative algorithm, *Geophysics*, 60, 142-153.
- Margrave, G. F., Lawton, D. C., and Stewart, R. R., 1998, Interpreting channel sands with 3C-3D seismic data: *The Leading Edge*, 17, no. 4, 509-513.
- Margrave, G. F., Stewart, R. R., and Larsen, J. A., 2001, Joint PP and PS Seismic Inversion, *The Leading Edge*, Sep. 2001, 1048-1052.
- Menke, W., 1989, *Geophysical Data Analysis: Discrete Inverse Theory*, Academic Press.

- Miller, S. L. M., Aydemir, E. O., and Margrave, G. F., 1995, Preliminary interpretation of P-P and P-S seismic data from Blackfoot broad-band survey: Crewes Research Report 1995, Ch 42.
- Muller, T., Jager, R. and Hocht, G., 1998, Common reflection surface stacking method – imaging with an unknown velocity model. In Expanded Abstracts, pages 1764-1767. Soc. Expl. Geophys.
- Musgrave, M. J. P., 1970, Crystal acoustics: Holden-Day, Inc. San Francisco.
- O'Connell, R. J. and Budiansky, B., 1974, Seismic velocities in dry and saturated cracked solids: J. Geophys. Res., 79, 5412-5426.
- Officer, C. B., 1974, Introduction to theoretical geophysics: Springer-Verlag.
- Ortega, J. and Rheinboldt, W. 1970, Iterative Solution of Nonlinear Equations in Several Variables (New York: Academic Press).
- Purnell, G. W., 1992, Imaging beneath a high-velocity layer using converted waves: Geophysics, 57, no. 1, 1444-1452.
- Rietveld, W. E., 1995, Controlled illumination in prestack seismic migration, Ph.D. thesis, Delft University of Technology.
- Sarkar, D., and Tsvankin, I., 2003, Analysis of image gathers in factorized VTI media, Geophysics, 68, 2016-2025.
- Schneider, W. A., 1978, Integral formulation for migration in two and three dimensions: Geophysics, 43, 49-76.
- Schneider, W. A. J., Ranzinger, K., Balch, A., and Kruse, C., 1992, A dynamic programming approach to first-arrival traveltimes computation in media with arbitrarily distributed velocities, Geophysics, 57, 39-50.
- Schneider, W. A., 2002, A simple, exact solution for the P-Sv wave conversion point via prestack migration: Geophysics, 67, 1634-1636.
- Schoenberg, M., and J. Douma, 1988, Elastic wave propagation in media with parallel fractures and aligned cracks: Geophysical Prospecting, 36, 571-590.
- Sen, M. K., and Stoffa, P. L., 1995, Global optimization method in geophysical inversion: Elsevier Sci. Publ. Co., The Netherlands.

- Sen, M. K., 2006, Seismic Inversion, SPE, Richardson, USA.
- Sen, M. K. & Mukherjee, A., 2003,  $\tau$ -p analysis in transversely isotropic media: Geophys. J. Int., 154, 647-658.
- Stewart, R. R., Gaiser, J. E., Brown, R. J., and Lawton, D. C., 2002, Converted-wave seismic exploration: Methods: Geophysics, 67, no. 5, 1348-1363.
- Stewart, R. R., Gaiser, J. E., Brown, R. J., and Lawton, D. C., 2003, Converted-wave seismic exploration: Applications: Geophysics, 68, no. 5, 40-57.
- Stoffa, P. L., Buhl, P., Diebold, J. B., and Wenzel, F., 1981, Direct mapping of seismic data to the domain of intercept time and ray parameter – A plane-wave decomposition, Geophysics, 46, 255-267.
- Stoffa, P. L., Sen, M. K., Seifoullaev, R., Pestana, R., and Tanis, M., 2003, Seismic Imaging and Velocity Analysis: Current Status and Future Directions, SIAM presentation.
- Stolt, R. H., and Benson, A. K., 1986, Seismic Migration Theory and Practice: Handbook of Geophysical Exploration Vol. 5, Geophysical Press.
- Stunff, Y. L., Grechka, V., and Tsvankin, I., 2001, Depth-domain velocity analysis in VTI media using surface P-wave data: Is it feasible?, Geophysics, 66, 897-903.
- Taner, M. T., and Koehler, F., 1969, Velocity spectra - digital computer derivation and applications of velocity functions: Geophysics, 34, no. 6, 859-881.
- Tarantola, A., 2005, Inverse Problem Theory and Methods for Model Parameter Estimation, SIAM, Philadelphia.
- Tatham, R. H., and Goolsbee, D. V., 1984, Separation of P- and S-wave reflections offshore western Florida, Geophysics, 49, 493-508.
- Tatham, R., and McCormack, M. D., 1991, Multicomponent seismology in petroleum exploration, SEG, Tulsa, Oklahoma.
- Tessmer, G., Krajewski, P., Fertig, J., and Behle, A., 1990, Processing of PS-reflection data applying a common conversion point stacking technique: Geophys. Prosp., 38, 267-286.

- Thomsen, L. 1986, Weak elastic anisotropy, *Geophysics*, 51, 1954-1966.
- Thorbecke, J. W., 1997, Common focus point technology: Ph.D. thesis, Delft Univ. Tech.
- Tsvankin, I., 1996, P-wave signatures and notation for transversely isotropic media: An overview: *Geophysics*, 61, 467-483.
- Tsvankin, I., 1997, Anisotropic parameters and P-wave velocity for orthorhombic media: *Geophysics*, 62, 1292-1309.
- Tsvankin, I., and Thomsen, L., 1994, Nonhyperbolic reflection moveout in anisotropic media, *Geophysics*, 59, 1290-1304.
- Tsvankin, I., and Thomsen, L., 1995, Inversion of reflection traveltimes for transverse isotropy, *Geophysics*, 60, 1096-1108.
- Tsvankin, I., 2001, Seismic signatures and analysis of reflection data in anisotropic media: Pergamon Press, Inc.
- Uhrig, L. F., and van Melle, F. A., 1955, Velocity anisotropy in stratified media, *Geophysics*, 20, 774-779.
- Van der Baan, M., 2005, Some comments on common-asymptotic-conversion-point (CACP) sorting of converted-wave data in isotropic, laterally inhomogeneous media: *Geophysics*, 70, U29-U36.
- Varela, C. L., 1996, Automatic background velocity estimation in 2D laterally varying media: Ph.D. thesis, University of Texas at Austin.
- Varela, C. L., Stoffa, P. L., and Sen, M. K., 1998, Background velocity estimation using non-linear optimization for reflection tomography and migration misfit: *Geophys. Prosp.*, 46, 51-78.
- Vestrum, R. W., Lawton, D. C., and Schmid, R., 1999, Imaging structures below dipping TI media: *Geophysics*, 64, 1239-1246.
- Virieux, J., 1986, P-Sv wave propagation in heterogeneous media: Velocity-stress finite-difference method: *Geophysics*, 51, 889-901.
- Wapenaar, C. P. A., and Berkhout, A. J., 1989, Elastic wave field extrapolation: redatuming of single- and multi- component seismic data: Elsevier Science Publ. Co., Inc.



- White, J. E., and Sengbush, R. L., 1953, Velocity measurements in near-surface formations, *Geophysics*, 18, 54-69.
- Winterstein, D. F., 1989, Velocity anisotropy terminology for geophysicists: *Geophysics*, 55, 1070-1088.
- Yan, L., and Lines, L. R. (2001), Seismic imaging and velocity analysis for an Alberta Foothills seismic survey. *Geophysics*, 66, 721-732.
- Yilmaz, O., and Chambers, R., 1984, Migration velocity analysis by wavefield extrapolation, *Geophysics*, 49, 1664-1674.
- Yilmaz, O., 1987, *Seismic Data processing*, SEG, Tulsa, Oklahoma.
- Yuan, J., 2001, Analysis of four-component seafloor seismic data for seismic anisotropy: PhD thesis, The University of Edinburgh.
- Zhang, Y., Bergler, S., and Hubral, P. (2001). Common-Reflection-Surface (CRS) stack for common-offset. *Geophys. Prosp.*, 49(6), : 709-718.

## **Vita**

Chandan Kumar was born in Barhiya, Bihar, India, on November 5, 1978, to Sr. Nandkishore Prasad Singh and Smt. Subhadra Devi. He completed his high school from R. K. Mission Vidyapeeth, Deoghar in 1994, and secondary level education from D. P. School, Bokaro Steel City, India in 1996. He entered the Department of Geology and Geophysics at the Indian Institute of Technology, Kharagpur, India in 1997. He graduated with the Master of Science degree in Exploration Geophysics in 2002. During June 2001 to August 2001, he did internship with National Geophysical Research Institute, Hyderabad. In August 2002, he enrolled in the PhD program in the Department of Geological Sciences at the University of Texas at Austin. During the summer of 2005 he worked for BP America Inc, with Arkoma Asset team as a Geophysicist. Upon graduation he will join BP America Inc, Gulf of Mexico Deep Gas (Texas Asset), Houston, Texas. He is a member of SEG, EAGE and SPG.

Permanent address: C/85, A. G. Colony, Po. Aashiana, Patna-25, India.

This dissertation was typed by the author.